Spring 1977

COSMIC RAY ISOTOPIC COMPOSITION: NEON THROUGH IRON

GEORGE ARTHUR SIMPSON
University of New Hampshire, Durham

INFORMATION TO USERS

This material was produced from a microfilm copy of the original document. While the most advanced technological means to photograph and reproduce this document have been used, the quality is heavily dependent upon the quality of the original submitted.

The following explanation of techniques is provided to help you understand markings or patterns which may appear on this reproduction.

1. The sign or "target" for pages apparently lacking from the document photographed is "Missing Page(s)". If it was possible to obtain the missing page(s) or section, they are spliced into the film along with adjacent pages. This may have necessitated cutting thru an image and duplicating adjacent pages to insure you complete continuity.

2. When an image on the film is obliterated with a large round black mark, it is an indication that the photographer suspected that the copy may have moved during exposure and thus cause a blurred image. You will find a good image of the page in the adjacent frame.

3. When a map, drawing or chart, etc., was part of the material being photographed the photographer followed a definite method in "sectioning" the material. It is customary to begin photoing at the upper left hand corner of a large sheet and to continue photoing from left to right in equal sections with a small overlap. If necessary, sectioning is continued again — beginning below the first row and continuing on until complete.

4. The majority of users indicate that the textual content is of greatest value, however, a somewhat higher quality reproduction could be made from "photographs" if essential to the understanding of the dissertation. Silver prints of "photographs" may be ordered at additional charge by writing the Order Department, giving the catalog number, title, author and specific pages you wish reproduced.

5. PLEASE NOTE: Some pages may have indistinct print. Filmed as received.

University Microfilms International
300 North Zeeb Road
Ann Arbor, Michigan 48106 USA
St. John's Road, Tyler's Green
High Wycombe, Bucks, England HP10 8HR

COSMIC RAY ISOTOPIC COMPOSITION: NEON THROUGH IRON

by

GEORGE SIMPSON
B.Sc., University of Calgary, 1967
M.Sc., University of Calgary, 1970

A THESIS

Submitted to the University of New Hampshire
In Partial Fulfillment of
The Requirements for the Degree of

Doctor of Philosophy
Graduate School
Department of Physics
May, 1977

This thesis has been examined and approved.

W R Webber

Thesis director, W. R. Webber
Prof. of Physics

R. L. Arnoldy

R. L. Arnoldy, Prof. of Physics

E. L. Chupp

E. L. Chupp, Prof. of Physics

R. E. Houston

R. E. Houston, Prof. of Physics

J. A. Lockwood

J. A. Lockwood, Prof. of Physics

Feb 25/77

Date

ACKNOWLEDGMENTS

I'd like to express my sincerest thanks to those who have helped make this thesis study a success:

W. R. Webber, who guided the work from a variety of distances, but always with insight and energy, will always be remembered as a model scientist and advisor;

Jim Kish, whose practical genius in getting instruments built and working has been warmly studied;

my family, especially Margie, who shared in the making of a creative and happy home at UNH;

and the Space Science Center Staff, whose friendly energy and straightforward ways were a pleasure to deal with: Renee Sperl, Janet Varney, Grace Richards, Al Knight, and Arthur Anderson.

I also owe a debt of thanks to several friends working in associated areas who shared their thoughts with me on many occasions: Jerry Lezniak, Allan Preszler, and John Barbary.

I acknowledge financial support obtained through NASA grant NGR 30-002-052.

TABLE OF CONTENTS

LIST OF ILLUSTRATIONS

CHAPTER I

CHAPTER II

CHAPTER III

CHAPTER IV

CHAPTER V

APPENDIX 2

LIST OF TABLES

ABSTRACT

ISOTOPIC COMPOSITION OF COSMIC RAYS:
NEON THROUGH IRON

by

GEORGE SIMPSON

This thesis describes an experimental determination of the isotopic composition of cosmic rays, and discusses the implications of the measurement for theories of cosmic ray origin. The work is seminal in that it gives the first high resolution results in the region Neon through Iron. After a brief introduction to the significance of the experiment and previous work in Chapter I, Chapters II and III recount the design of the balloon-borne instrument with which the measurements were performed. The analysis of the data, including interaction rejection with consistency criteria, calibration of the instrument using the flight data, and charge and mass assignments for each event, is discussed in the fourth chapter. A systematic method of treating the non-linear response of plastic scintillators is a feature of the data analysis. Chapter V presents isotopic mass histograms and traces the nuclear interaction corrections through the instrument and the atmosphere. The instrumental performance is evaluated at the close of this chapter. In

Chapter VI, a conventional propagation model is used to translate the observations through the interplanetary medium and the galaxy to the sources. Chapter VII concludes the thesis with a discussion of the significance of the results in the context of published nucleosynthesis theory.

An Appendix gives full details of the unique pathlength correction system developed for the experiment.

This thesis provides an affirmative answer to the question "do the isotopic abundances of cosmic rays at the source differ significantly from the solar system abundances?".

GLOSSARY

gm.cm-2	grams per square centimeter; a unit of material thickness
dE/dx	kinetic energy loss per gm.cm-2
A**B	notation for A to the power B
X.EY	notation for X times 10 to the power Y
pm	photomultiplier, converts light to electric current
E	kinetic energy; also denotes kinetic energy measuring detector, or the output of such a detector
S	dE/dx measurement or detector
C	Cerenkov measurement or detector
k, K	normalization constants
n	refractive index
v	velocity in units of the speed of light
PEN	p.netration detector, the bottom element of the experiment
Q,q	standard deviation, sigma
Qpe	sigma due to photoelectron statistics
M	mass of nucleus
Z	particle charge
A	particle atomic weight

CHAPTER I

INTRODUCTION

This thesis describes an experimental determination of the isotopic composition of cosmic rays. The work is seminal in that it gives the first high mass resolution results in the region Neon through Iron. In this introductory chapter, we set the stage for the results to follow with a brief survey of current notions of cosmic ray origin, and a review of previous experimental achievements in this area.

1.0 THEORIES OF COSMIC RAY ORIGIN

It was in 1934, only four years after the discovery of the neutron, that the theory of cosmic ray origin which is now thought most likely was proposed by Baade and Zwicky (Baade and Zwicky, 1934). Since the 1950's, the debate on cosmic ray origin has centered on two main issues:

1. local versus extragalactic origin;
2. supernova (or other stellar event) versus statistical interstellar origin (Fermi mechanism).

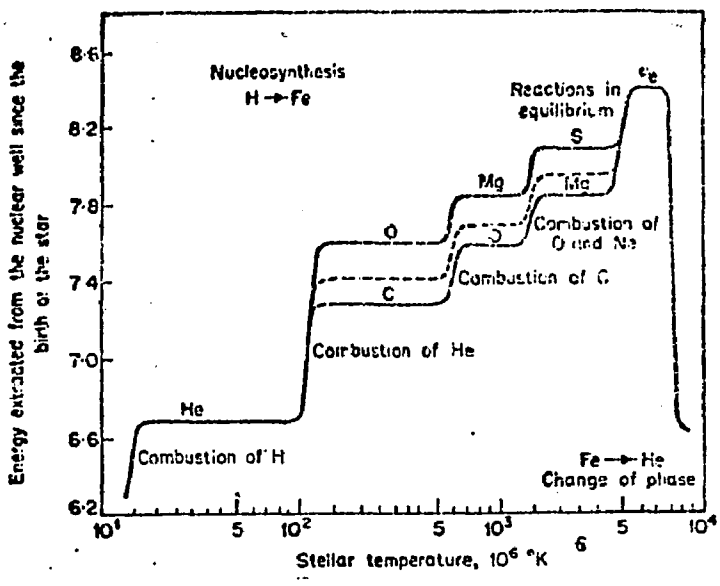

Figure 1.1

The Stages of Nucleosynthesis

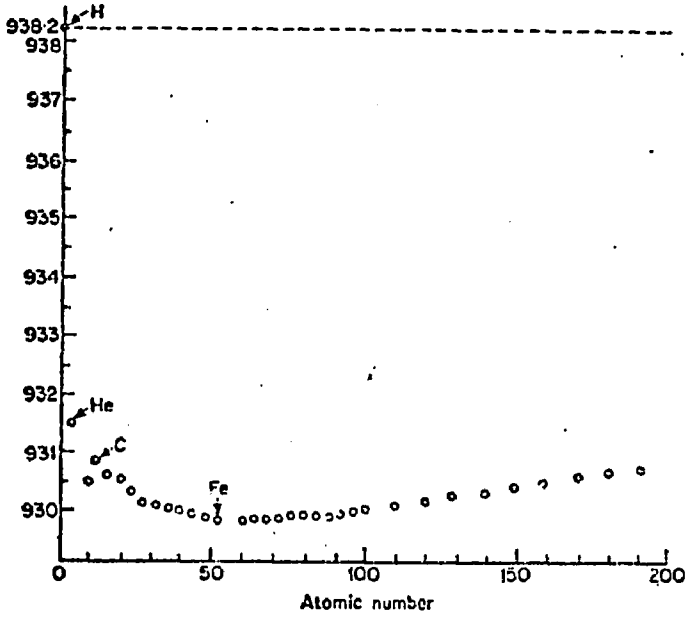

Figure 1.2

Mass/Nucleon of the Stable Nuclei

The results presented in this thesis bear on the second issue; regarding the first, we note only that at the energies we are discussing (ca 6.E8 eV), recent gamma-ray observations (Fichtel et al., 1975) have put the the weight of evidence with the galactic hypothesis (Stecker, 1975; Burbidge, 1974).

The inferences that can be made about cosmic ray origin from our isotopic composition measurements will draw heavily upon the theory of the evolution of matter in stars. This theory, first introduced in detail by Burbidge et al. (1957), shows the way in which a universe of primordial Hydrogen evolves to the observed state of 92 different elements, through the burning of matter deep in the interior of stars. The burning takes place in stages of ever increasing temperature and decreasing interval of time: Hydrogen burning, in which Helium or Carbon, Nitrogen and Oxygen are formed, spans some 1.E9 years, while the final step of evolution, in which massive stars build up the majority of the periodic table, is an explosive event, which may last only some hours or seconds. Figure 1.1 (from Reeves, 1968) shows the stages of nucleosynthesis, as they are presently conceived. It is with the last step, which is the explosion of supernovae, that many theorists have associated cosmic ray origin (Ginzburg, 1957). The arguments in favor of this association are the matching of the enormous energy content of the cosmic rays in the galaxy (3.E49 to 1.E50 ergs) to the energy output of supernovae,

and the observations of gamma rays (Hartman et al., 1976) from the vicinity of known supernova remnants in the galaxy. The gamma ray observations are taken to be evidence of energetic particles producing pi-0 mesons, which decay to gamma rays.

Opposing this point of view historically were (1) theories of statistical interstellar origin (Fermi mechanism Fermi, 1949, 1954), which propose that moving magnetic fields in the interstellar medium may accelerate the cosmic rays because of the statistically higher probability of a head-on collision (energy gain), than an overtaking collision (energy loss); and (2) the point of view that the observed acceleration of particles by the sun is evidence that ordinary stars may provide the bulk of the cosmic rays (Richtmeyer and Teller , 1949).

Recently, the Fermi mechanism was mated with supernova origin in the acceleration theory of Scott and Chevalier (1975). Magnetic "knots" in the expanding supernova shock wave accelerate particles by the second-order Fermi mechanism. Another modern variant of the supernova origin theory is the neutron-star (pulsar) accelerator mechanism of Sturrock (1971). In this theory the rotational kinetic energy of the neutron star is transferred to charged particles by the neutron star's intense magnetic field.

We should keep in mind the following points regarding cosmic ray origin theories:

1. Nucleosynthesis theory has proceeded by attempting to match the composition predicted by stellar model calculations to the observed solar system abundances. "Solar system" (Cameron, 1974) abundances were fixed at this location some 1.E9 years ago. That these abundances are typical of the present epoch in other reaches of the galaxy is an untested assumption. This is an important premise underlying the comparison of cosmic ray composition with solar system abundances.

2. The exact mechanism of supernova explosions is still highly uncertain, although there exist some models (Colgate, 1965,1973; Arnett, 1966). None of the mechanisms proposed for the supernova detonation are currently free from serious objection. A recent review article comments: "The nuclear groundwork is being laid for the calculation of the cosmic rays produced in supernovae and other explosive events." (Fowler, 1975).

3. Supernova origin faces a severe problem in that energetic particles within the cavity of the source may suffer adiabatic deceleration due to the expanding magnetic field (Kulsrud and Zwiebel, 1975; but see also Cowsik and Wilson, 1975.).

4. Fermi acceleration requires an injection mechanism for the particles, in order that the rate of energy gain exceed the ionization loss. The ionization loss goes as Z**2, which strongly constrains the available injection mechanisms.

5. It has been proposed that variations of cosmic ray composition from the solar system abundances may be explained entirely in terms of selective acceleration mechanisms (Casse and Goret, 1973; Casse, Goret and Cesarsky, 1975). This hypothesis (in its strongest form) removes the cosmic rays from any connection with the site of the nucleosynthesis, the source material for the cosmic rays being simply the ambient interstellar medium and/or the outer envelope of the accelerating body.

Setting aside the limitations of the theories, we may see from Figure 1.2 the reason for the central importance of Iron in the nucleosynthesis chain. Iron, being the most stable of all elements, is the final product of nuclear fusion reactions. Any further composition changes result in energy loss to the star. The isotopic Iron abundances reflect in the most direct manner the temperatures and densities at the site of the nucleosynthesis. If the cosmic rays have their origin in an extreme environment such as the supernova, they may reflect this fact by an alteration in

Goddard Space Flight Center
Isotope Experiment

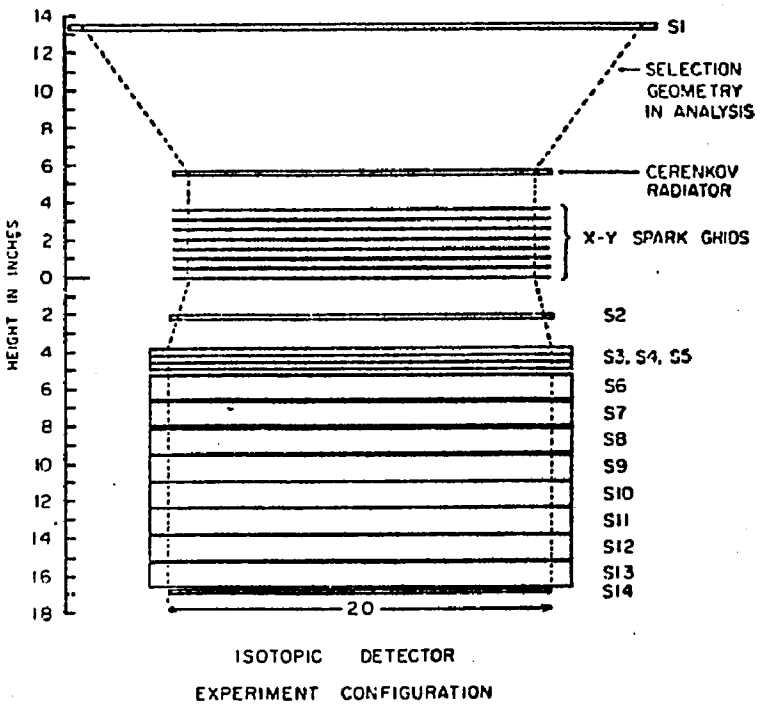

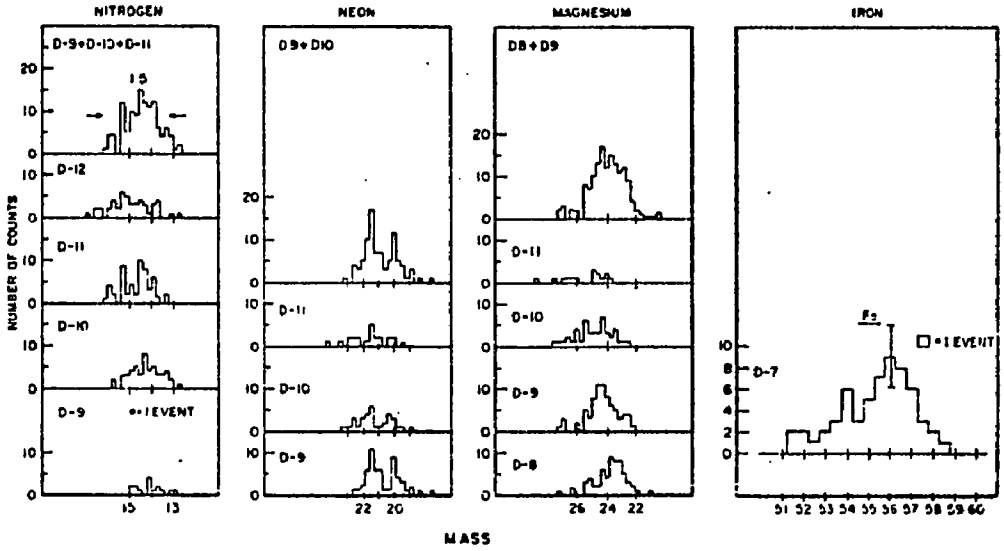

Figure 1.3
Experiment and Results of Fisher et al. (1975)

their isotopic composition. However, if they are produced in an environment in which nuclear build-up is not occurring, it is expected that the composition would not differ significantly from the solar system abundances predicted by standard nucleosynthesis theory.

2.0 PREVIOUS EXPERIMENTAL ACHIEVEMENTS

The study of the isotopic composition of the cosmic rays has a history which follows the evolution of the instrumentation from small experiments capable of resolving the isotopes of Hydrogen and Helium (Fan et al., 1966), to present-day balloon experiments weighing nearly a ton, which have the ability to resolve species for a wide range of elements and energies.

At the present time, a variety of approaches are being pursued. Below, we discuss briefly the method and results of the leading groups, restricting ourselves to those reporting isotopic information for Z>9.

Fisher et al (1975, Goddard Space Flight Center) have presented results on isotopic composition from the Cerenkov-Range analysis of data obtained with the instrument shown in Figure 1.3. It may be noted that in this experiment, spark grids are used to define the particle trajectory through the flat detectors, and that the scintillators S3-S14 are used to bring the particle to rest.

University of Kiel
Plastic Track Detector Experiment

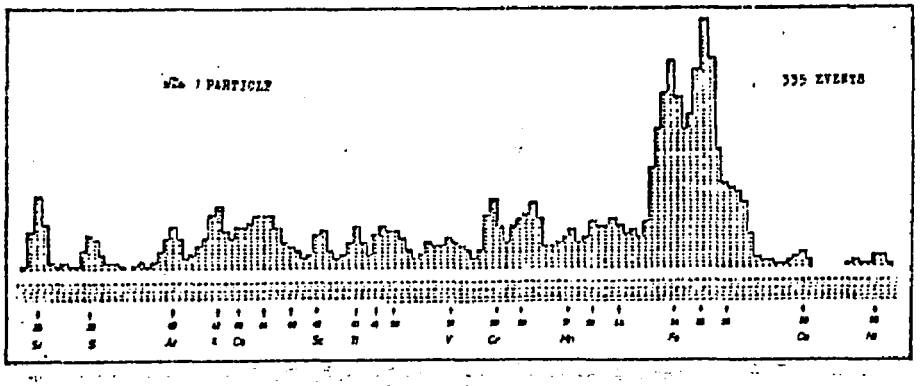

Spectrum of Si (Z=14) up to Ni (Z=28) for E=150-500 MeV/nuc.

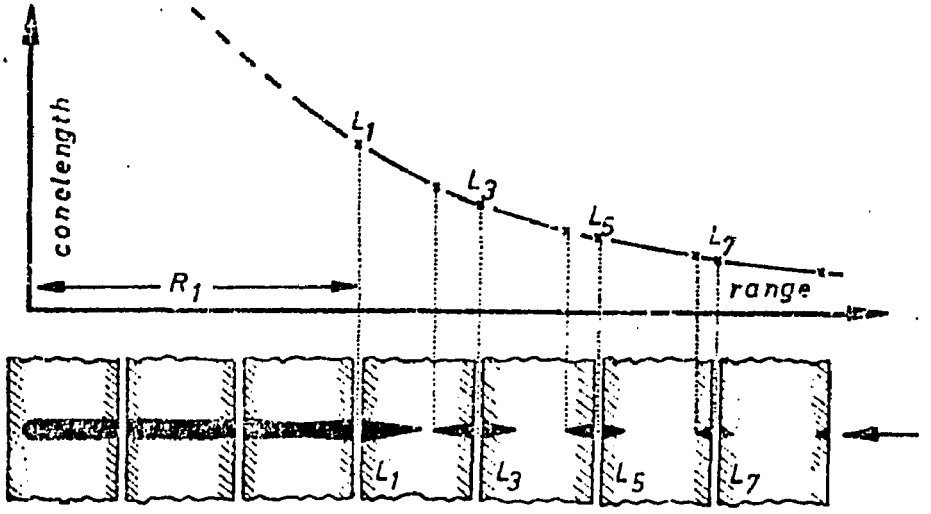

Cone length image of a stopping ionizing particle in plastic track detector sheets (not in scale)

Figure 1.4

Results and Experiment of Siegman, Bartholomä and Enge (1976)

In this way, multiple dE/dx measurements are made, and the range measurement is absolute to within the thickness of a detector. Charge is determined from dE/dx versus range, while the Cerenkov-range pair give mass information. These results may also be seen in Figure 1.3.

Bartholema et al (1975, University of Kiel) analyzed particles stopping in a stack of eighteen 250-micron thick sheets of Lexan polycarbonate. Heavy nuclei stopping in the plastics leave a cylindrical region of radiation damage which is later etched. The dimension of the resultant cavities in the plastic along the particle track reflect the rate of ionization energy loss (dE/dx). This combination of dE/dx measurement with precisely determined range allows mass analysis. Figure 1.4 shows these results, and gives an illustration of the technique.

Dwyer and Meyer (1976; University of Chicago) obtained results on Ne, Mg, and Si with their scintillator-Cerenkov experiment. Flying their package at a geomagnetic latitude such that cosmic rays of energies just above the Cerenkov threshold were cut off by the geomagnetic field, they analyzed the distribution of Cerenkov pulse heights to obtain the mean mass of each element. They quote values of 20.45, 24.32, and 28.26, respectively. These values are corrected for atmospheric interactions, and refer to energies around 1.2 GeV/nucleon. The quoted errors are 0.1 to .16 AMU.

New Hampshire 1973 Isotope Experiment

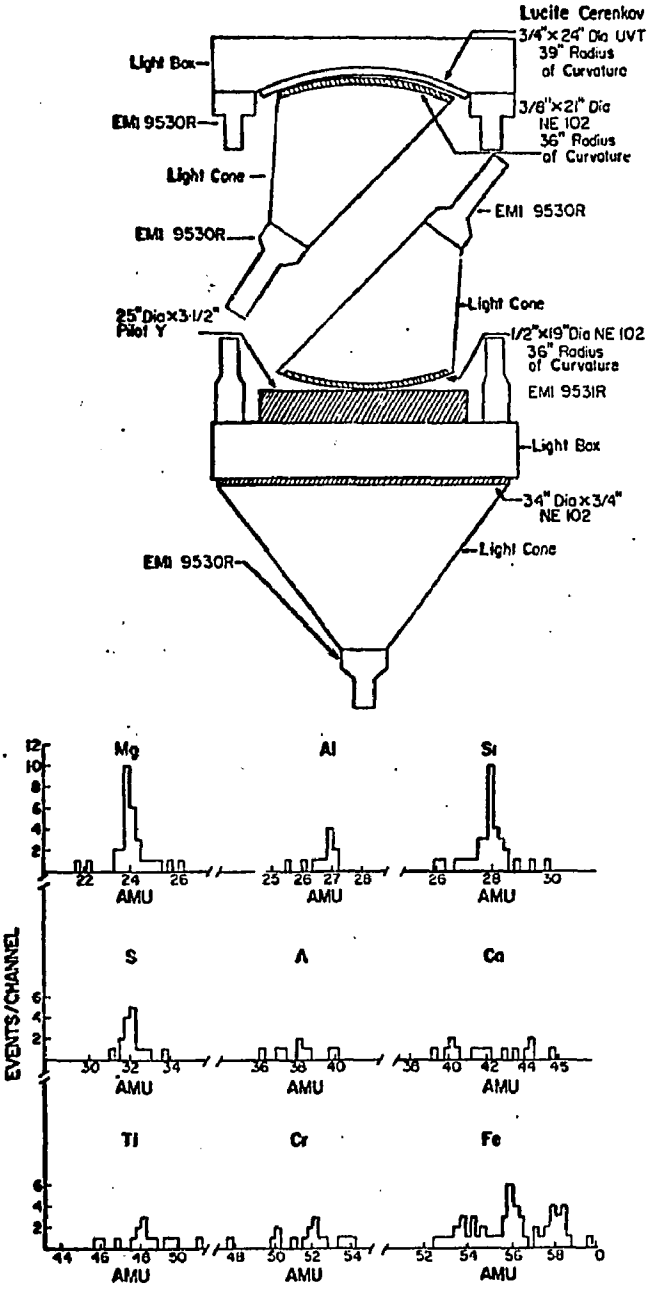

Figure 1.5

Experiment and Results of Webber, Lezniak and Kish (1973)

Benegas et al (1975, St Louis) used a similar approach to estimate the mean mass of iron. They give a value of 54.2+/-1.3 AMU.

The 1973 results of Webber et al (University of New Hampshire) continue to be competetive with the later results mentioned above. The experiment was an earlier generation of that described in this thesis. We display these results and that instrument in Fig 1.5.

Facing 8

CHAPTER II

EXPERIMENT: DESCRIPTION AND DETECTOR TECHNIQUE

The measurement of the isotopic composition of the cosmic rays is an exciting challenge to the experimental physicist, both because of the likely significance of the results to the question of cosmic ray origin, and the difficulty of the measurement. The task is intrinsically difficult because

1. the flux of primary particles is low: less that one Iron particle per square meter-steradian-Mev-hour;

2. the physical difference among the isotopes of each element is small: the mass difference is only 2%/AMU for the Iron isotopes; and

3. the cosmic ray nuclei are fragile at these energies, fragmenting into lower atomic weight nuclides when they collide with other nuclei.

Making further demands upon the experimentalist's technique is the extreme environment of the upper atmosphere in which the instrument must function reliably.

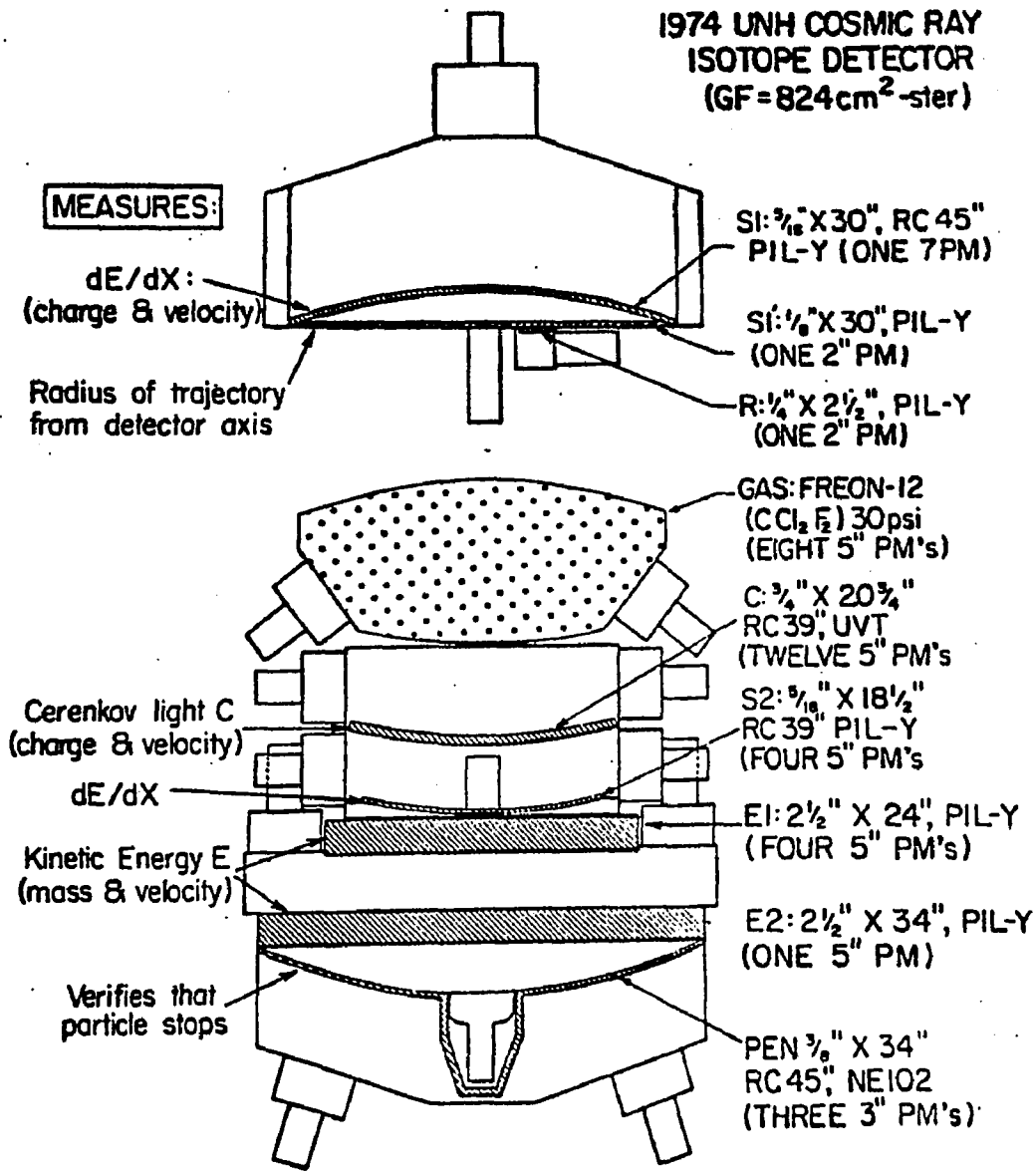

Figure 2.1. 1974 UNH Cosmic Ray Isotope Experiment

To facilitate the discussion of our solutions to these challenges, we have divided the topic between chapters II and III. This chapter gives a survey of the instrument, introduces the factors which contribute to the resolution of each detector type, and gives some details of our experimental technique. Chapter III gives a discussion of the design of the complete system.

1.0 SURVEY OF THE EXPERIMENT

Figures 2.1 and 2.2 show a line drawing and a photograph of the instrument. It is designed to study the isotopic composition, energy spectrum, and chemical abundances of cosmic ray species from Z=2 (Helium) through Z=28 (Nickel) in energy intervals starting at 200 Mev/nucleon, and extending as high as 50 Gev/n. The mode of interest in this discussion is that in which the particles are brought to rest in the thick counters E1 and E2 (stopping mode). In this mode maximum information on isotopic composition is obtained.

The main design objectives pertinent to the isotopic composition mode were:

1. Resolution substantially less than one AMU for Z=2 to 28

2. Geometrical factor as large as possible

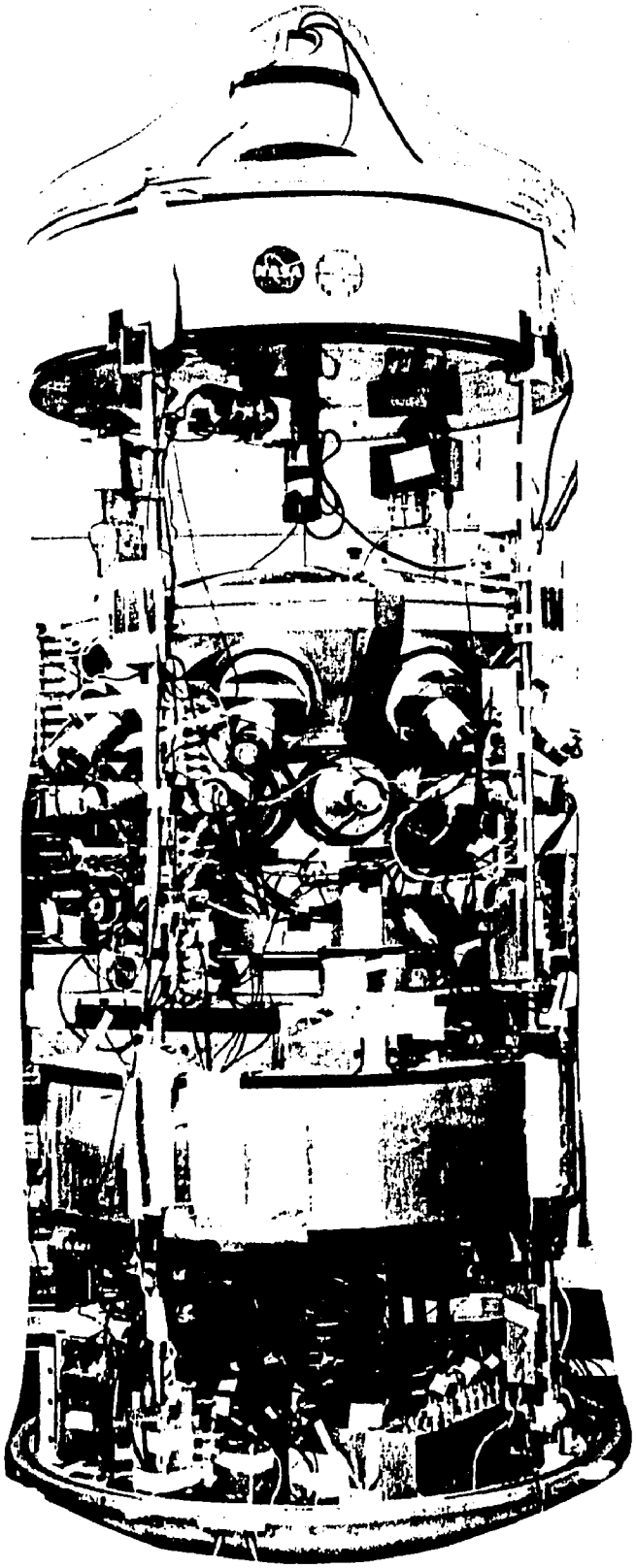

1974
Isotope
Experiment

Figure 2.2

3. Nuclear interaction rejection capability

4. Simplicity and reliability

The main features of the telescope as seen in Figure 2.1 are:

1. S1 and S2, the two thin scintillators, which measure the rate of ionization energy loss, dE/dx, and define the telescope geometry*;

2. the thick scintillators E1 and E2, in which the particles of interest are brought to rest, thus measuring the residual kinetic energy E;

3. the Cerenkov detector C, which measures particle velocity. Isotopic separation is achieved with this counter because at fixed charge and velocity, heavier isotopes penetrate deeper into the E counters. The material between the C and E counters and the rapid change of Cerenkov output with velocity combine to magnify this separation.

Also seen in Figure 2.1 are the gas Cerenkov detector (which is not of interest for low-energy isotope resolution, since its threshold energy is well above the energy of

*We will refer to the combination (S1+S2)/2 as simply S in the text.

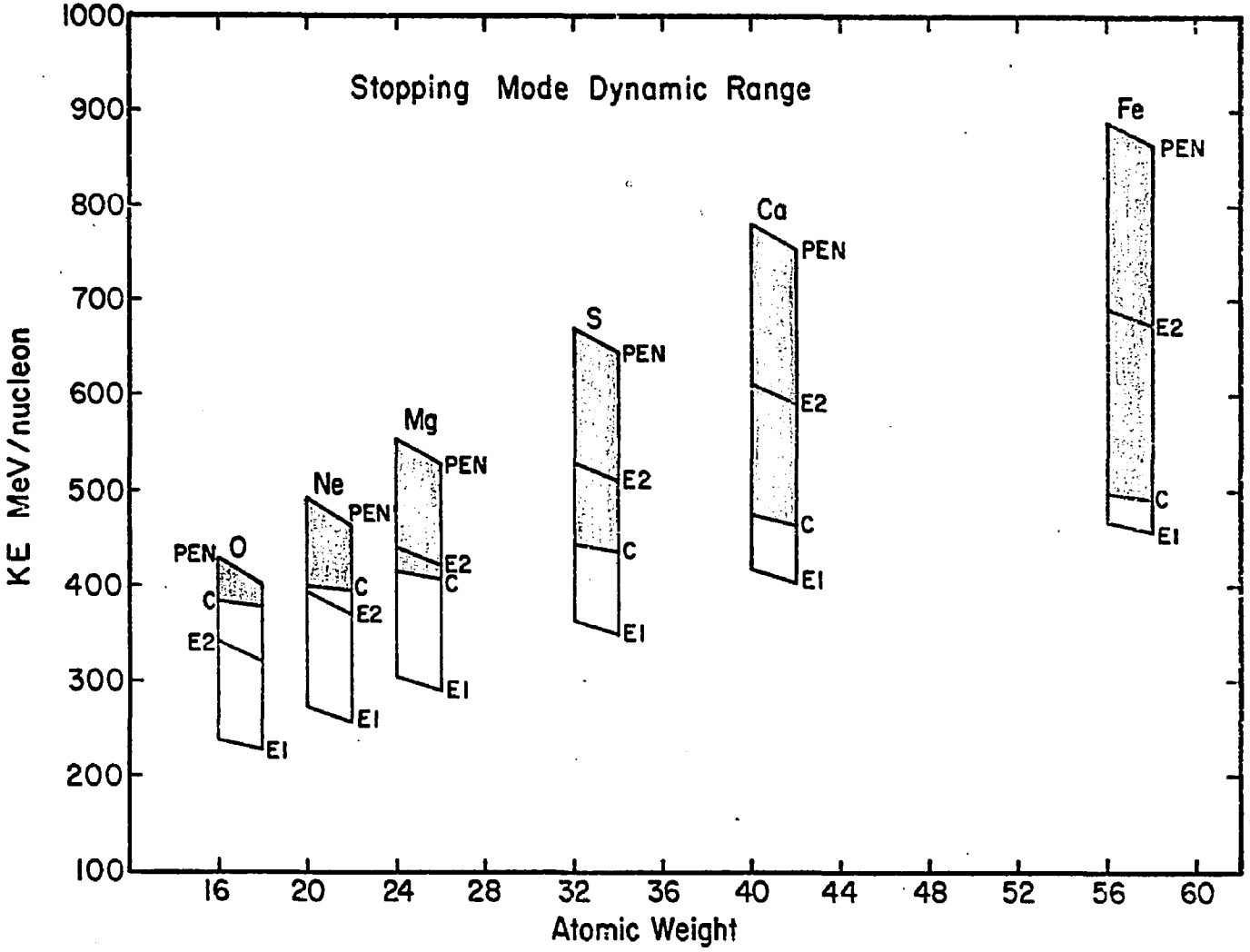

Figure 2.3 Stopping Mode Dynamic Range

particles which can stop in the E counters), and the S1' counter, which is provided to measure the radius of the particle trajectory from the detector axis. This information is used to correct for pathlength differences and thereby to improve the resolution of the C, S2, E1, and E2 detectors. The N detector helps establish the scale of the radius measurement in S1'. The penetration detector (PEN) discriminates between particles which pass through E2 and those which stop in it.

The energy range of the stopping mode is illustrated in Figure 2.3, which shows the incident kinetic energy per nucleon required of particles to activate each detector as a function of atomic number. The band of energies in which the particle stops (below PEN threshold) and the Cerenkov threshold is exceeded is the region of interest for this study. An alternate mode of istopic analysis, applicable to all low-Z particles stopping in E1 or E2 is available, which uses the S counter instead of the Cerenkov counter. The two modes of analysis are complementary, since the Cerenkov threshold does not occur for particles which stop in the E counters until Z=8, while the resolving power of the S versus E1 or E2 analysis is best for Z<8.

The detection process using scintillators and Cerenkov radiators starts when particles passing through the detector material have part of their energy loss converted to light. In plastic scintillators, the light production occurs in

four steps. The particle ionizes atoms in its path, producing a thick jet of knock-on electrons; the electrons excite atoms along their path; the excited atoms decay, emitting in the ultraviolet; and finally the ultraviolet light is absorbed and reradiated in the visible spectrum by wavelength shifters in the plastic. As a crude approximation, the light output (L) of plastic scintillators is proportional to the particle's energy loss: $L=A(dE/dx)$.

Cerenkov radiation is an electromagnetic effect by which particles travelling faster than the speed of light in a medium are decelerated (Jelley, 1954). While scintillation light exhibits significant departures from $L=A(dE/dx)$, Cerenkov light "C" is governed exactly by the relation

$$C = K'Z^2(1-\frac{1}{(nv)^2})$$

n being the refractive index of the medium, and v being the velocity in units of the velocity of light. On the other hand, the yield of light from Cerenkov detectors is much less than that from scintillators. (Note the twelve photomultipliers used to view the C detector.)

The detection process is completed when light from the Cerenkov or scintillator plastic finds its way to a photomultiplier, and is converted to an electrical pulse for digitization. The light diffusion boxes which surround the S, C ,E and PEN elements are seen in Figure 2.1. The box walls are painted with $BaSO_4$ paint, which has a reflectivity

of 97%, to minimize loss of useful photons during their transport from the plastic to the photomultiplier.

2.0 RESOLUTION OF INDIVIDUAL DETECTORS

Stated in its simplest form, our experiment design problem is to find a configuration of detectors such that the separation of adjacent isotopes is greater than the resolution of the system. Thus the design study focusses first on the resolution (Q) of each detector. We give next a discussion of the physical effects which contribute to the resolution of the individual Cerenkov, dE/dx, and E counters.

2.1 PHOTOELECTRON STATISTICS

All detectors which collect photons with photomultipliers are subject to resolution broadening due to photoelectron statistics (Qpe). The conversion efficiency of photons to electrons at the photomultipler cathode is typically 20%. Poisson statistics governs fluctuations in the number of electrons emitted (J) for a given light pulse. Neglecting the contribution to the broadening from succeeding stages of the tube, we have*:

$$Q_{pe} = \sqrt{J} / (J-1)$$

*All resolutions (Q,q) are expressed as one sigma fractions, unless otherwise noted.

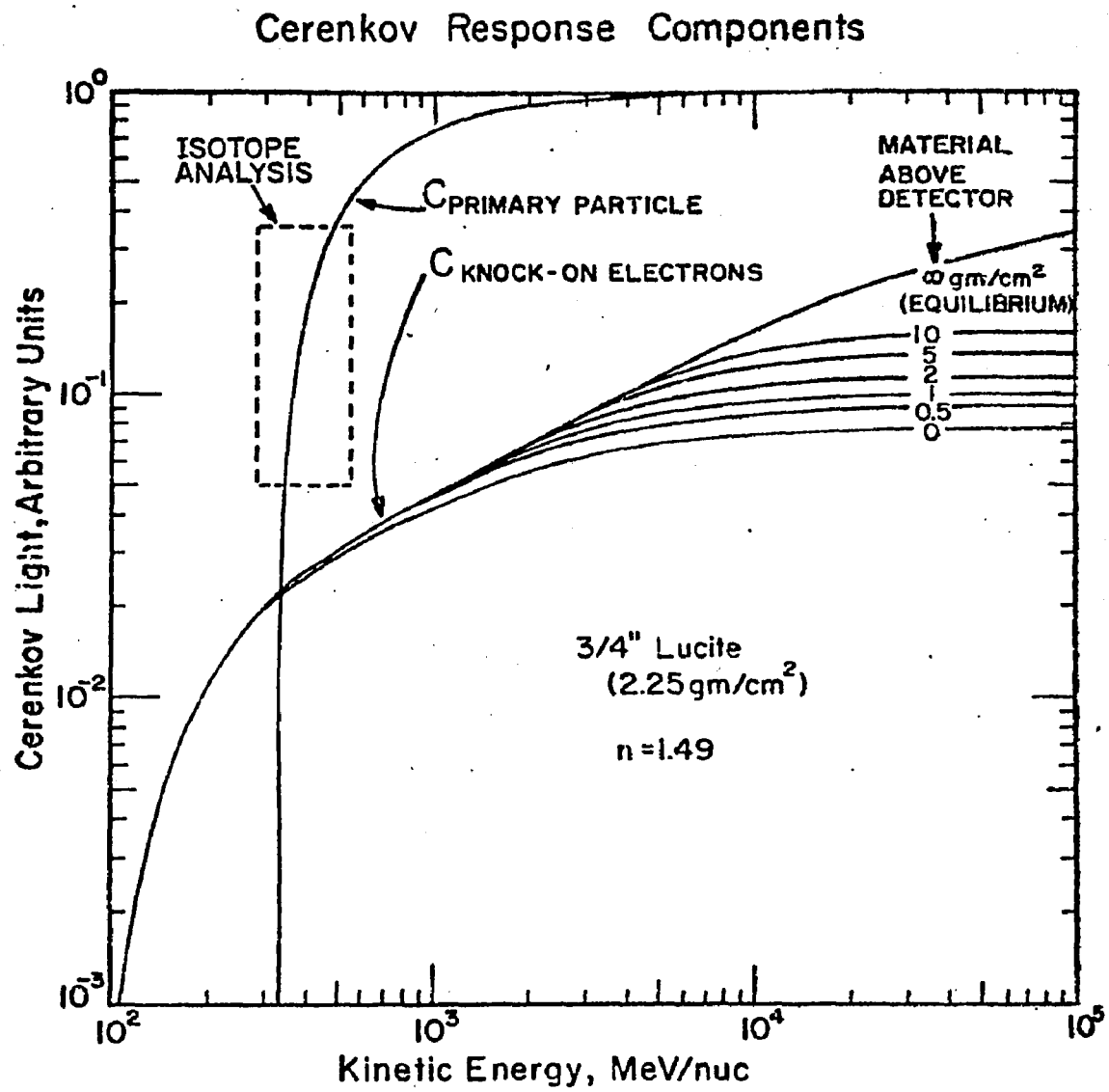

Figure 2.4

Cerenkov Response Components

For Cerenkov detectors, photoelectron statistics dominates the resolution over much of the operating range. Note that since Cerenkov output C varies as Z**2,

$$Q_C = \frac{q}{Z} \left(\frac{C_{max}}{C}\right)^{\frac{1}{2}}$$

where:

q=resolution for v=1, Z=1 particles, and
Cmax is the Cerenkov output for v=1 particles of charge Z.

2.2 FAST KNOCK-ON ELECTRONS IN CERENKOV COUNTERS

A small fraction of the knock-on electrons have velocities exceeding the Cerenkov threshold, thus emitting additional Cerenkov light. Lezniak(1976) has analyzed this contribution in detail, including the contribution from material above the detector itself. Figure 2.4 shows the contribution to the Cerenkov output due to knock-on electrons. Over the range of interest (shown) this source of resolution broadening is small.

2.3 THIN SCINTILLATOR STATISTICS

Fluctuations in the energy transfer from the primary particle to secondary electrons dominate the resolution of thin scintillators. Although the distribution of scintillator outputs due to these fluctuations may become highly assymmetric for high particle velocities and for low

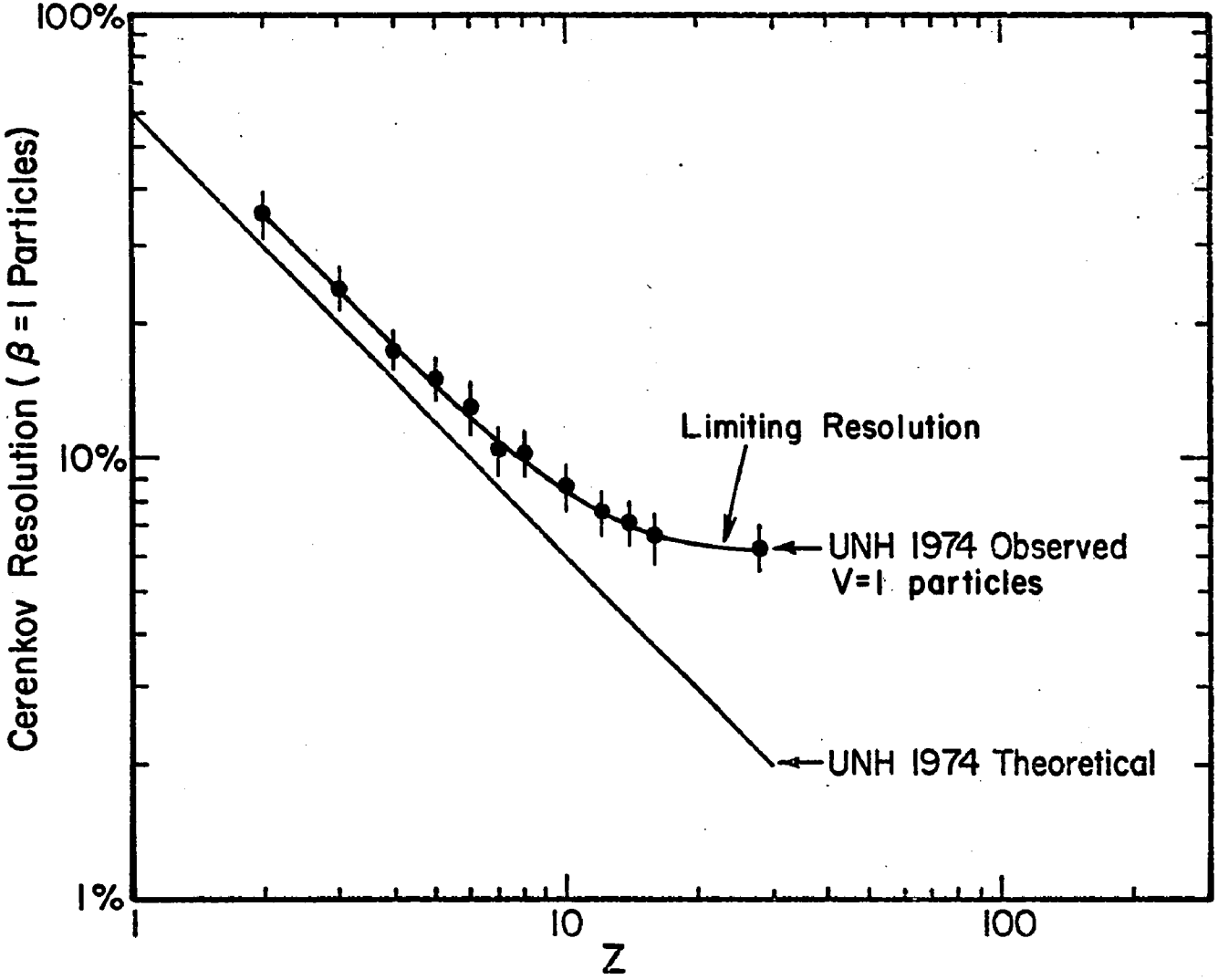

Figure 2.5 Cerenkov Detector Resolutions

Z nuclei (Landau distribution), for velocities and charges of interest in this study, the distribution is essentially Gaussian. The resolution function Qs is

$$Q_s = dE \cdot E_d \left[2 - E_d/E_m \left\{1 - \frac{v^2}{2} + v^2 \ln (E_m/E_d)\right\}\right]$$

where:

dE=energy loss in detector,

Ed=energy of electron whose range is the scintillator thickness, and

Em=maximum transferable energy to a single electron.

We operate in the regime where a simple scaling expression holds:

$$Q_s = KE/(Z \sqrt{X})$$

where:

x=detector thickness

2.4 OTHER SOURCES OF RESOLUTION BROADENING

Pathlength errors, gain variations due to temperature changes, compensation inaccuracy, and photomultiplier gain misalignment all contribute to the limiting resolution, which appears as a constant term that limits the improvement of system resolution with Z. Figure 2.5 illustrates this effect for our Cerenkov detector. For the total energy counters, the resolution is limited across most of the operating range by these sources of error.

3.0 SOME ASPECTS OF EXPERIMENTAL TECHNIQUE

Because of the relative scarcity of the nuclei of interest, the main problem of isotopic composition studies is that of combining sufficient geometrical gathering power with suitably matched high-resolution detecting elements. Balloon-borne instrumentation since 1974 has taken the course of gaining larger geometrical factors by allowing the detecting elements to have some degree of non-uniformity, and using information on the particle trajectory to correct out these non-uniformities. For example, the Goddard (Fisher et al., 1975), St. Louis (Benegas et al., 1975), and Chicago (Dwyer and Meyer, 1976) experiments make use of multiple position sensing elements to completely determine the trajectory of each cosmic ray. Inherent detector non-uniformities are mapped using abundant low-Z species (muons, helium, or carbon), then this map is applied to the other nuclei observed. This method, while in principle ideal, suffers from many limitations, some of which are:

1. complexity of associated equipment;

2. large magnitude of the correction (typically 25%) relative to desired resolution (<2%);

3. non-linear behavior of plastic scintillators (which may invalidate the extension of low-Z maps to higher charges); and

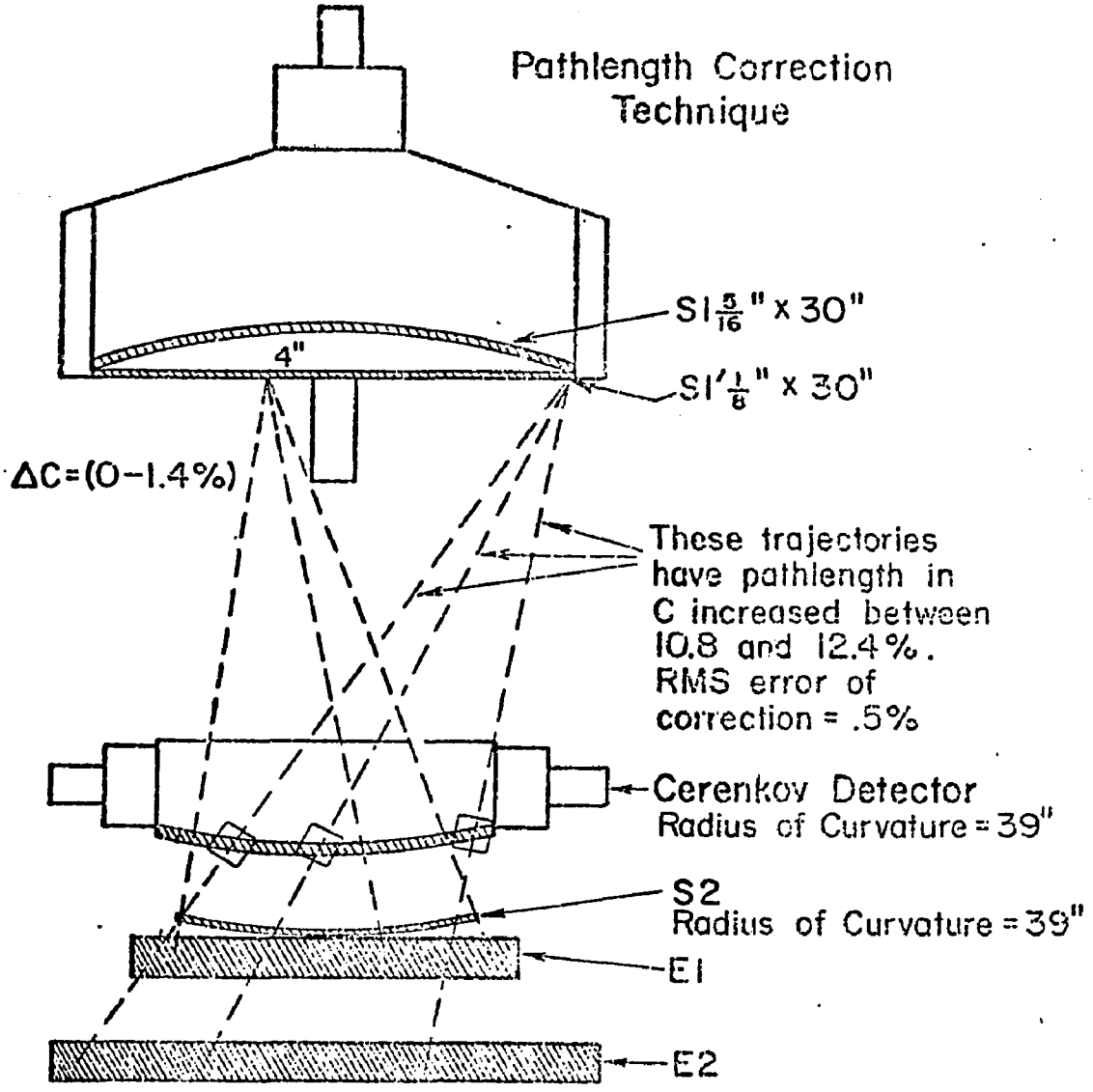

Figure 2.6
Pathlength Correction Technique

4. production of multiple tracks in position detectors (as many as 30% of the total number of events have been rejected for this reason).

Our approach differs considerably from the above, as we discuss below.

3.1 PATHLENGTH CORRECTION

A single piece of trajectory information, namely the radius of the particle from the detector axis, is used in combination with suitably curved detecting elements to reduce "pathlength errors". Pathlength errors are the variations of detector response due to the increased thickness of material encountered along slant trajectories over those which are perpendicular to the detector surface. Details of the pathlength correction technique are given in Appendix 1, while the main ideas are given here.

Figure 2.6 illustrates the effect of pathlength errors. The secant increase of pathlength in C and S2 has the two-fold effect of increasing the output of C and S2 and E1, and decreasing the the energy with which the particle enters E2. But it may also be seen, that due to the curvature in C and S2, if the particle radius in S1' is known, the magnitude of the pathlength error is fixed within rather narrow limits. Therefore it may be corrected out in the

data analysis. Also, since the change in energy loss due to the pathlength increase can be computed, the signal from the detector in which the particle stops can be suitably increased. The importance of this technique is that it allows the instrument elements to be larger and closer together without sacrificing resolution, thus considerably increasing the geometrical factor over comparable resolution curved element telescopes without the radial measurement.

The radial measurement is accomplished in the S1-S1' pair: The S1' plastic is viewed by a single 2" photomultiplier, which is optically coupled to the plastic at its center. The S1' signal is a function of charge, velocity, and radius from the photomultiplier, while the S1 signal is a function only of charge and velocity. Therefore, the ratio S1/S1' contains the radial information, which can be extracted and used to compute the pathlength correction, as described in Appendix 1.

3.2 COMPENSATION

Spatial nonuniformities, which are light-collection variations associated with photomultipler placement, were removed from each detector by airbrushing a diffuse mask of white paint onto the scintillator face. The shape and density of the mask were tested using an electron source to produce a constant light output in a 2 cm. diameter region, then refinements were made until spatial nonuniformities

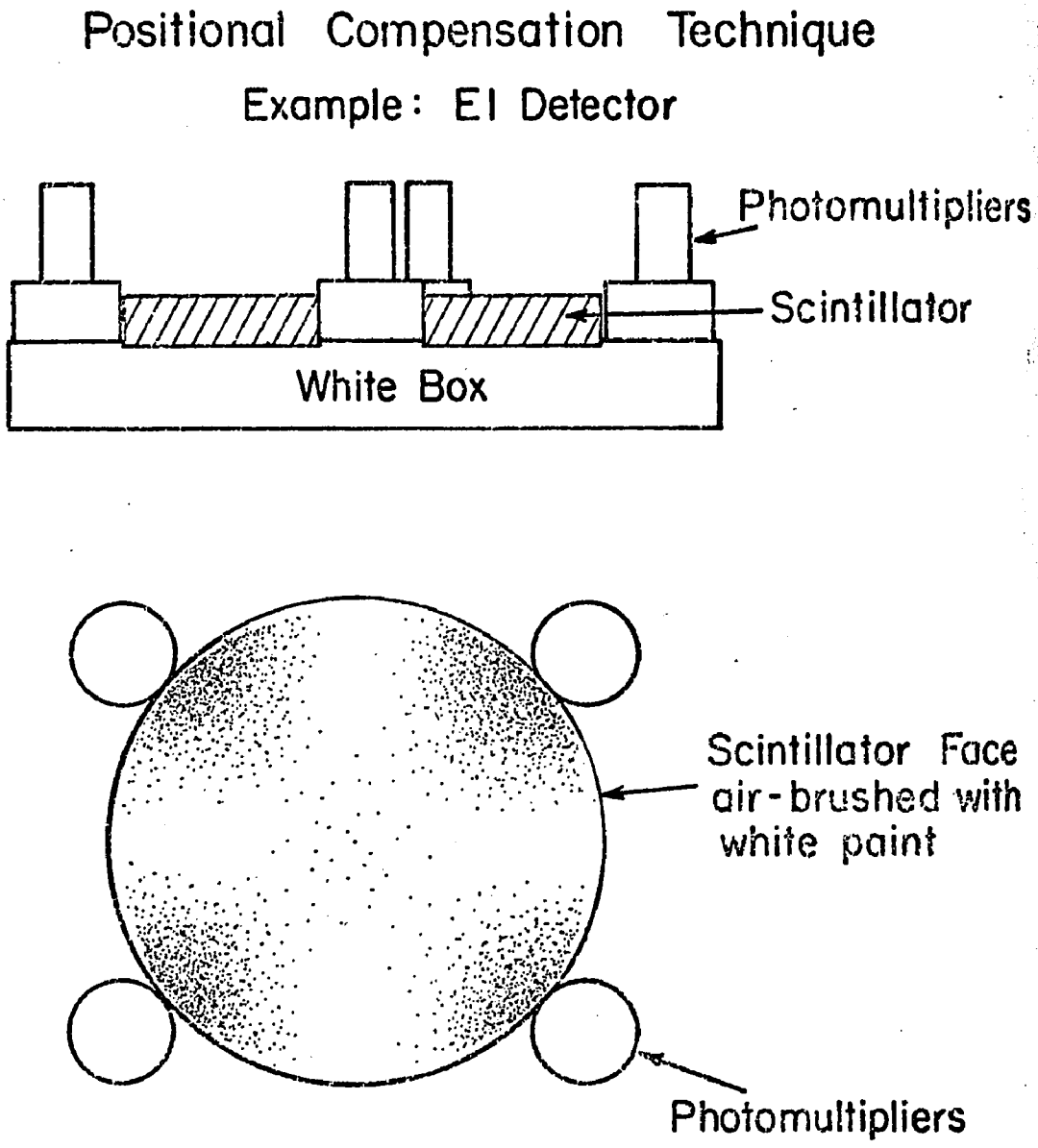

Figure 2.7
Positional Compensation Technique

measured in this way fell below the 1% level. This procedure was followed for S1, S2, E1, and E2. Figure 2.7 represents the compensation pattern for E1. The Cerenkov detector, apparently because of its high light-collection efficiency and large number of photomultiplier tubes, needed no compensation.

3.3 THICKNESS VARIATIONS, PM MATCHING

A requirement of all high resolution particle detection systems is detectors of uniform thickness. This requirement was achieved by wet-grinding the plastic with coarse sanding disks on the side to be painted until the desired thickness tolerances (<.5%) were achieved. It is also crucial that the photomultiplier gains of multi-tube detectors be accurately matched. The significant technical points bearing on photomultiplier tube matching are: 1)-matching at the operating voltage (photomultiplier gain is not sufficiently consistent a function of voltage to allow gross gain changes between tube matching and flight); 2)-wrapping the tubes in mu-metal magnetic shielding, to eliminate orientation effects; and 3)-as far as possible, matching in the detector itself. This last procedure minimizes gain shifts induced by handling and exposure to high light levels. An Am241 alpha particle source coupled to a pellet of NE102 scintillator was placed in the geometrical center of the Cerenkov detector to match its tubes, while the other

photomultipliers were adjusted using muons.

CHAPTER III

EXPERIMENT: DESIGN

We complete the discussion of the physics of the instrument in this chapter, with a study of the equations governing the resolving power of the detector combinations we use, and some predictions of the system performance.

1.0 PRINCIPLES OF MASS-SEPARATION DESIGN

The principles of isotopic separation using the combinations of Cerenkov and total Energy (C x E) and Scintillation and total Energy (S x E) techniques have been described by Webber and Kish (1973). For completeness, we include parts of that discussion here:

1.1 S X E TECHNIQUE

In the non-relativistic approximation, the kinetic energy E and the rate of ionization loss S are given by:

$$E = Mv^2/2$$

$$S = k\left(\frac{Z}{v}\right)^2 \ln\left(\frac{K}{v^2}\right)$$

with:

K, k, k', etc., constants, and other symbols as previously

defined.

The resolving power of simultaneous measurements of S and E may be estimated by combining 1) and 2), obtaining:

$$S = \frac{K'MZ^2}{E} \ln(K''E/M)$$

In this mode one may write a particularly simple expression for the mass separation, if the variation of the logarithmic term is neglected:

$$\frac{dM}{M} = \{(\frac{dS}{S})^2 + (\frac{dE}{E})^2\}^{\frac{1}{2}}$$

This equation conveys the meaning that in this mode the relative separation of masses is a function in which the fractional changes in E and S are weighted equally.

1.2 C X E TECHNIQUE

The energy dependence of the absolute mass separation in the Cerenkov by total energy mode may be studied by combining the theoretical expressions for the Cerenkov and total energy measurements.

$$C = K'Z^2(1-\frac{M}{2En^2})$$

then:

$$dC = C\ (M + dM) - C\ (M) = \frac{KZ^2}{2n^2} \frac{dM}{E}$$

An expression for the fractional mass separation as a function of the fractional Cerenkov resolution, analogous to that given for the S x E analysis, is not available, because the equation in question is transcendental. However, we can

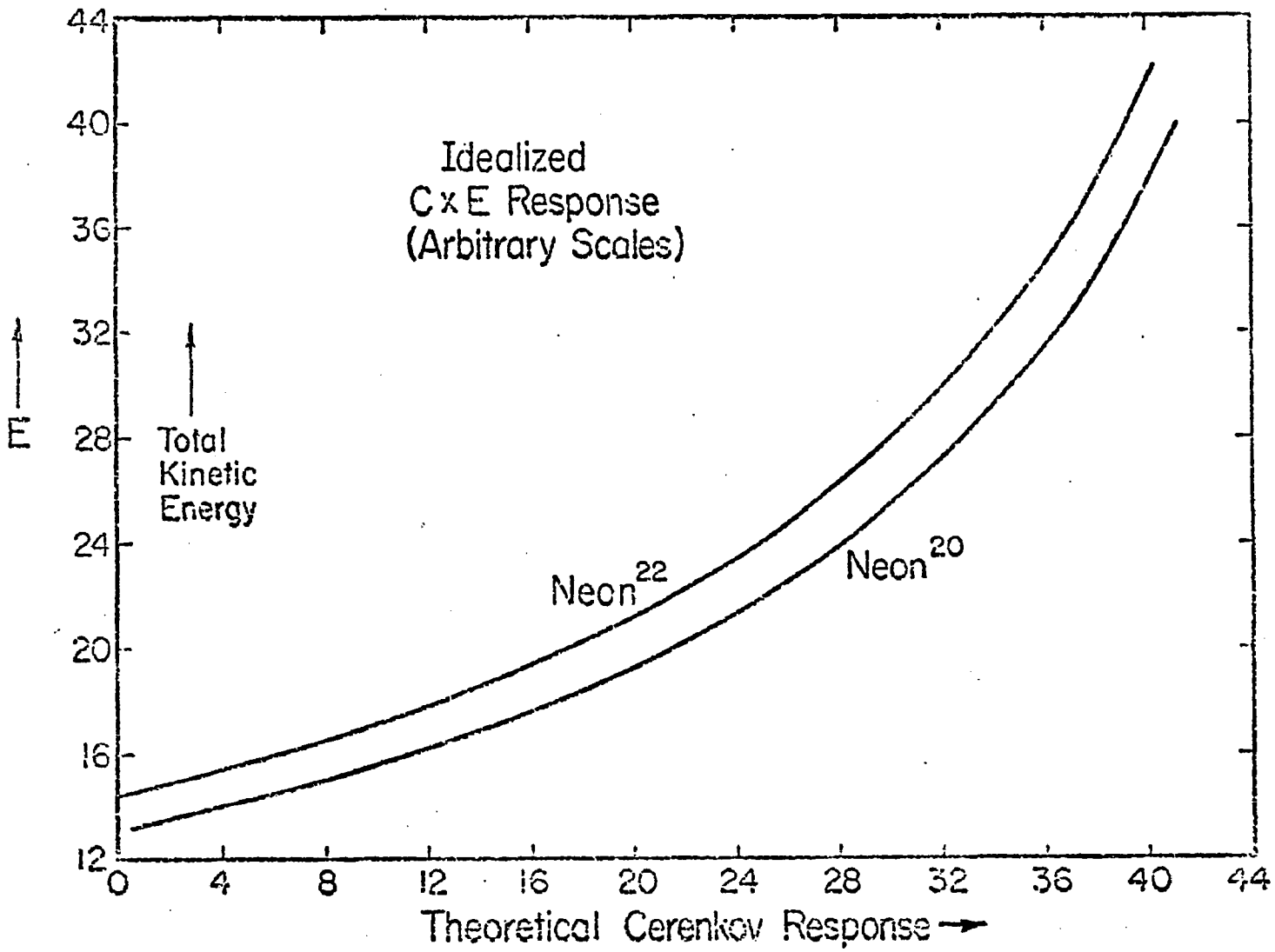

Figure 3.1 Idealized C x E Response: Neon

see from the above expression, the important fact that the absolute separation falls off as 1/E.

Much more information can be obtained with a graphical analysis, which is in fact the usual method for predicting instrumental performance. As an example, we show on Figure 3.1 the theoretical Ne-20 and Ne-22 Cerenkov response C plotted versus the particle kinetic energy E, from which the theoretical mass separation may be obtained. Assuming that our kinetic energy measuremement is made with perfect resolution, the relative separation which is of interest is that in the C-dimension, dC/C. Shown on Figure 3.2 is the calculated relative C-dimension separation/AMU of the Neon isotopes determined from Figure 3.1 as a function of particle kinetic energy/nucleon, and the Cerenkov counter resolution, based on our measured v=1, Z=1 resolution of 26%. We observe that near the Cerenkov threshold of 320 Mev/n, there is a region where the relative separation is infinite, because Ne-22 is not above the threshold. We also note that at high energies, the mass separation is decreasing, approaching the 1/E fall-off theoretically predicted. However, the resolution is improving less rapidly, so that as the energy increases the mass separation reaches a point where isotope resolution is no longer possible.

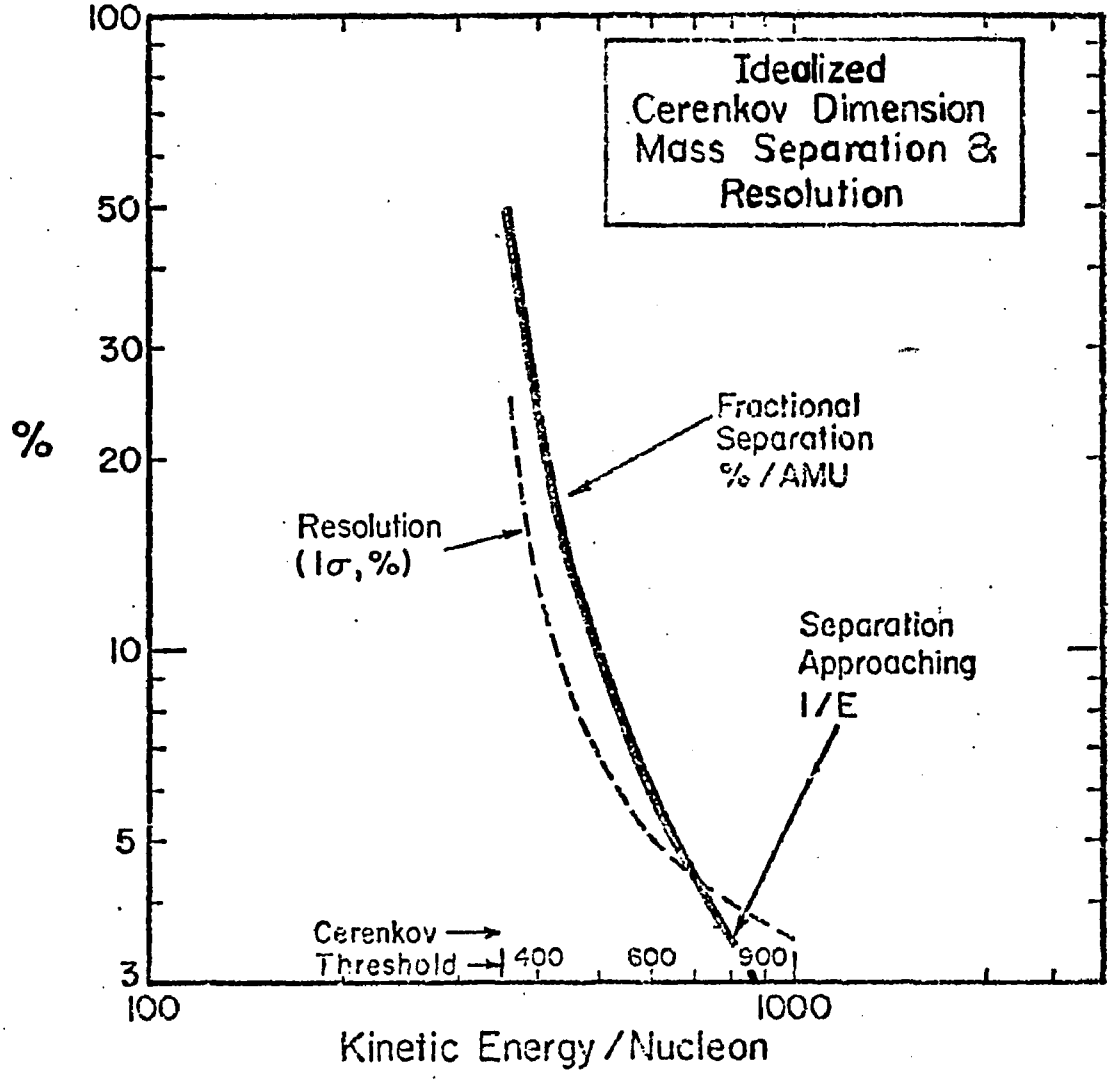

Figure 3.2

Idealized CxE Resolution and Mass Separation

2.0 PREDICTED RESOLUTIONS AND SEPARATIONS

We now consider the separation of charges and isotopes predicted by a more complete model of the system, and the resultant power of the system to identify the charge and isotopic mass of nuclei.

As we have noted, the situation treated in section 1.0 is highly idealized. If one could make simultaneous measurements of differential energy loss, Cerenkov light output, and residual energy, one could work from the theoretical figures and equations given to derive the particle's charge, mass, and energy. But in fact one is constrained to make measurements at different points on the trajectory. And further, with scintillation detectors, one measures not the differential or residual energy deposit, but the light output of the scintillator, which is a non-linear function of charge, mass, and energy deposit. The equations only indicate that species separation is in principle achievable. To accurately predict the instrumental response, it is necessary to calculate the output of each detector to primary particles of energies, charges and masses spanning the range of interest, taking into account the slowing down of the particles as they traverse the instrument material, and considering the measured or predicted non-linearities of each detector.

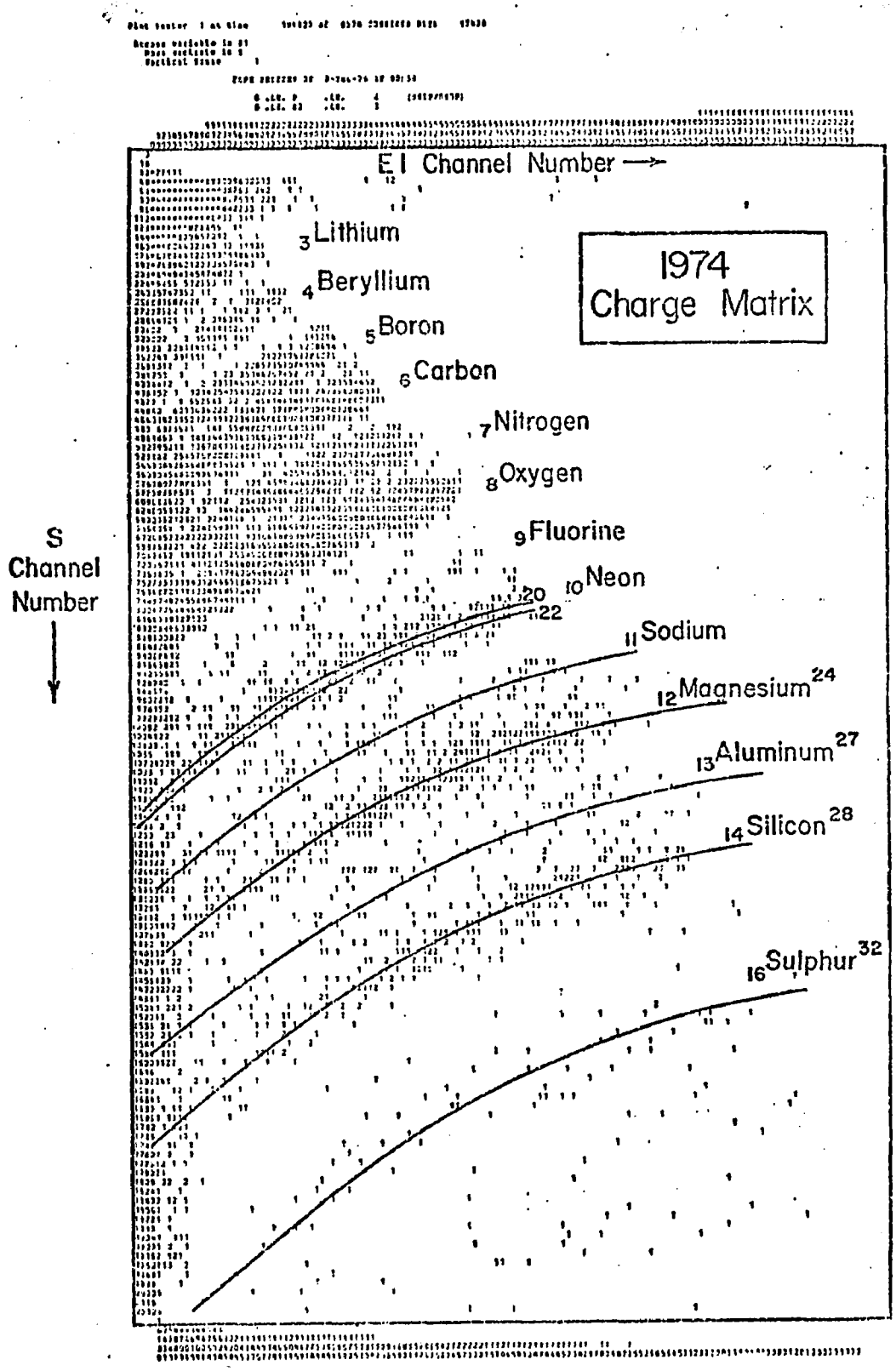

Figure 3.3 S x El Matrix

Before continuing further with the details of the design process, it may be helpful to familiarize the reader with the commmon method of data presentation, which is in the form of two-dimensional scatter plots, or matrices. Along each axis is the output of one detector, scaled as desired to magnify or diminish specific features of the matrix. Each event is represented as a count at the coordinates labeled by the detector pulse heights for that event. This is a powerful method of presentation, giving a visual representation of the separation of species, and showing without prejudice the system resolution.

Figure 3.3 is a matrix showing the charge separation in the S X E mode for the elements Lithium through Sulphur. The tightness of the clustering of events about the fitted lines reflects the resolution of the E and S detectors. These resolutions can be measured for each element by forming a histogram of the number of events as a function of distance from the charge line, for all the events of each charge. The relative separation of the different species can also be measured directly from Figure 3.3. We will present many examples of matrices below, to establish a strong connection between the raw data which they present, and the analysis which follows.

Now let us continue with our discussion of the design of the system.

MODE 1: S x E CHARGE and ISOTOPE ANALYSIS

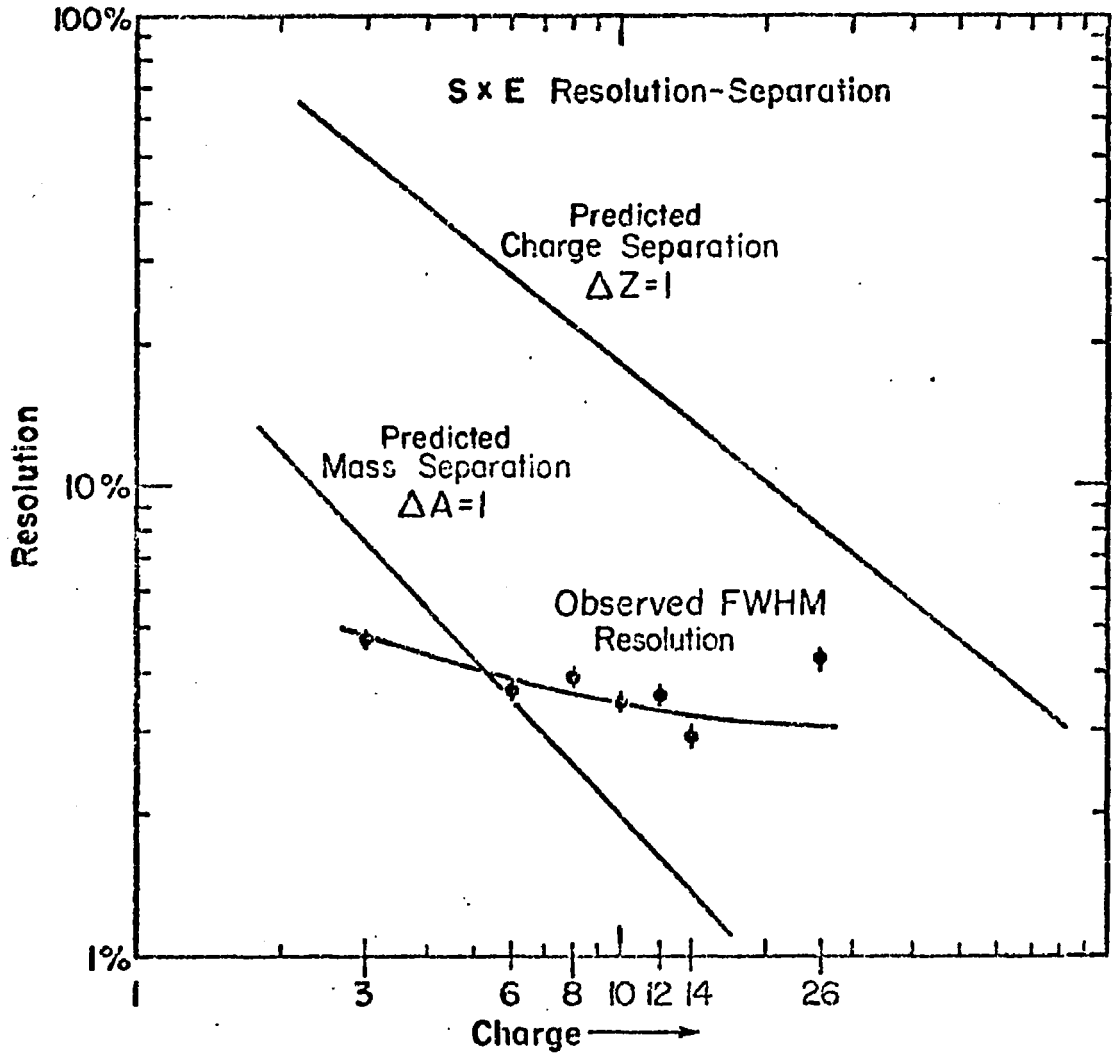

Figure 3.4 S x E Resolution-Separation

Particles which come to rest in either E1 or E2 can be analyzed for charge, mass, and energy by combining the E information with that given by the dE/dx elements S1 and S2. We saw on Figure 3.3 the clear resolution of the charges which is given by this mode. The separation of masses shown is about 1/7 that of the charges.

Shown in Figure 3.4 are the dE/dx resolution (Qs) as measured in the flight data, and the separation of adjacent isotopes and charges as predicted from analysis of the energy deposits in each detector and the detector response functions (ch IV). Since it is usually required that the FWHM instrumental resolution be less than the separation in order to achieve resolution of equally abundant species, we see that isotopic separation is feasible with this mode only until about Z=8. At higher Z, the C x E analysis provides isotopic separation, but the S x E mode is still essential for charge resolution. The charge resolution is seen from Figure 3.4 to be adequate to separate equally abundant elements well beyond Z=26.

MODE 2: C x S CHARGE ANALYSIS

Another mode of analysis, useful for additional charge information, is the C x S mode. In this mode we confirm that the charge information implicit in the Cerenkov output agrees with that obtained from the S x E analysis. A C x S matrix of the charges Neon through Sulphur is shown in

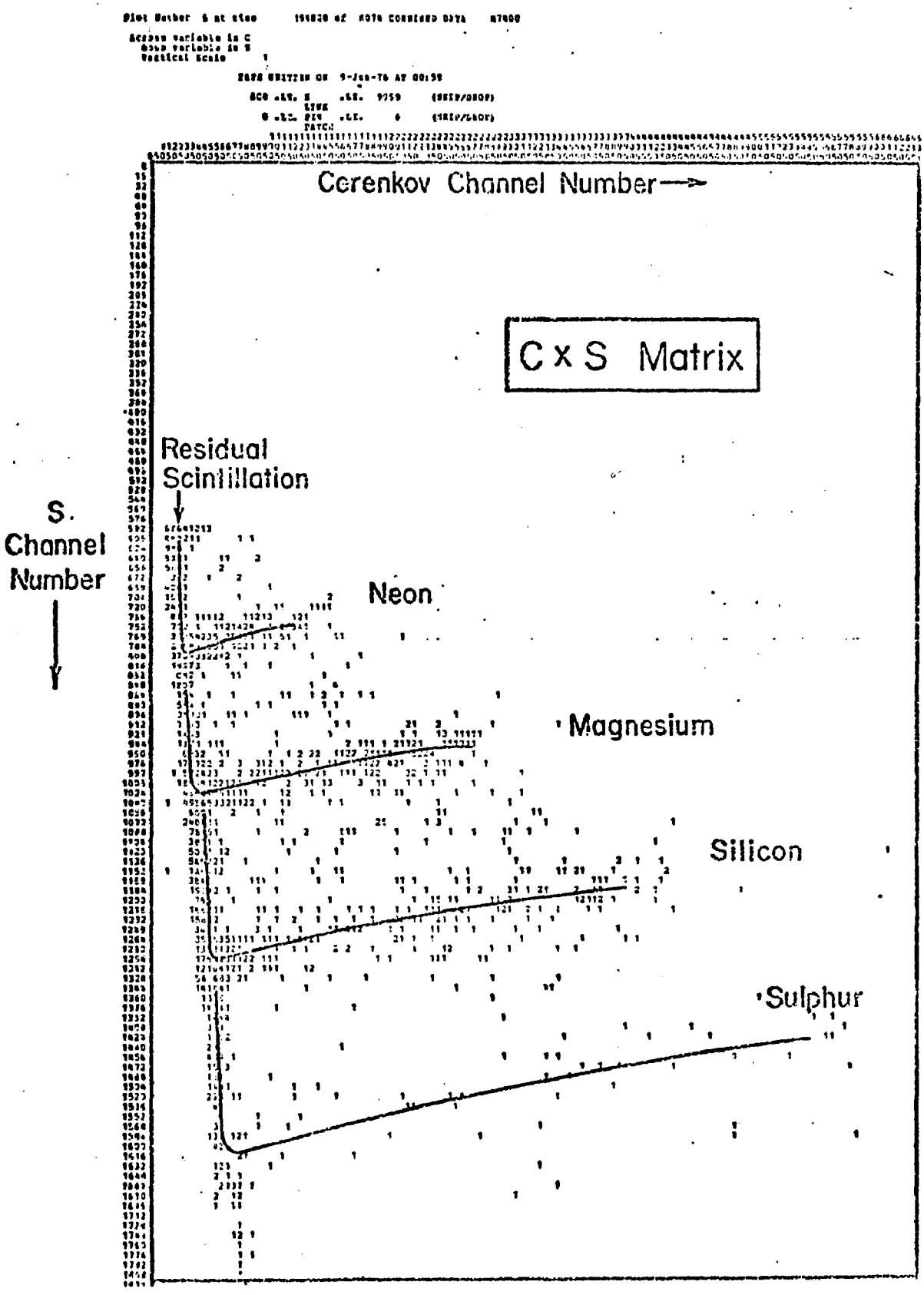

Figure 3.5 C x S Matrix

Figure 3.5. An interesting feature is present in this matrix which we have not seen previously. This is the presence of two components in the response of a single detection element. On the left of the matrix, the heavy band of events is due to those events which are below the Cerenkov threshold. They still produce a small amount of light, due to a low level of scintillation in the plastic. At the Cerenkov threshold, each element is seen to break sharply away from the residual scintillation and move up to the right. This behavior follows the decrease of energy loss in S as the particle energy, and the Cerenkov output becomes higher.

Full advantage of the redundancy of charge definitions in the C x S and S x E modes is obtained when the charge assignments in each of these modes are plotted against one another, allowing a two- dimensional charge selection for each event. We will show examples of this two-dimensional charge assignment in Chapter IV.

MODE 3: C x E ISOTOPE ANALYSIS

The key to obtaining realistic predictions of isotope resolution in the C x E mode is to determine the expected separation of isotopes from graphs such as that shown in Figure 3.6, in which the C and (E1+E2) outputs have been converted to pulse height channel scale. This Figure has been constructed using the predicted Cerenkov output and

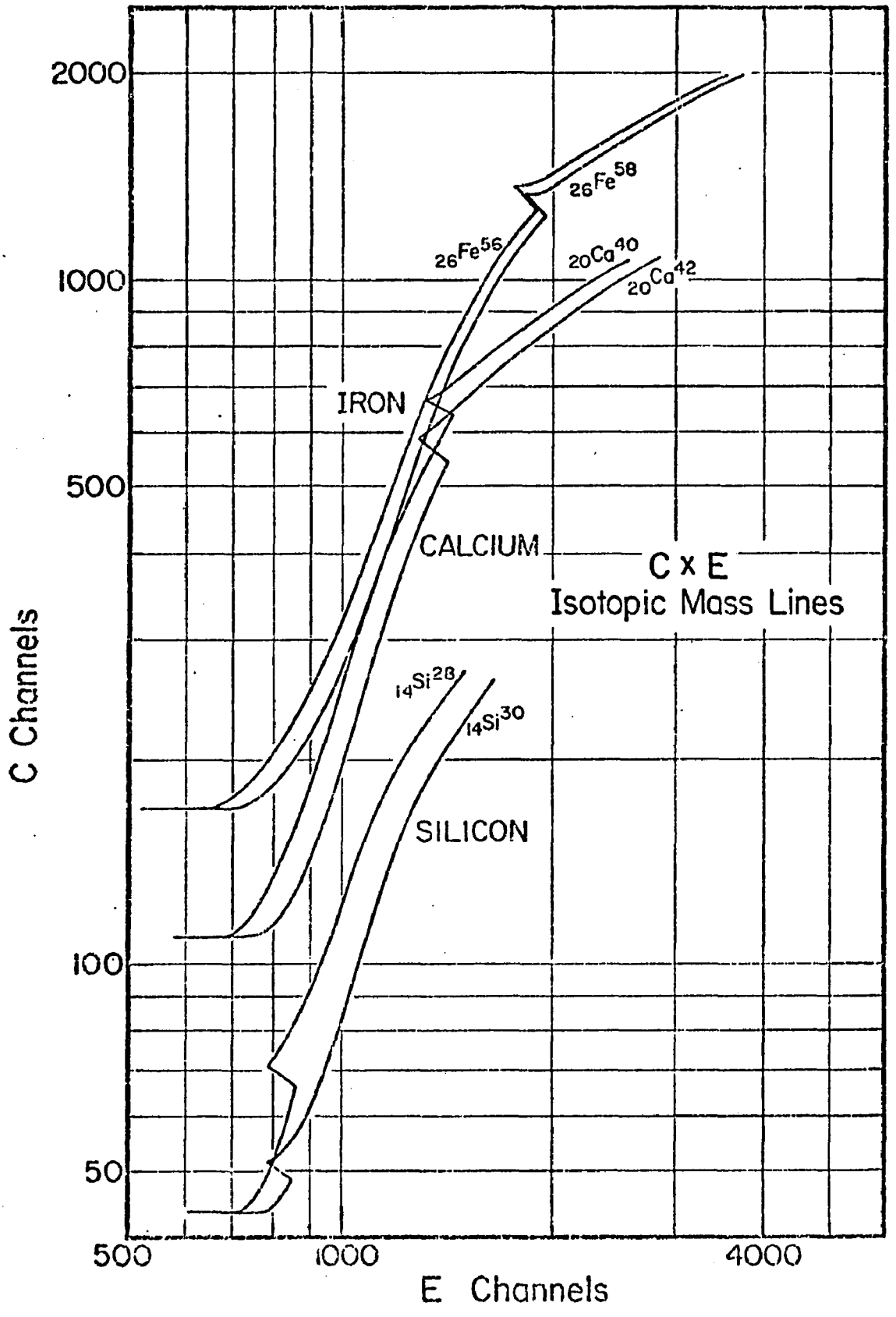

Figure 3.6 C x E Isotope Lines

E-counter energy deposit, in conjunction with a detailed specification of each detector's non-linearities (response function). By measuring the fractional separation of isotopes in both dimensions, and comparing these separations to the resolutions of the corresponding detectors, we can predict the mass resolution. Figures 3.7, 3.8, and 3.9 illustrate this result for three charges of interest by showing the separation and the resolution on a common scale. The scale chosen is C/Cmax, the Cerenkov output referenced to the maximum Cerenkov output for v=1 particles of each charge. An important feature of these three resolution-separation diagrams, which can also be noted on Figure 3.6, is the fall-off of mass separation as the Cerenkov output grows. This observation implies that there is an optimal zone for mass analysis of any element, which is specified by the resolution-separation diagrams. This zone arises because residual scintillation degrades the mass separation just above the Cerenkov threshold, and because the 1/E fall noted earlier dominates the mass separation at high energies. We will find this prediction of great value in our analysis of the flight data (Chapter IV).

The resolutions which we have shown on Figures 3.7, 3.8, and 3.9 are calculated neglecting the fluctuations introduced by knock-on electrons, but including the effect of residual scintillation. We have described the net resolution by:

$$Q_C^2 = \left(\frac{.255}{Z}\right)^2 \left(\frac{C'-Sr'}{C-Sr}\right) + (.0234)^2$$

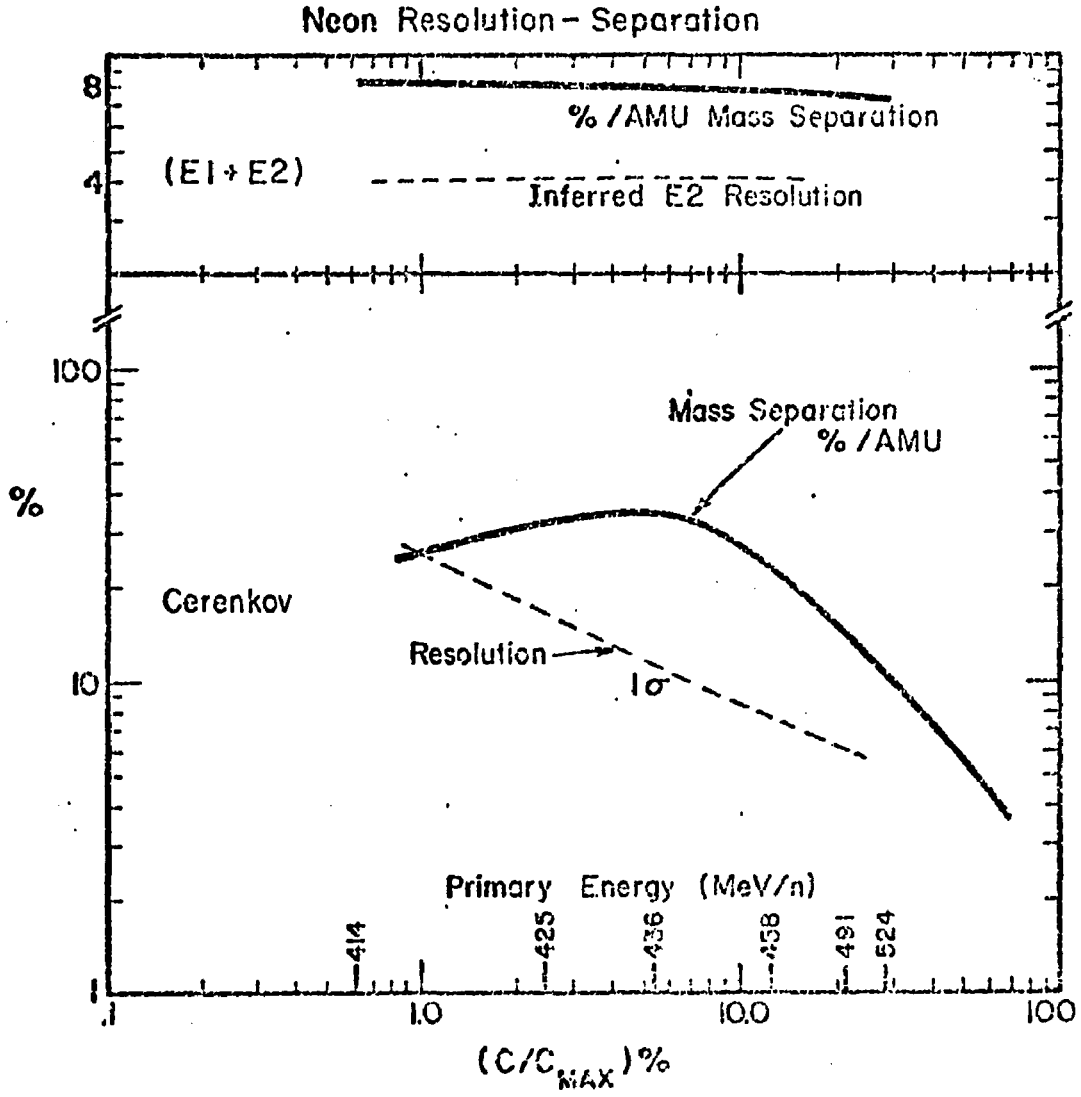

Figure 3.7 Neon C x E Resolution-Separation

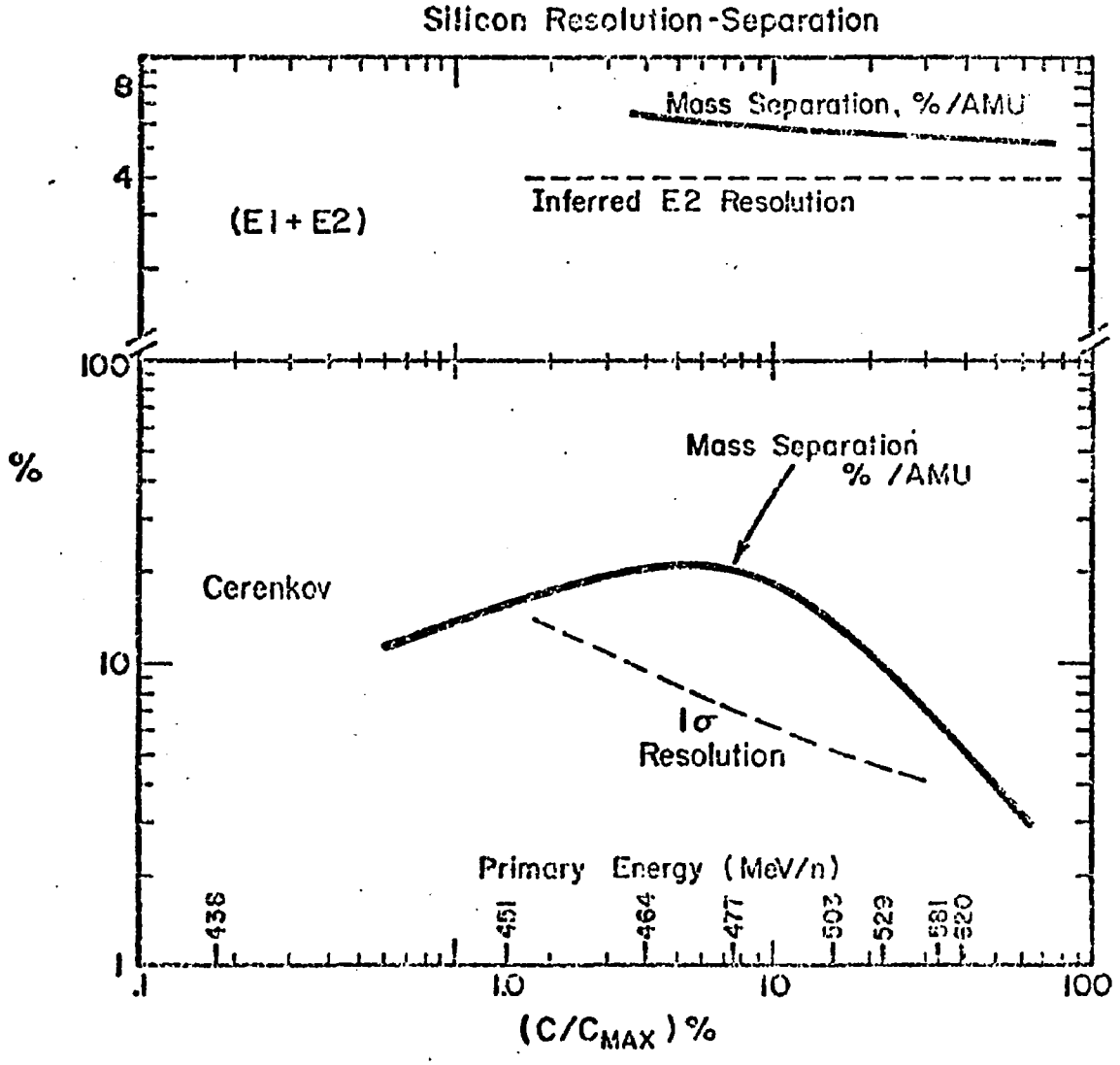

Figure 3.8 Silicon C x E Resolution-Separation

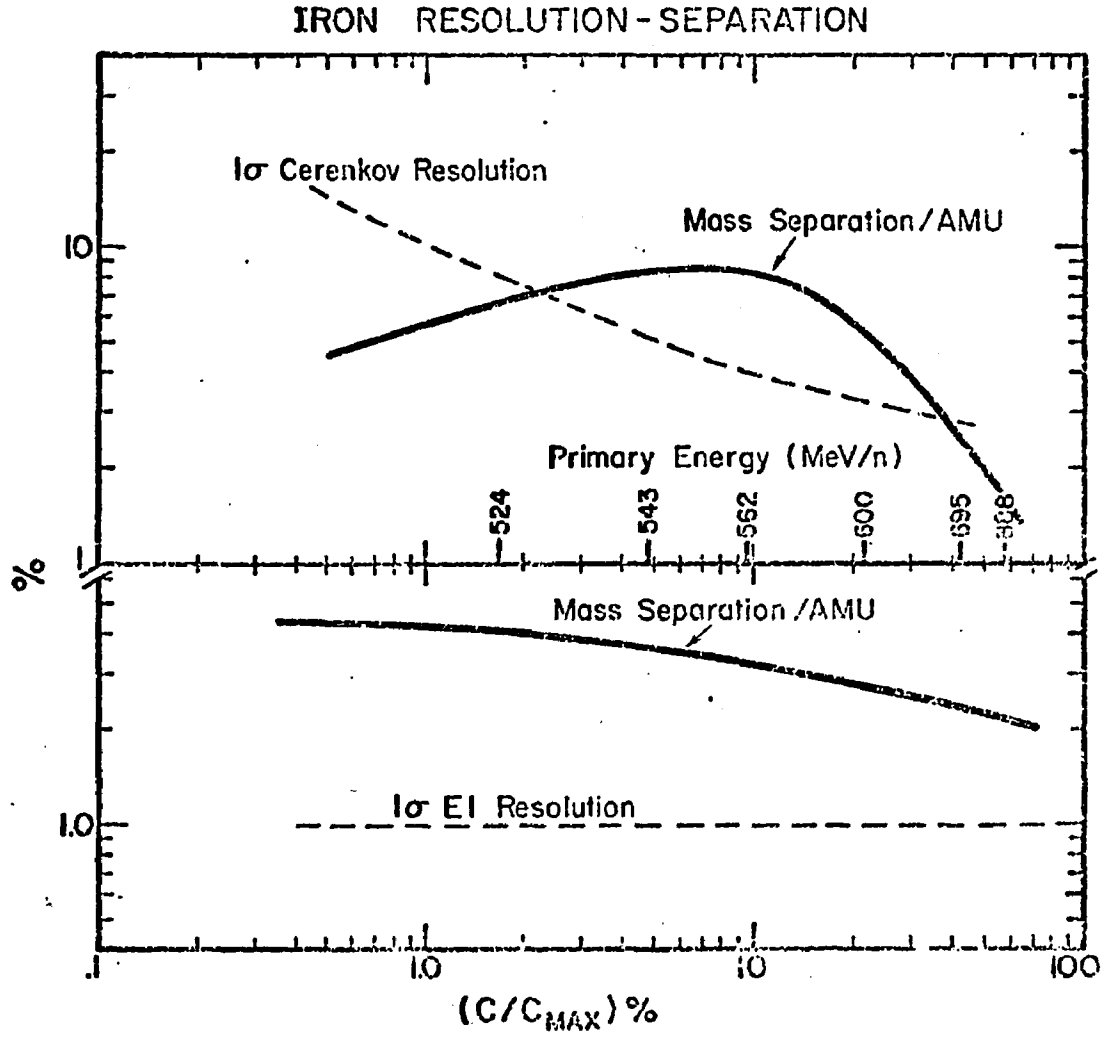

Figure 3.9 Iron C x E Resolution-Separation

where:

Sr is residual scintillation,

Sr, C refer to the velocity of particle studied,

Sr' C' are for v=1 particles of the same species,

0.255 is the resolution at Z=1, v=1 (muons), and

0.0234 is the limiting resolution observed in Figure 2.5.

CHAPTER IV

DATA ANALYSIS

1.0 INTRODUCTION

The task of collecting and converting the series of ten billion telemetry bits representing pulse amplitudes in each of the eight detectors of the experiment into isotopic mass histograms required considerable care and computational effort. The principle steps taken to obtain the abundance results at the detector were:

1. data collection during the balloon flights
2. transcription of telemetry data from video tape to record format computer tape
3. temperature correction and removal of Helium data
4. inter-flight normalization
5. pathlength effect correction
6. background rejection with consistency criteria
7. calibration of the instrument response from flight data

8. charge and mass assignments for each event using the derived calibration

This chapter describes the background rejection using consistency criteria, the instrument calibration from the flight data, and the charge and mass assignments. Steps 1,2,3, and 4 are described in Appendix 2. The pathlength correction technique (5) is described in Chapter 2 and in Appendix 1.

2.0 BACKGROUND REJECTION USING CONSISTENCY CRITERIA

As we have pointed out in Chapter II, at the energies we are considering, nuclei are relatively fragile, often fragmenting when they collide with other nuclei. About 50% of the incident particles which we would like to analyze in the C x E mode are lost due to fragmentation in the instrument. These fragments constitute a large source of background which can obscure our results unless they are thoroughly removed. We employ a battery of three interaction-rejection techniques to remove from consideration particles which suffer alterations in their charge while traversing the instrument. Particles which are altered in mass alone cannot be rejected by these techniques, and must be corrected for in the data analysis (Chapter V).

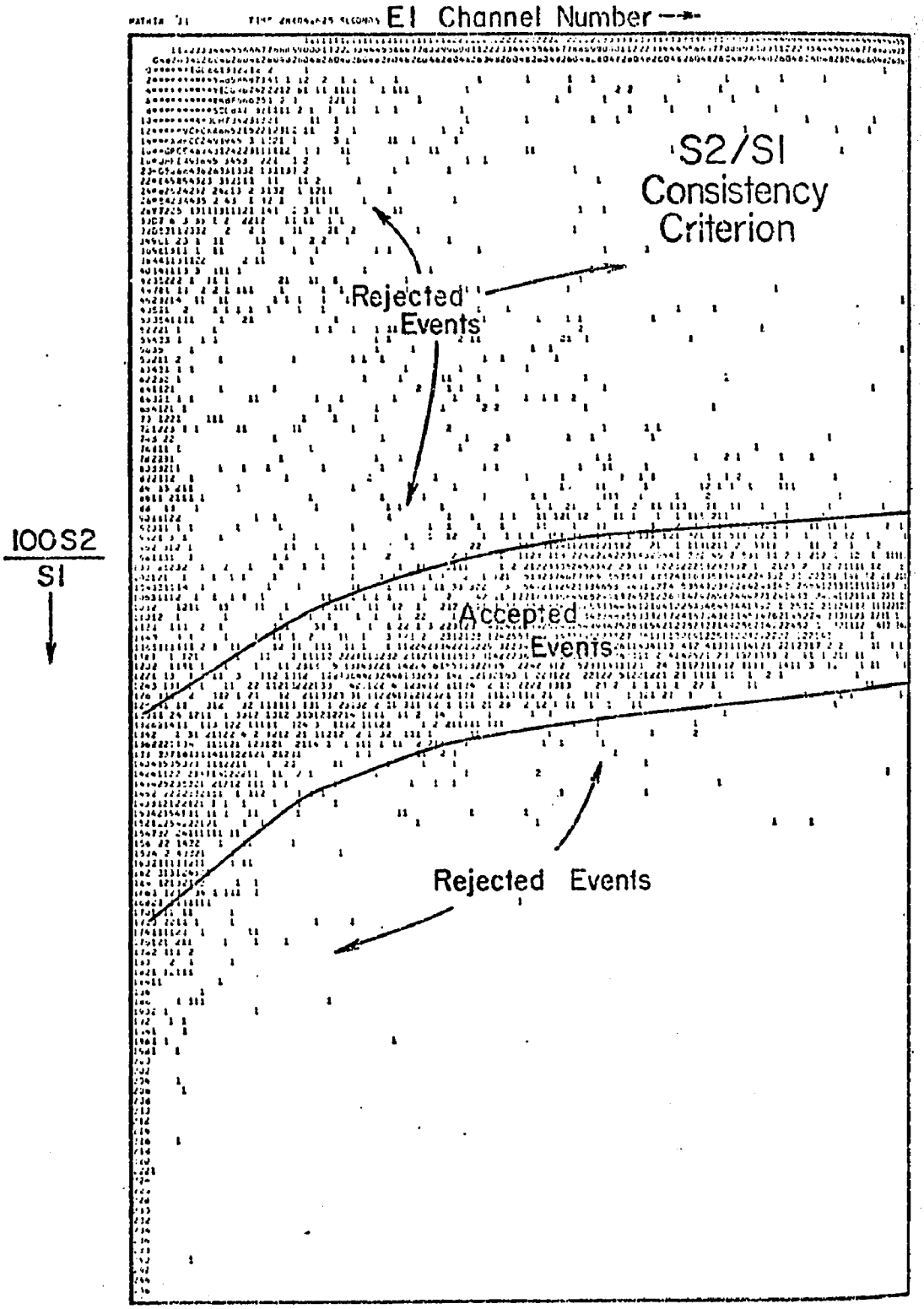

Figure 4.1 S2/S1 Consistency Criterion

2.1 S2/S1 CRITERION

The two dE/dx detectors S1 and S2 provide a redundancy which is a powerful tool for interaction rejection. The ratio S2/S1 is a suitable parameter to consider. Figure 4.1 shows this ratio plotted versus the E1 pulse height for a sample of particles which stop in E1. The matrix shows clearly that there are two distinct regions. One, in which the pulse height in S2 is similar to that in S1, is from particles which do not undergo charge-altering fragmentation (within boundaries). The second region, outside the boundaries shown, consists of particles whose S2 pulse height is more than three standard deviations from the mean of the distribution . We form criteria like that shown in Figure 4.1 for each case of particles stopping in E1, those stopping in E2, and those which penetrate the instrument. The S2/S1 criterion eliminates mainly events in which a change in charge occurs before S2. In this case, we estimate that it rejects 95% of the total number of interacting events, and less than 5% of the non-interacting events.

2.2 E1 X S CRITERION

A second charge-consistency criterion may be applied to particles which stop in E2. In this case E1 provides another dE/dx measurement. Figure 4.2 shows the matrix of S x E1 for Z=10 to 16 particles which stop in E2 (no PEN

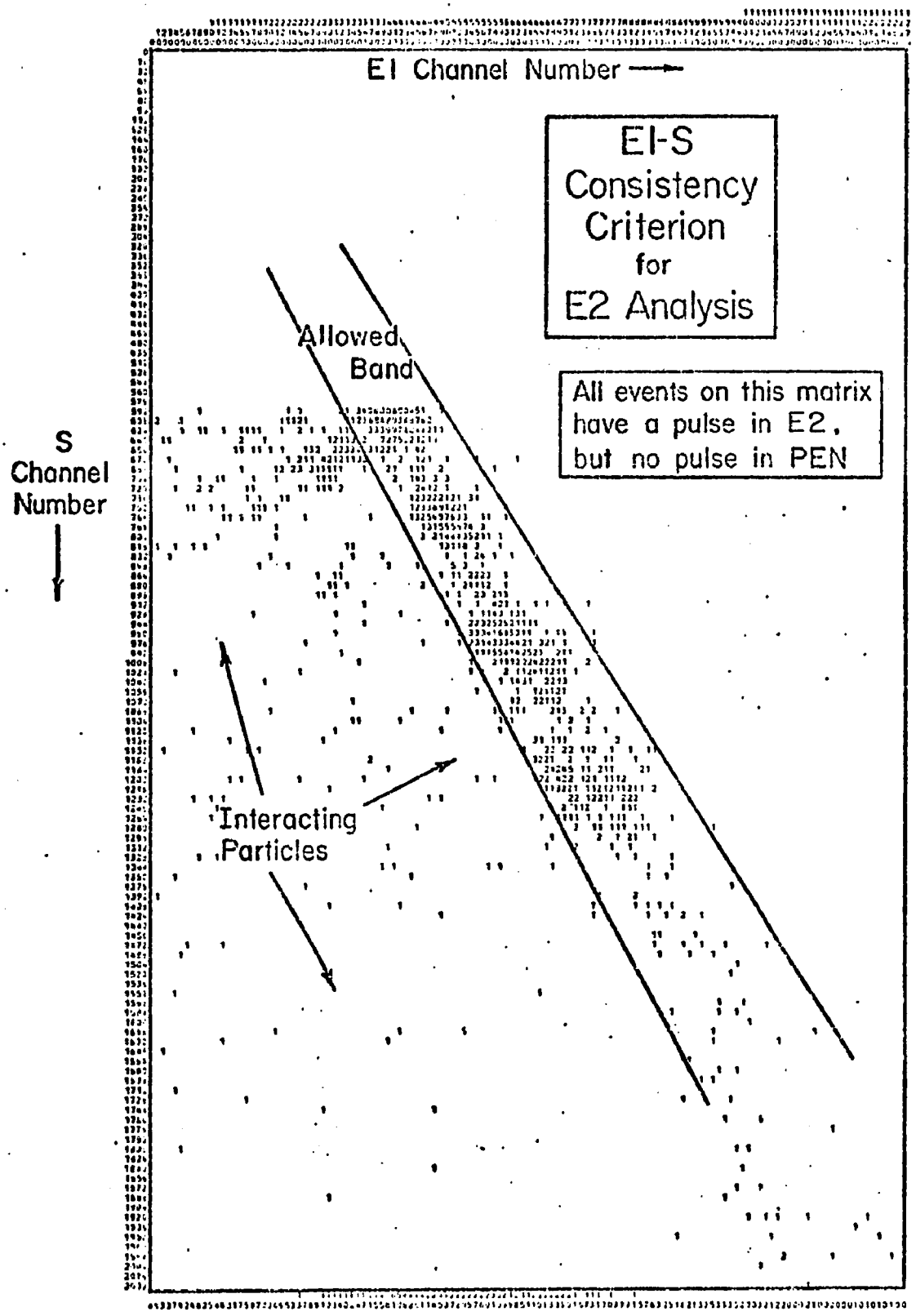

Figure 4.2

S x E1 Matrix: Consistency Criterion for E2 Analysis

pulse). We demand agreement between these dE/dx measurements by choosing the region shown on the matrix, which is the only region allowed for particles which stop in E2 but do not fragment.

2.3 FRAGMENT SIGNAL CRITERION

About 1/2 of the total interaction cross-section of high-Z nuclei goes into the peripheral reactions, which result in a particle of low Z fragmenting from the primary nucleus. Because the range of this particle is much greater than that of the primary which generated it :

$$\text{Range(proton)} = Z*Z/A \times \text{Range}(Z,A)$$

we have a powerful interaction signal. A small pulse in the counter below the nominal stopping counter signals an interaction.

The power of this tool for rejecting interactions which occur before E2 can be seen in Figure 4.3, which shows the matrix of S x E1, when a pulse is produced in E2. The trail of pulses to the left of the main distribution is in the same region as particles which produce no pulse in E2; we would treat these particles as valid stopping events were it not for the pulse in E2. If these particles had not fragmented, it would be impossible for them to produce a pulse in E2, because their kinetic energy, as measured in E1 is too low. Also shown on this figure is the distribution

INTERACTION REJECTION BY

FRAGMENT SIGNAL CRITERION

Primary Z,A	Depth from Top of Atmosphere	Remaining Kinetic Energy (MeV/n)	Range of Proton Fragment gm/cm²	Range of Deuteron gm/cm²	Residual Range gm/cm²	Medium	gm/cm² to E2	
26,56	0	600	175	350	14.55	AIR	16.13	
(600 MeV/n)	2.8	520	141.8	283.6	11.75	AIR	13.3	
	4	480	110	220	9.1	INSTRUMENT	12.1	
	6	410	86	172	7.1	INSTRUMENT	10.1	
	8	335	61.6	132.2	5.1	INSTRUMENT	8.1	
	9	295	49.6	99.2	4.1	INSTRUMENT	7.1	
	10	248	37.5	75.0	3.1	INSTRUMENT	6.1	
	11	199	25.4	50.8	2.1	INSTRUMENT	5.1	
	12	138	13.4	26.7	1.1	E1 / INSTRUMENT	4.1	
	12.6	85	6.12	12.24	0.5	E1 / INSTRUMENT	3.5	
	13.0	37	1.29	2.58	0.1	E1 / INSTRUMENT	3.1	← Fragment can't reach E2
							gm/cm² to PEN	
10,20	0	470	120.54	241	24.1	AIR	24.1	
(470 MeV/n)	2.8	438	107	214	21.3	AIR	21.3	
	6	395	79.7	159	15.9	INSTRUMENT	18.1	
	9	344	64.7	129	12.9	INSTRUMENT	15.1	
	12	294	49.7	99	9.9	INSTRUMENT	12.1	
	15	240	34.7	75	6.9	INSTRUMENT	9.1	
	17	195	24.7	49	4.9	INSTRUMENT	7.1	
	19	145	14.7	29	2.9	INSTRUMENT	5.1	
	21	77	4.71	9.4	0.94	INSTRUMENT	3.1	
	21.6	44	1.72	2.34	0.34	INSTRUMENT	2.5	← Fragment can't reach PEN

Table 4.1

Interaction Rejection by
Fragment Signal Criterion

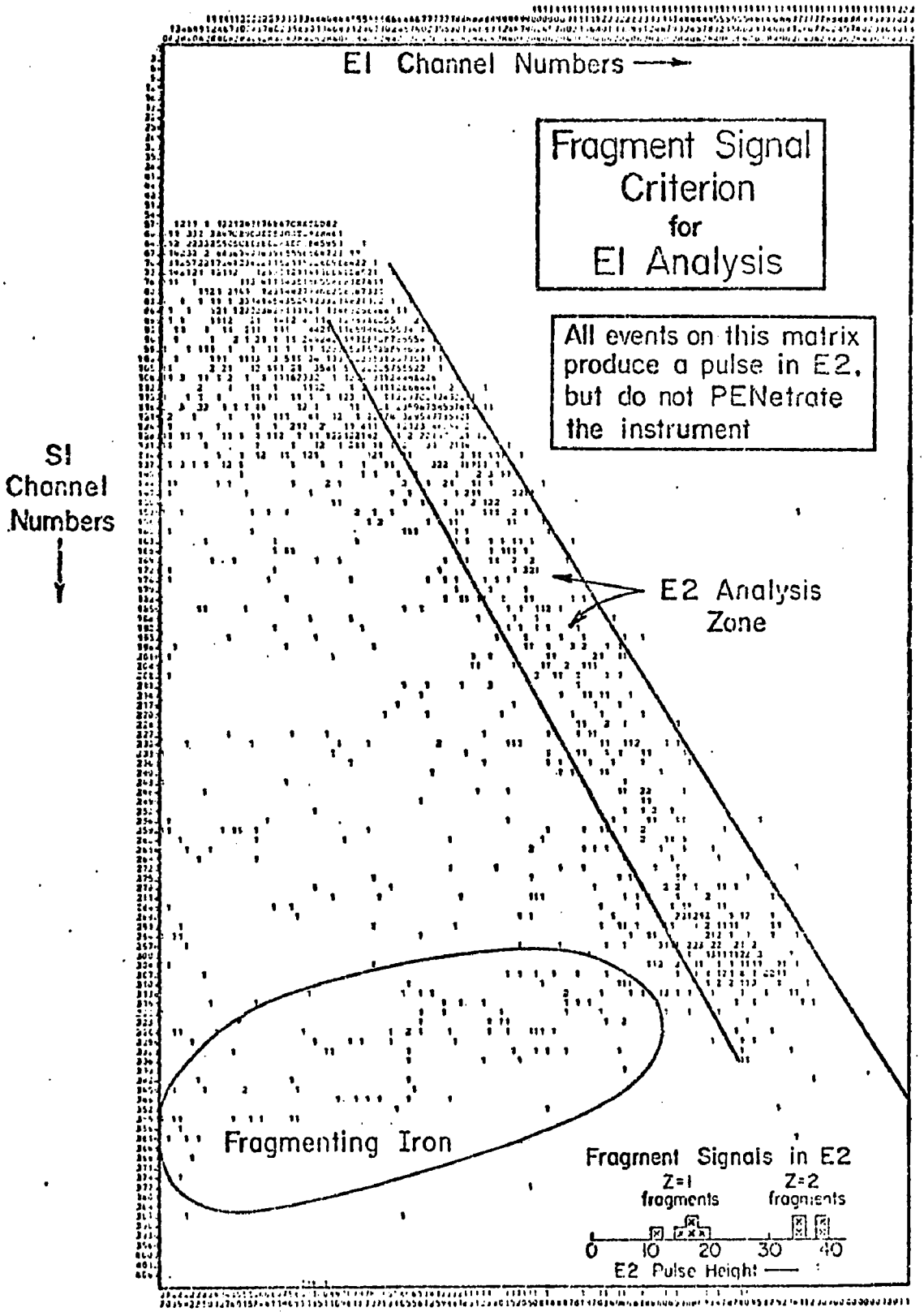

Figure 4.3

Fragment Signal Criterion for E1 Analysis

of pulse sizes in E2 for a sample of these particles which have apparently interacted. The pulse distribution is consistent with charge 1 and charge 2 fragments.

It is revealing to study the mechanism in more detail: Consider two cases: 1) an Iron particle with the median energy of those we analyze (600 Mev/n), which stops half way through E1, and 2) a Neon cosmic ray of 470 Mev/n, which is the mean energy of particles of this charge we analyze. The Neon particle stops two-thirds of the way through E2. Table 4.1 shows in columns 4 and 5 the ranges of protons and deuterons which are fragmented from the incident nucleus (assumed at constant Mev/nuc). The instrumental depth to E2 (or PEN) is shown in column 8. It is seen that any fragment of mass 1 or 2 has enough range to trigger E2, except at the very lowest energies.

In the case of fragmenting particles which have been slowed sufficiently that low mass fragments do not leave the stopping counter, we do not have a fragment signal criterion, but we do observe in the stopping counter all of the primary kinetic energy, less only the difference in binding energies of the intial and fragmented particles (<10 Mev in all cases, or .1%, of the E1 energy deposit). The fragment signal rejection mechanism is not perfect, because fragments may leave the instrument geometry; however, we estimate that less than 7% of the interactions will escape this criterion on this account.

3.0 INSTRUMENT CALIBRATION: AN OVERVIEW

In order to form mass histograms, we must assign mass lines which describe the mean location of each isotope on the matrices. The accurate assignment of these isotopic line coordinates is the most critical task of the data analysis, because inaccurate assignments can result in broadening of the histograms, and/or isotopic mis-identification. The main problem in this task is unfolding the non-linear response of the plastic scintillators, which is uncharted except by the flight data itself. This section describes in general terms the procedure for calibrating the instrument from the flight data.

3.1 SCINTILLATOR RESPONSE FUNCTIONS FROM FIDUCIAL DATA

Calculations using range-energy tables to give accurate estimates of the energy deposit in each detector, as a function of incident Z, A, and primary energy, are widely employed to give a first approximation to the response of scintillation detectors. The factor which converts energy deposit to pulse height channels (so giving the exact detector response) reflects the product of detector gain and scintillator saturation effects. We denote this factor as (ch/Mev). When (ch/Mev) is known to sufficient accuracy for all detectors, nuclides, and energies of interest, the mass line assignment problem is solved. We use the term

"response function" to describe the complete specification of (ch/Mev) for any detector.

The process of constructing the response function is iterative, involving several stages of feedback among the data, histograms, and response function charts. Fiducial point data provide the initial conditions for the construction of the response functions. The fiducial points are (for each charge or isotope):

1. E1 begins to respond (E1=0)

2. E1 maximum energy deposit is obtained (E1max)

3. E2 begins to respond (E2=0)

4. E2max

5. Response of minimum ionizing particles (v=1).

Also available are isotopic mass lines themselves, which can be visually observed in the data in the region where the resolution is <1AMU, and sufficient statistics prevail. This information is especially valuable near the Cerenkov threshold.

Before continuing, it is helpful to define "sufficient accuracy". Figures 3.7, 3.8, and 3.9 showed examples of the isotopic separation expected in the C x E analysis. Our total energy response function is sufficiently accurate if

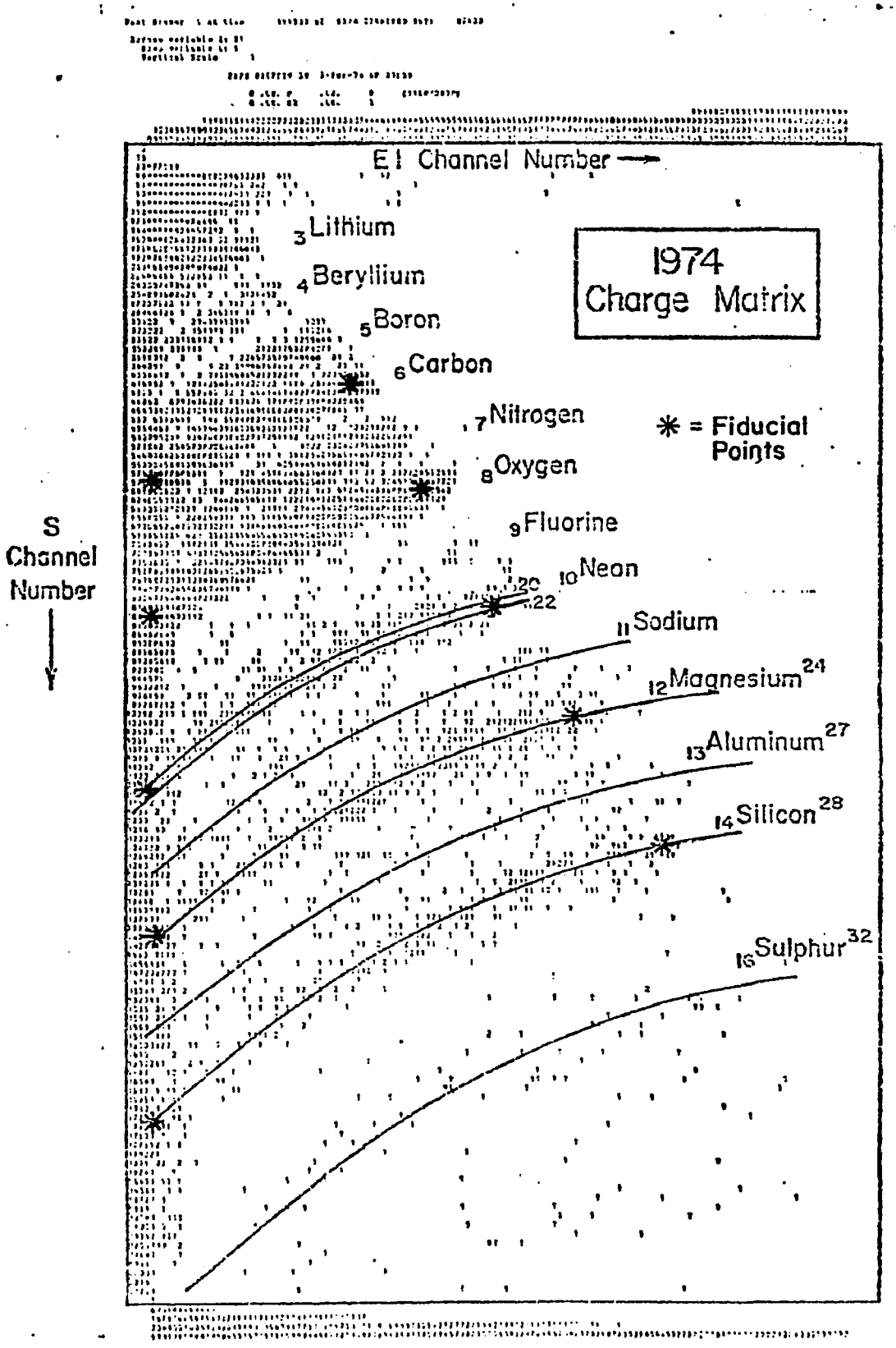

Figure 4.4 S x E1 Matrix with Fiducial Points

the error is small with respect to the isotopic separation. For Iron, the E-dimension 1-AMU separation is 2-4%, implying that the E response error must be small compared with 2%. Similarly, Figure 3.4 showed that the charge separation in the S x E plane is 7% near Iron, implying that the dE/dx response error must be small with respect to 7%. The general steps taken to derive the response functions from the data were:

1. On matrices of S x E (see Figure 4.4), the locations of the most abundant charges are obvious. Smooth curves are sketched through the center of each of these pulse height distributions, following the variation of E and S with particle energy. The set of lines for all these charges is studied to smooth the intervals between the curves, then the channel number of each detector at each of the fiducial points is recorded. Calculations are performed to give the energy deposit (Mev) at each fiducial point.

2. The fiducial data are then plotted to give an outline of the response function. This is sketched in Figure 4.5, where log (ch/Mev) is plotted against log (Mev).

3. Smooth trend-lines are drawn through the response data, which describe the variation with charge of (ch/Mev) at each calibration point. The (ch/Mev) determined along

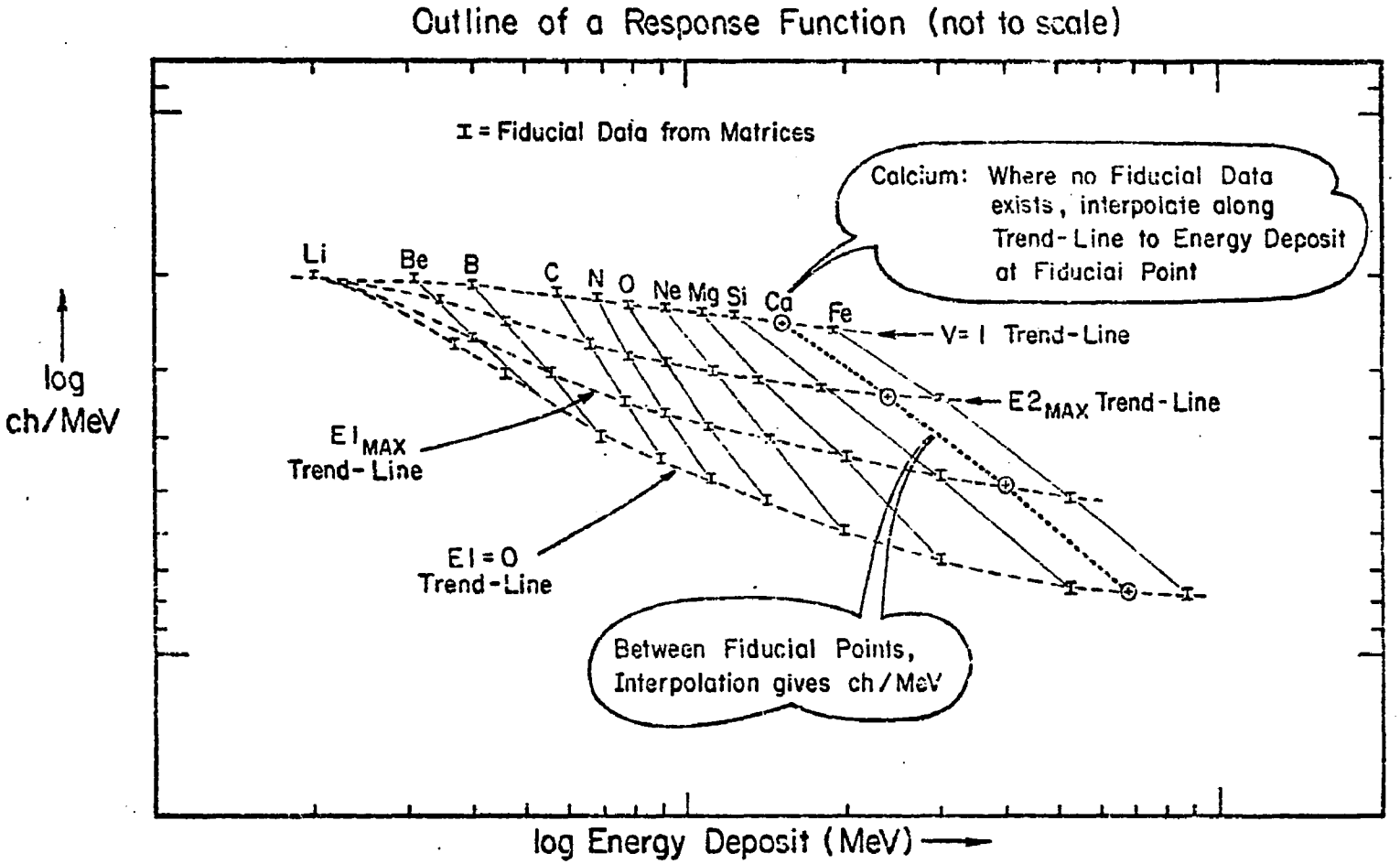

Figure 4.5 Outline of a Response Function

the smoothed trend-line is checked against the matrices for consistency. This step is iterated until the network of trend-lines is smooth and consistent with the data.

4. From energy-loss tabulations, the energy deposit of all other nuclides of interest at each of the calibration points is determined. The response of each detector to a particle of given charge and energy deposit is obtained by finding (ch/Mev) along each of the detector response function's trend-lines, and interpolating between these points to get (ch/Mev) at the precise energy deposit of the particle. Following an ensemble of particles through the instrument, we obtain in this manner tables of the predicted instrumental response to all nuclides and energies of interest.

5. The tables produced in step 4 are used to assign a charge and mass value to each event for several detector combinations. The distributions of charge and mass assignments thus obtained are studied to 'fine tune' the response functions further until the charge and mass distributions are centered on the appropriate values. The demand that the response function trend-lines be smooth is carefully maintained throughout this step.

3.2 C X E CALIBRATION INFORMATION

In parallel with the above steps, the best-fit mass line locations on the CxE matrices of the abundant species Ne-20, Mg-24, Si-28, and Fe-56 are used to augment the fiducial data in forming the response functions of E1 and E2. (The Cerenkov detector itself can be precisely calibrated using the v=1 data, as described below.) The Cerenkov response is used to predict the energy deposit (Mev) in E, and the best-fit mass lines are used to find (ch) in E at the predicted Cerenkov channel. This information is especially important for Iron which stops in E1, because the information on response in this region from other sources is limited.

4.0 INSTRUMENT CALIBRATIONS: DETAILS

Now we turn to a detailed discussion of the calibration of the Cerenkov, dE/dx, and residual kinetic energy detectors.

4.1 CERENKOV CALIBRATION

The response of the Cerenkov detector is the best defined of any in the instrument. There are three components of the output: primary particle Cerenkov light, which is dominant, knock-on electron Cerenkov light, which mainly affects the output near v=1, and residual

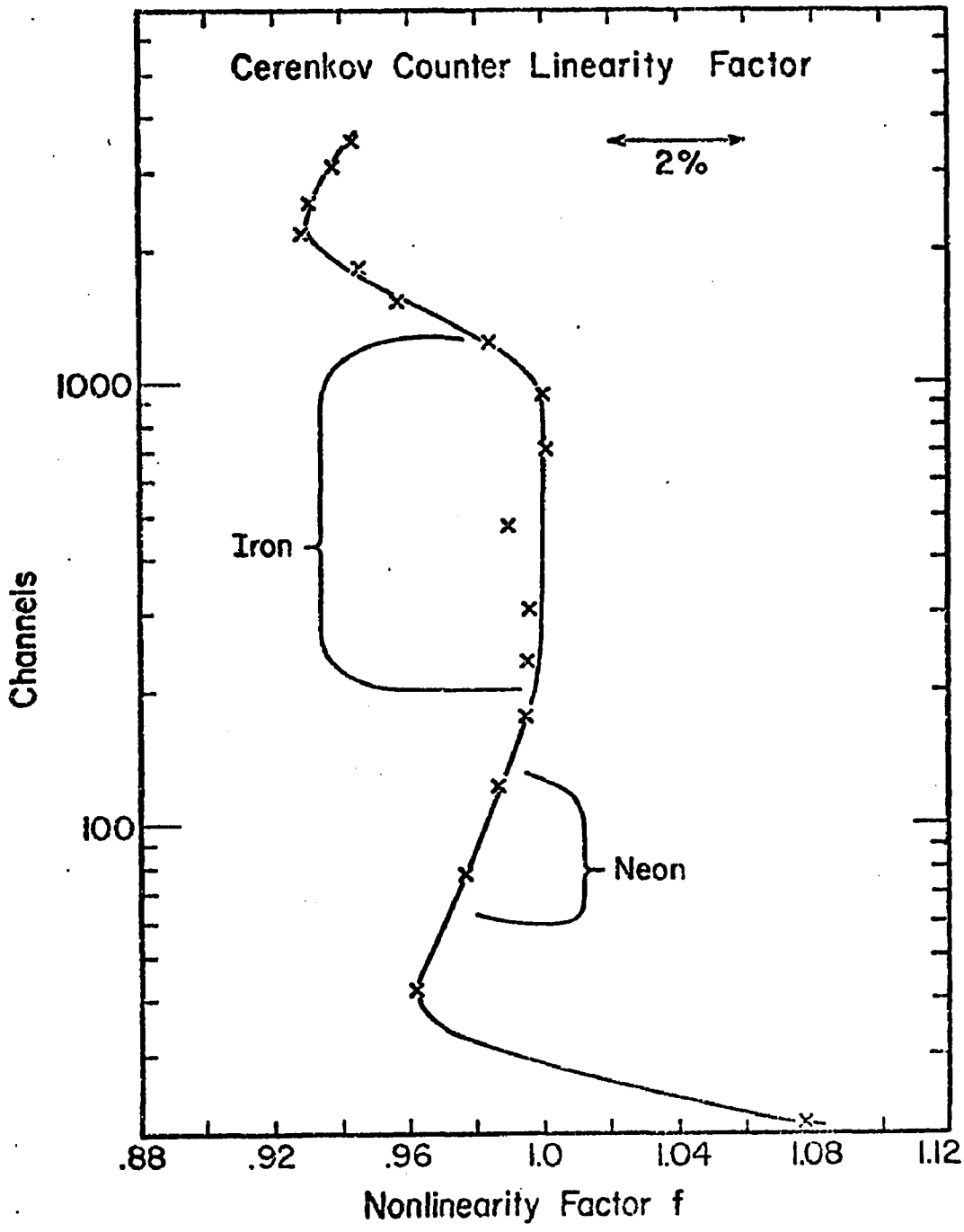

Figure 4.6 Cerenkov Detector Linearity Factor

scintillation.

We use the method of Lezniak (1975) to obtain Cerenkov detector calibration information from the pulse height distributions in C near v=1. His method provides a technique for estimating the theoretical v=1 point from the pulse height distributions of real detectors by carefully taking into account the effect of resolution broadening. We give a brief summary of his estimation technique in Appendix II. The Cerenkov detector gain is fixed by equating the v=1 pulse height channel to the complete expression for the detector output, including the effects of knock-on electrons and residual scintillation. The detector linearity may be studied by comparing the calculated response (nearly Z**2) to that observed at the v=1 point for a variety of charges. Figure 4.6 shows the Cerenkov linearity correction factor, as a function of pulse height channels. In most of the the region useful for C x E1 mass analysis, no deviation from linearity greater that 0.5% is observed*.

Lezniak (1976) provided the results we used on the knock-on electron contribution to our Cerenkov detector output. Figure 2.4 showed these results.

*The deviation from linearity at low channels may be simply explained as an ADC zero offset of 2 channels. The deviation at high channels presumably originates in electronic non-linearity, most probably in the ADC circuitry.

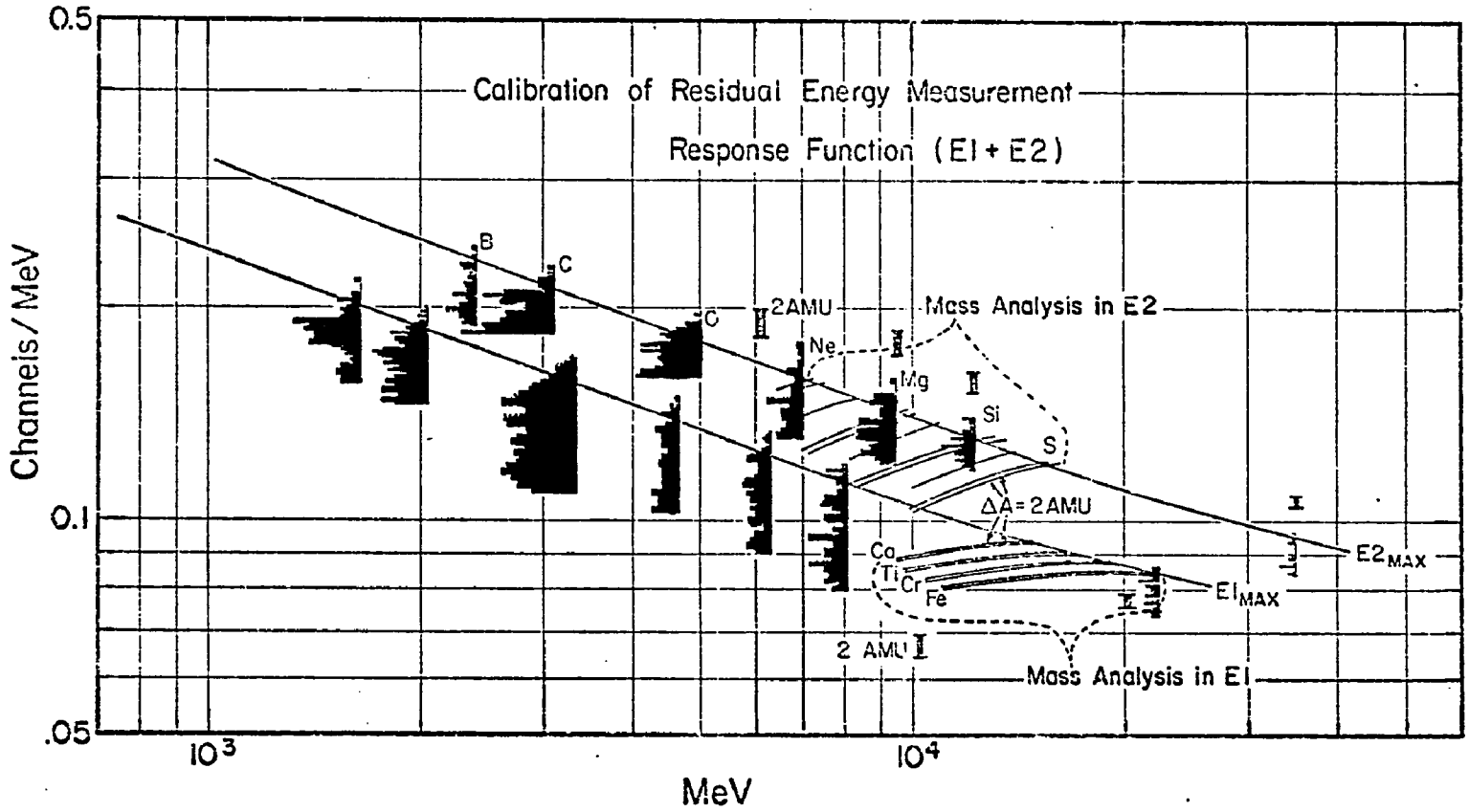

Figure 4.7 Response Functions Derived for E1 and E2

The residual scintillation is about 3% of the v=1 C response. It was described by constructing a residual scintillation response function. Since we do not have residual scintillation data at E2max and E1max for high Z elements, and for all charges at v=1, we have used only two trend-lines, estimating the residual scintillation at E1max for Z=14,16, and 26. Fine tuning of the residual scintillation response function was performed using the Iron residual scintillation line, which is well-defined (see Figure 4.15).

4.2 TOTAL ENERGY RESPONSE FUNCTION

In the construction of the total energy response functions for E1 and E2, we used the combined power of information from the fiducial points, the Cerenkov calibration, and the well-resolved mass lines in the C x E plane.

Figure 4.7 shows the response functions derived for E1 and E2. Of special relevance to this Figure are the following points:

1. The fiducial data are presented as event histograms. The observed (E1+E2) channel number of each event (of selected good-statistics charges) is divided by the calculated Mev at the fiducial point. The number distribution of ch/Mev of all particles in a broad

region around the fiducial point, which forms each histogram in the Figure. The sharp drop in the histograms defines the fiducial points. The two factors limiting the fiducial data quality are statistics and pathlength variations in the flat E counters.

2. E1 and E2 have different response characteristics, as is plain from the Figure. For particles that penetrate to E2, E1 and E2 are treated as a sum to eliminate pathlength errors (of magnitude about 7%) which would be present if E2 were treated separately. These errors arise because E1 is flat. In the sum (E1+E2) the individual pathlength errors cancel. (Refer to Figure 2.6.)

3. The region of the response function in which isotopic analysis is possible is limited, as we have seen in Chapter III, by resolution-separation considerations in the C and E detectors (Figures 3.7, 3.8, and 3.9). Another effect limiting the available region is the sharp hook seen in the predicted response lines in the C X E plane as particles penetrate from E1 to E2 (Figure 3.6). Because E1 is flat, the hook may start at a variety of signal levels in E1, depending on the zenith angle of incidence assumed in the response calculation. These factors limit us to two separate domains of the total E1+E2 response function, which we show on Figure 4.7. The elements Neon through Sulphur may be analyzed

when they stop in E2, and Calcium through Iron particles may be studied when they stop in E1. Outside these domains, either the mass separation is small with respect to the resolution, the particle velocity is below the Cerenkov threshold, or the E1-E2 hook obscures the mass separation. Therefore we have essentially two response functions to study: one for E1+E2, Ne through S, and a second for E1 alone, Ca-Fe.

4. The bars shown on the Figure give the magnitude of response function error necessary to change the mass assignment by 2 AMU.

5. The response lines of each isotope are slightly curved. This is because the mass histograms formed using a linear interpolation between the fiducial points were found to show somewhat inferior resolutions as compared to those which could be obtained by performing the interpolation with a slight degree of curvature. This curvature was incorporated into the response model by allowing one free parameter to fit the deviation from the straight-line fit of all the isotope response lines in each E detector. This procedure optimized the mass resolution. The curvature of the isotope response lines was fitted by a hyperbolic tangent in the form

$$Y = Yo + K \tanh \alpha \left(\frac{X-Xo}{X_1-Xo}\right)$$

where:

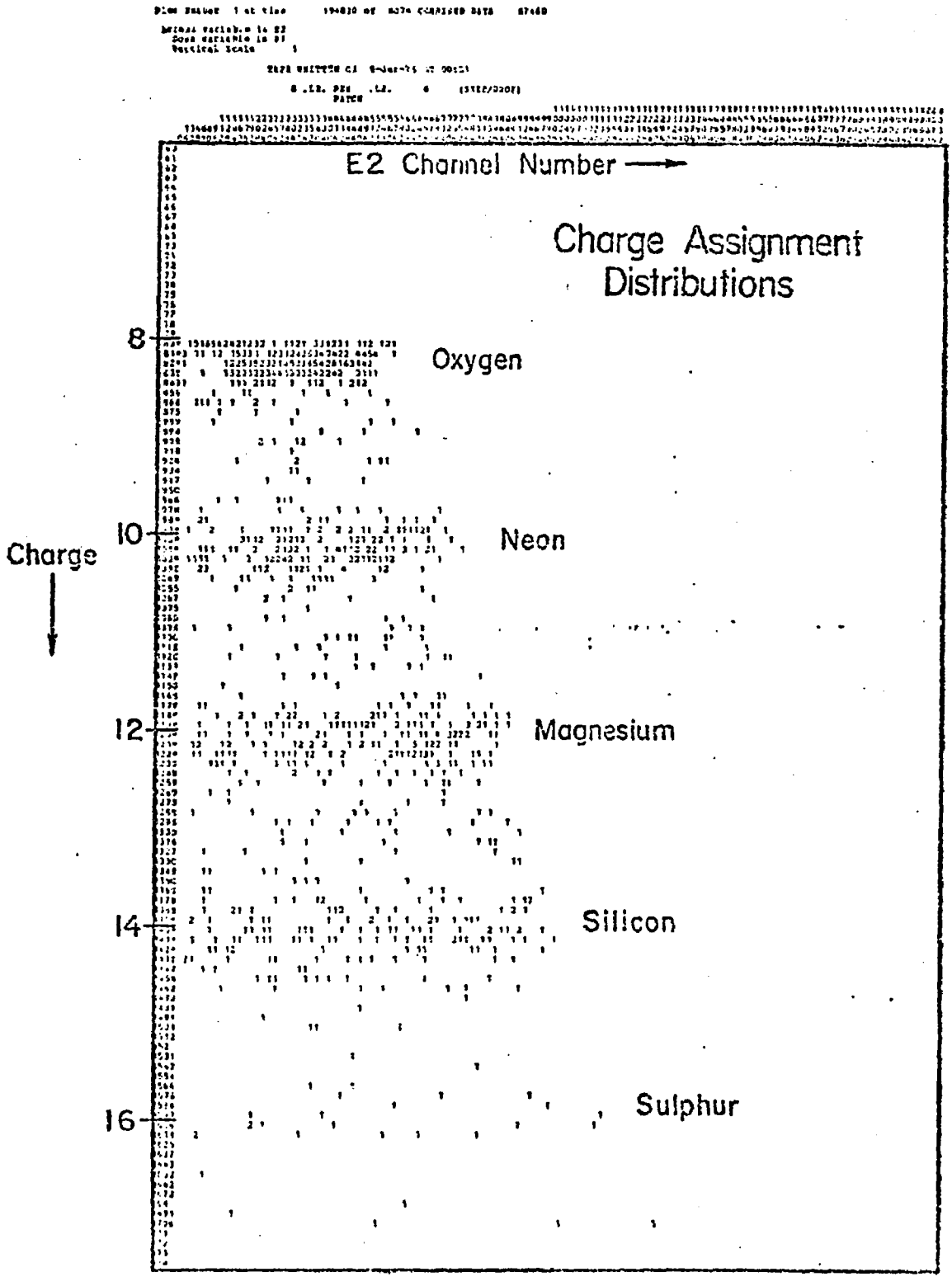

Figure 4.8

Charge Assignment Distribution For Particles Stopping in E2

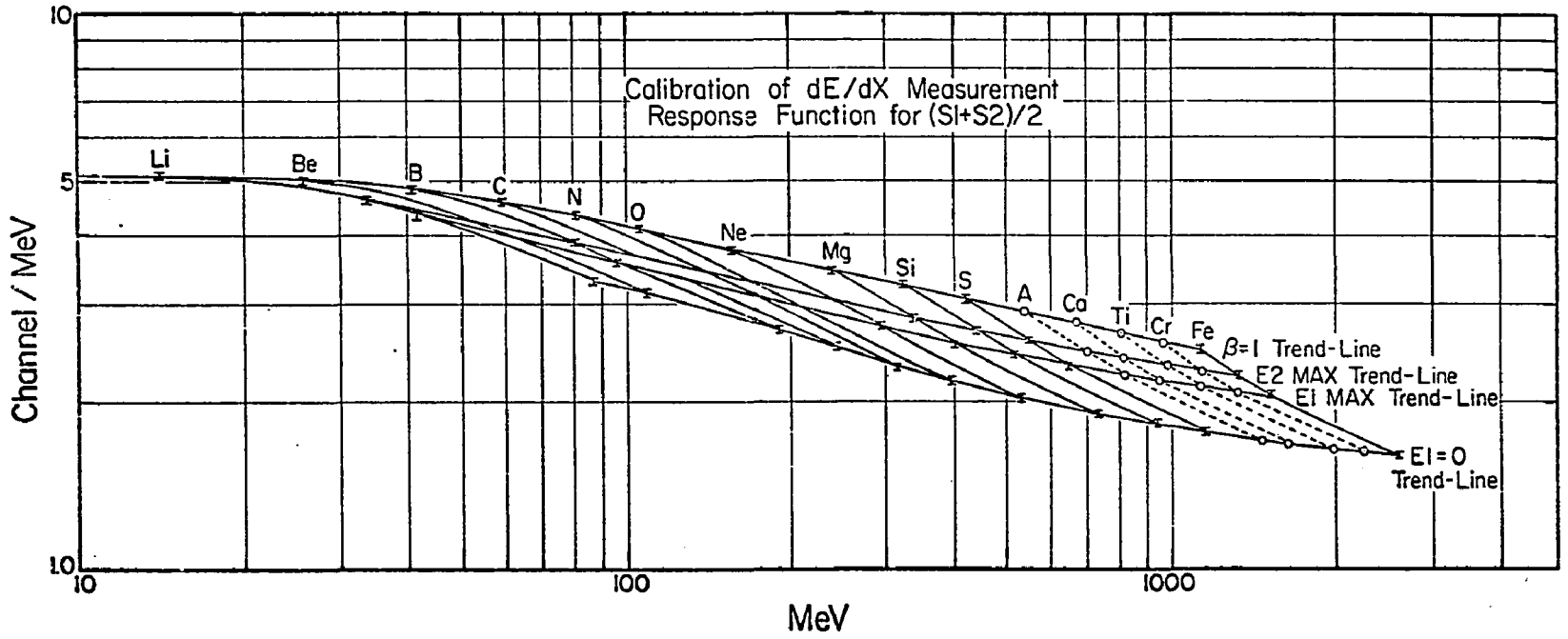

Figure 4.9. Response Function of S

X0 and X1 are the energy deposits at the fiducial points, and Y0 and Y1 are the ch/MeV at X0 and X1 on the trend lines.

The physical significance of this curvature is that the non-linearities of the scintillation material themselves saturate as the energy loss increases.

4.3 CALIBRATION OF THE S MEASUREMENT

Calibration of the S measurement is necessary to ensure that the best charge assignment is given to each particle. We have fiducial data to help us in this task at E1=0, E1max, E2max, and v=1. (Figure 4.4 showed the location (ch) of the calibration points at E1=0 and E1max on the matrix of E1 X S.) Energy loss calculations give the energy deposited (Mev) in S at each of these points. Using the response function derived from the fiducial data as a starting point, the S response function is improved by making charge estimates to the nearest 0.1Z based on the response function and the energy loss calculation. When these estimates are plotted versus E1 or E2, we have charge distributions such as those in Figure 4.8. The centering and slope (if any) of the charge distributions are used to re-estimate the response functions. Figure 4.9 shows the S response function as finally derived using the above procedures.

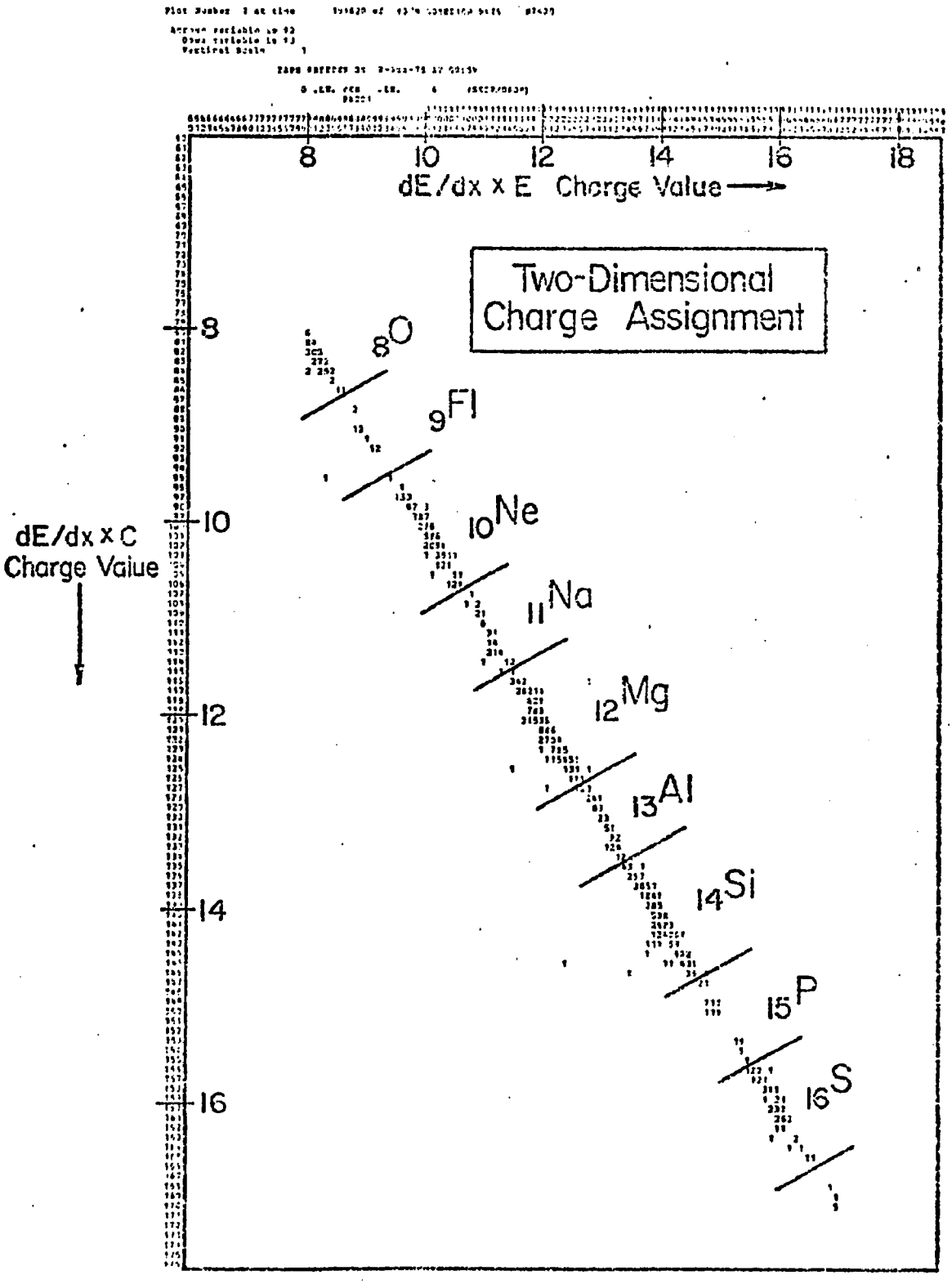

Figure 4.10

Two-Dimensional Charge Assignment: Z=8-16

5.0 CHARGE ASSIGNMENT

The charge of each event is determined by interpolation of the event coordinates using a table of calculated detector responses. This table is formed by calculating the detector output for a series of energies and nuclides spanning the range of interest, as discussed in the previous sections.

Because the mass assignment is not independent of the charge assignment, it is crucial to make the most careful Z-estimate possible. We have estimated the charge of each event in two pairs of detectors: C-S, and E-S. The charge assignment in each pair of detectors is performed by linear interpolation along coordinates orthogonal to the charge lines. We use the average of the E x S and C x S charge estimates to assign a charge value to the nearest 0.1Z for each event. The best estimates of the charge in the C x S and E x S modes are shown plotted against one another in Figures 4.10 and 4.11. (Z=10-16 is on 4.10, while Z=20-26 is shown on 4.11.) On these Figures, even charges were assigned to all events lying in an interval 1.2 Z wide, centered on the even integer value, and odd charges were assigned to events in the remaining 0.8 Z interval. This difference minimizes the effect of charge spill-over from the abundant even elements into the less abundant odd elements.

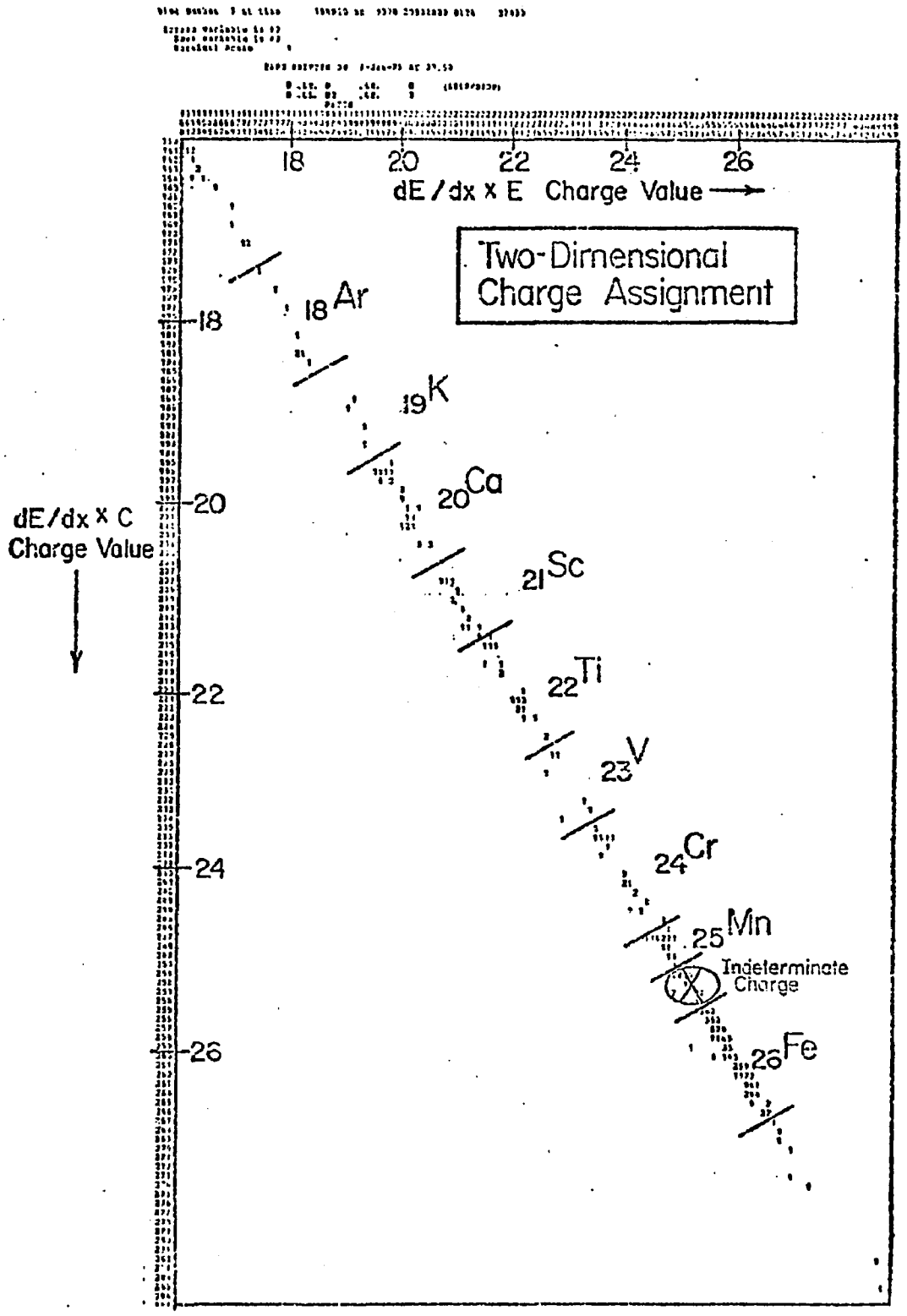

Figure 4.11

Two-Dimensional Charge Assignment: Z=18-26

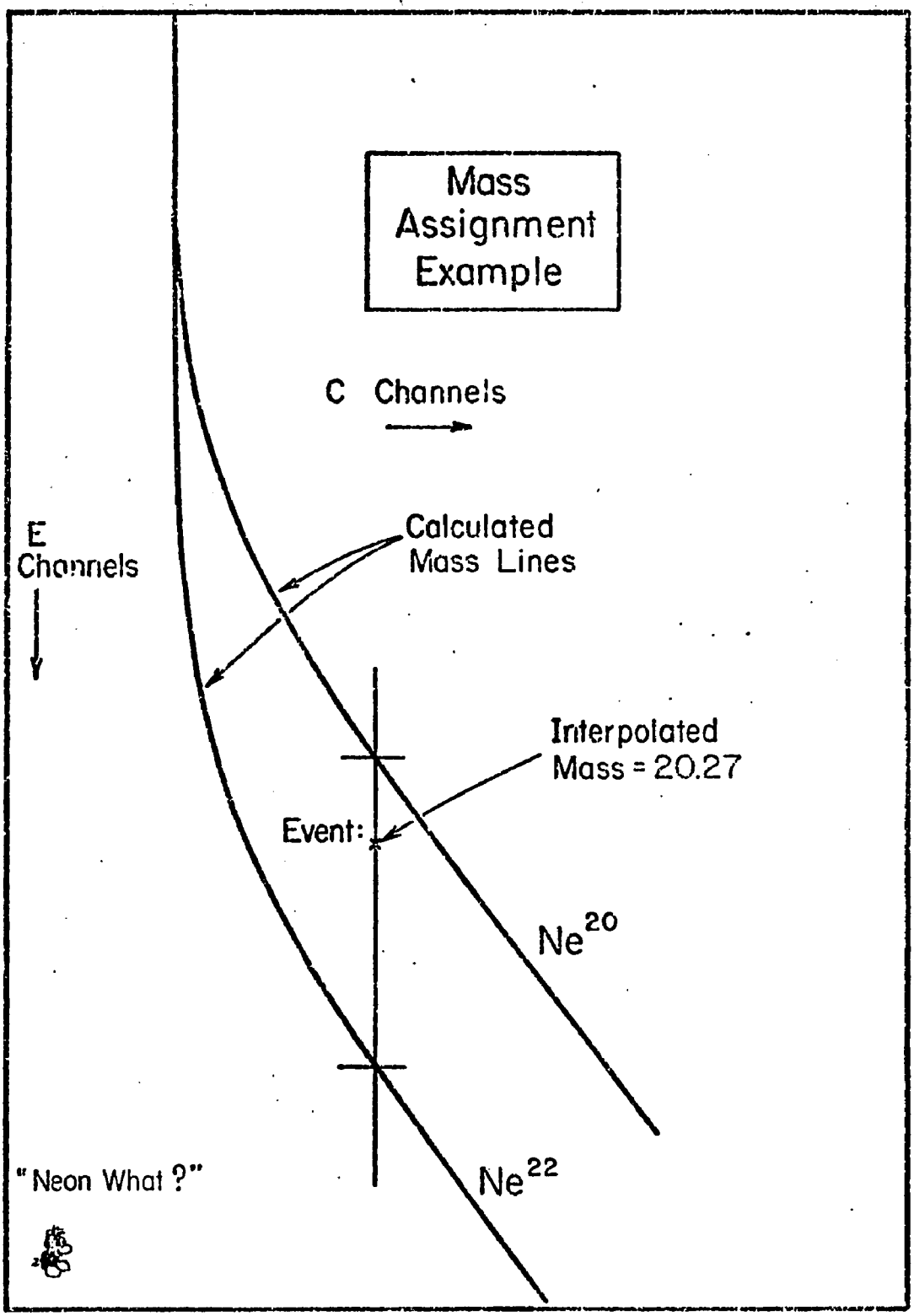

Figure 4.12 Mass Assignment Example

Manganese is treated somewhat differently, because of the large relative abundance of Iron, which introduces severe spill-over problems into the Manganese region. We prefer not to assign a charge in the region of Z=25.1 to Z=25.4, since the true charge may well be either 25 or 26 there.

6.0 MASS ASSIGNMENT

The mass assignment for a particular event is made by a linear interpolation in the C x E plane between the predicted responses of isotopes of the assigned charge separated by 2 AMU (see Figure 4.12).

As we have mentioned, resolution-separation diagrams for the Cerenkov counter show that mass resolution is optimal in a rather narrow band of energies near the Cerenkov threshold. We are therefore obliged to balance the benefit of increased statistics which comes from broadening our energy band against the resolution loss which is simultaneously incurred. We also must limit the range of energies considered to avoid the 'hook' region. For particles stopping in E1, best results are obtained if values of E1 are allowed such that all the important isotopes of each charge are above the Cerenkov threshold, and such that the hook region is not entered. Calcium through Iron are analyzed in E1. In E2, the mass separation of Ca through Fe rapidly falls below the mass resolution

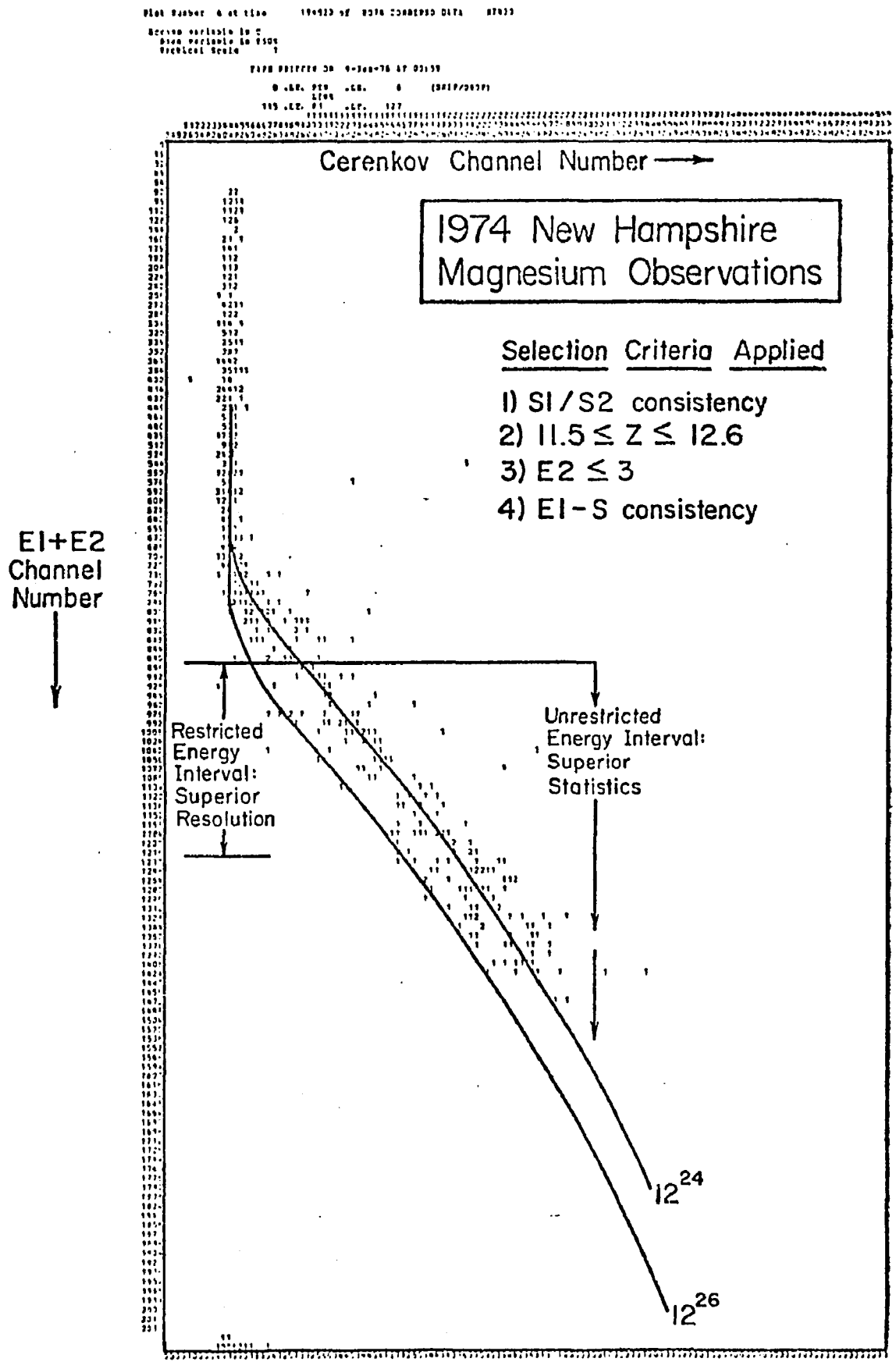

Figure 4.13 C x E Matrix: Magnesium

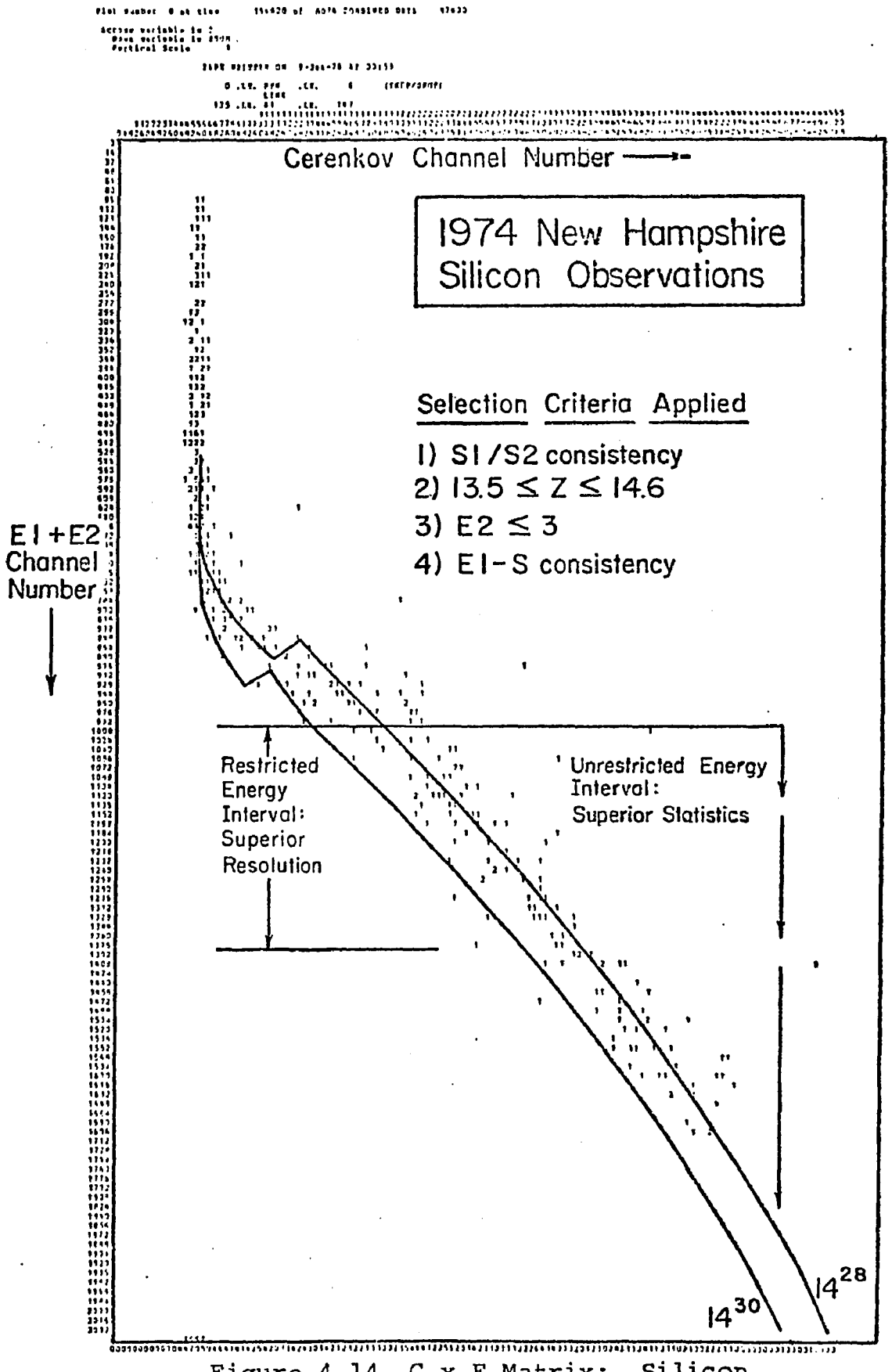

Figure 4.14 C x E Matrix: Silicon

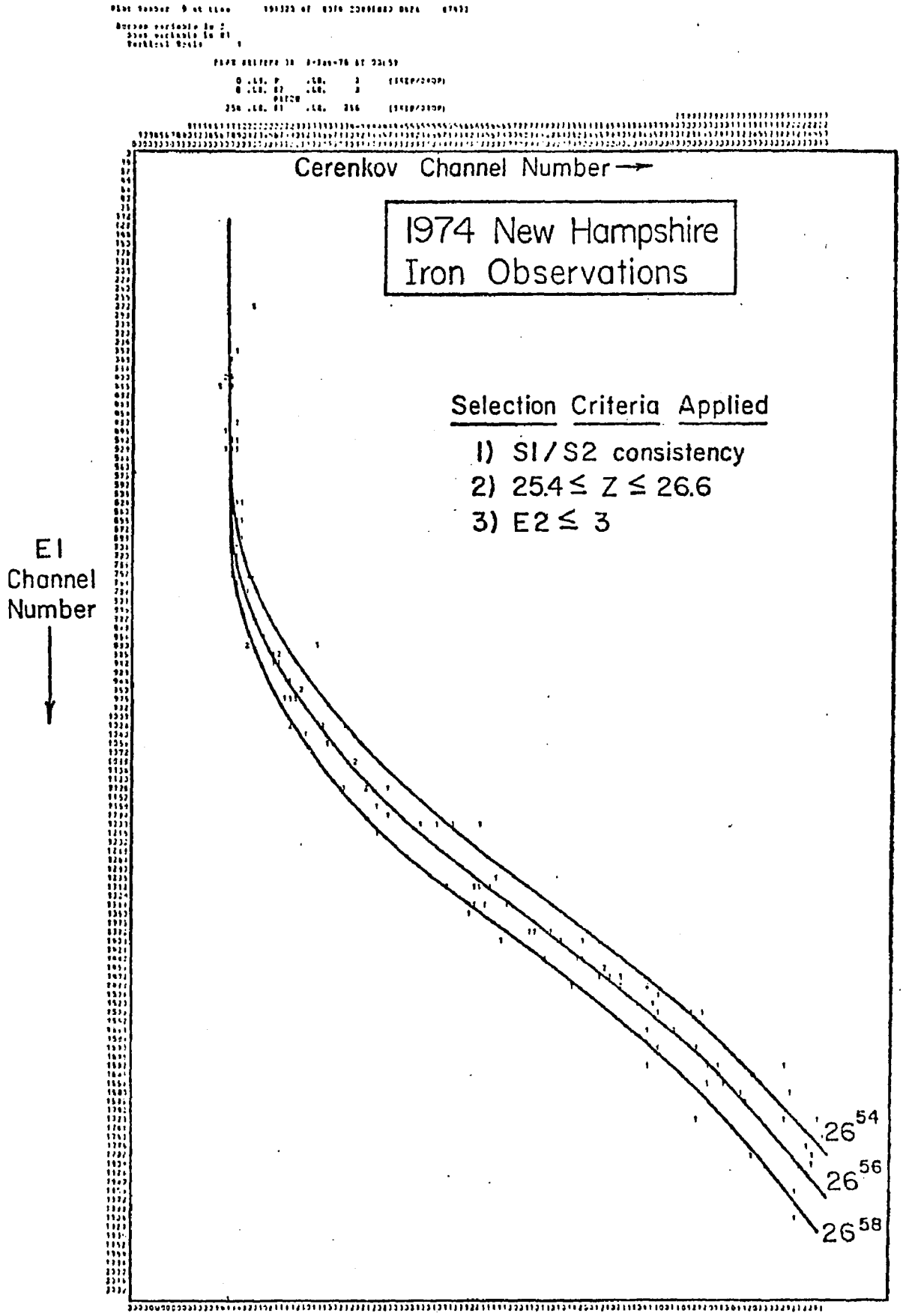

Figure 4.15 C x E Matrix: Iron

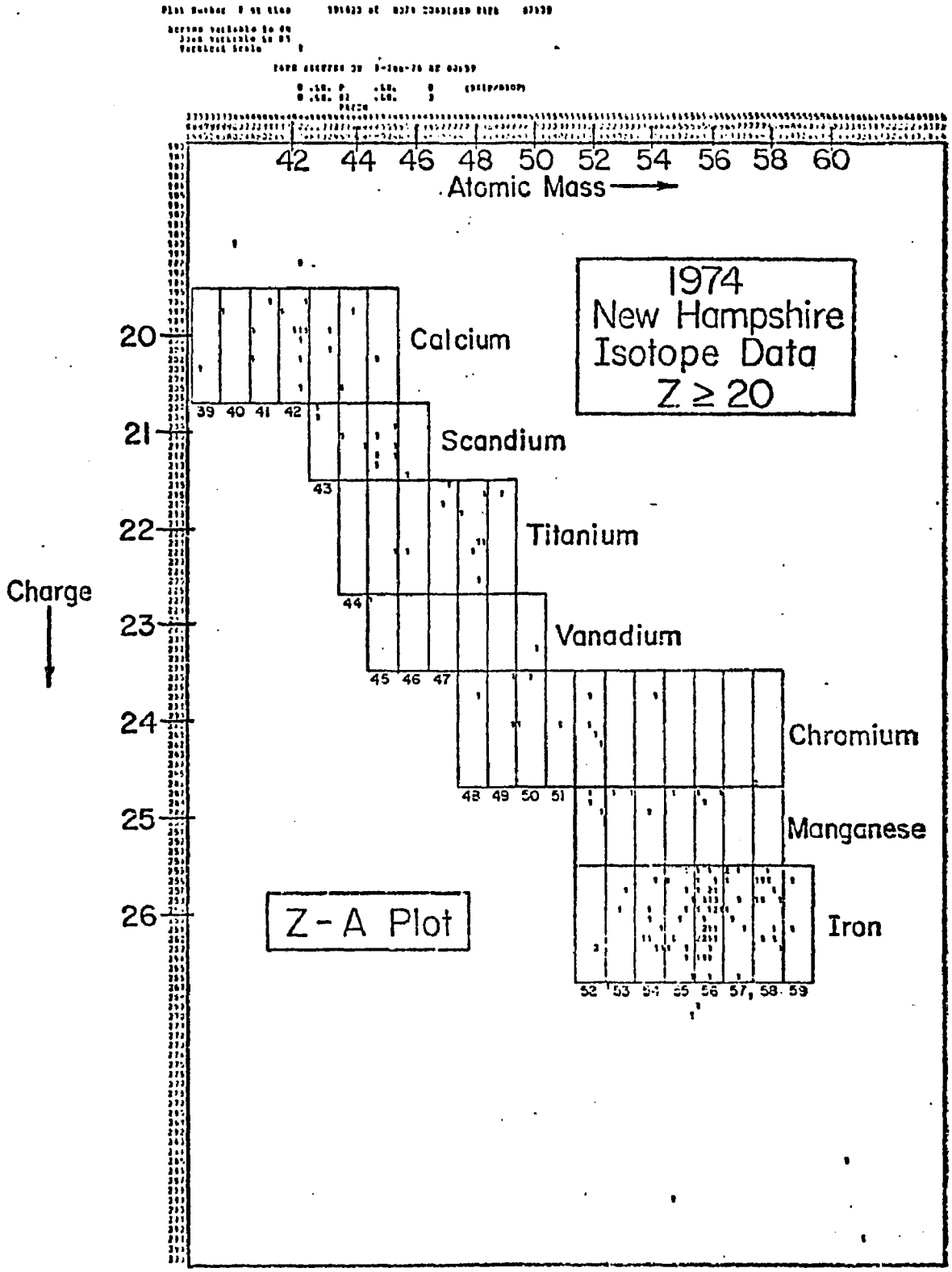

Figure 4.16

Z-A Plot

Calcium - Iron

(Figure 3.6), so they are not analyzed.

Neon through Sulphur nuclei exceed the Cerenkov threshold only when they stop in E2, and so are only suitable for mass analysis there. For this group of charges, the resolution-statistics trade-off is also very important.

We show in Figures 4.13, 4.14, and 4.15 the C x E matrices for Magnesium, Silicon, and Iron. The mass plots which we will show below maintain an event-by-event correspondence with these matrices and others like them.

6.1 THE Z-A PLOT

The most effective way we have found for presenting the data showing both the charge and mass resolutions simultaneously is in the form of a "Z-A plot", which is effectively a chart of the nuclides. On this plot each event is represented by a point at the charge and mass assigned to it, with the charge and mass shown to the nearest 0.1Z and 0.2 AMU, respectively, to display the final resolution of the experiment. The Z-A plot for all particles stopping in E1 and meeting the E1 selection criteria discussed above is seen in Figure 4.16, while that for particles stopping in E2 (and meeting the criteria appropriate to this region) is shown in Figure 4.17. Cells are drawn on the plot which correspond to the location of

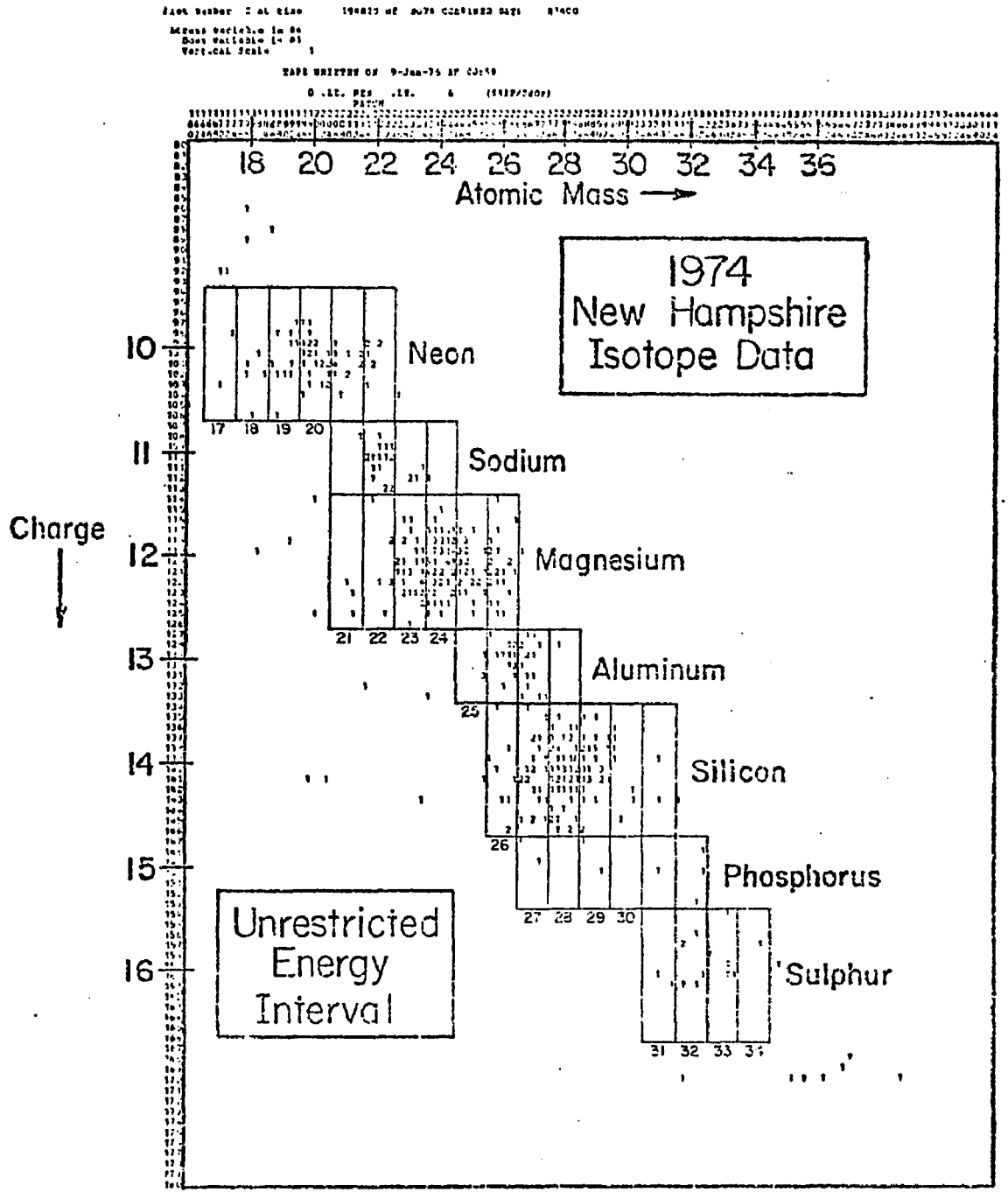

Figure 4.17 Z-A Plot: Neon-Sulphur (Unrestricted)

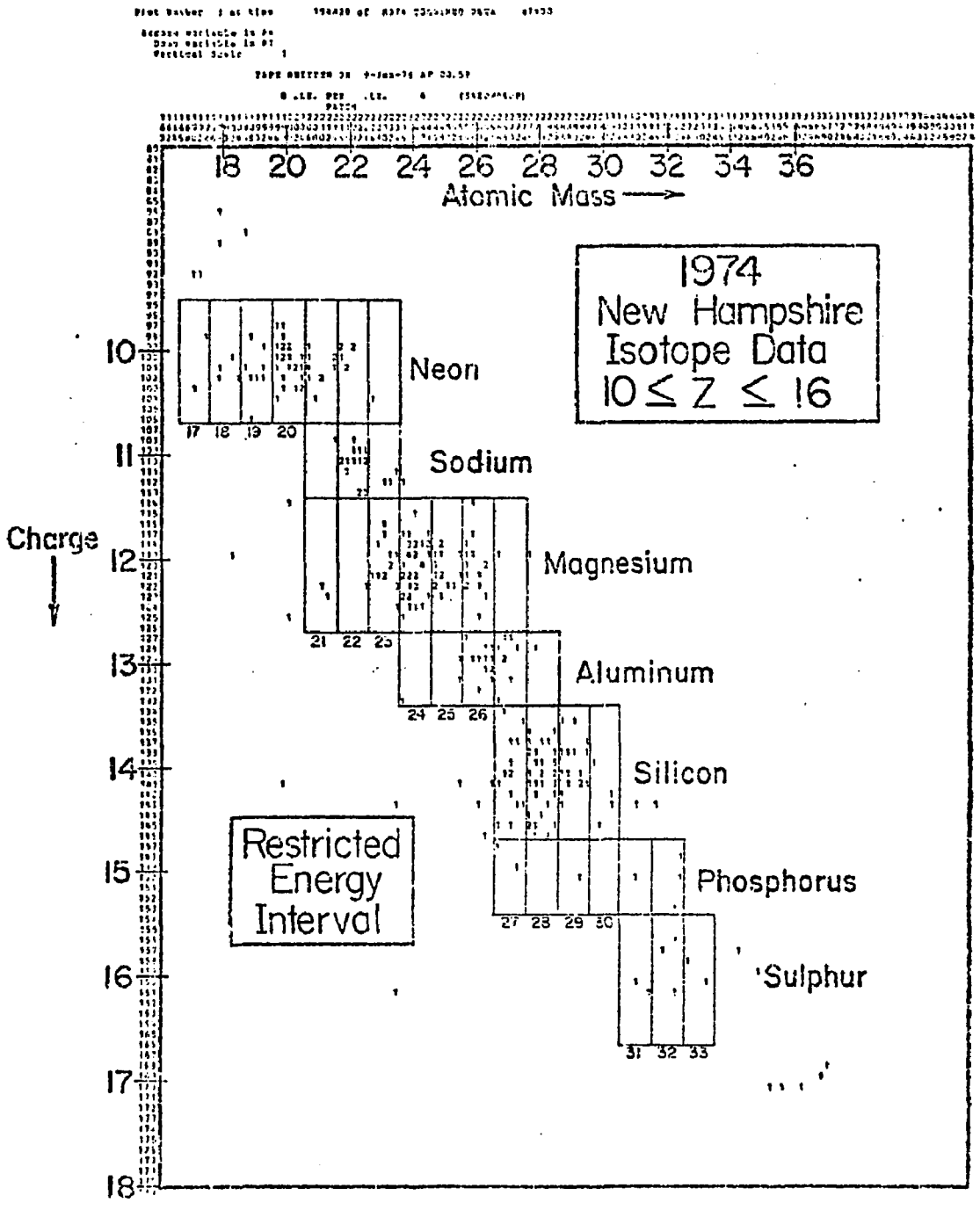

Figure 4.18 Z-A Plot: Neon-Sulphur (Restricted)

each observed isotope in the chart of the nuclides (with allowance made for the slightly larger charge interval assigned to the even charges). The clear resolution of isotopes of Fe, Cr, Sc, and Ca is evident in Figure 4.16. Examining the Z-A plot of particles stopping in E2, we see the first clear resolution of the isotopes Ne-22 and Mg-26.

It is interesting to examine a Z-A plot of particles stopping in E2 with energy intervals tightly restricted to the region of optimal mass resolution. Figure 4.18 shows this Z-A plot. We judge that the two E2 Z-A plots are about equivalent, the higher statistical accuracy in the "unrestricted" case (figure 4.17) balancing the superior resolution of the "restricted" plot.

6.2 SYSTEMATIC ERRORS OF MASS ASSIGNMENT

The E1 response function, which governs mass assignment in the Z=(20-28) range, was obtained by making two crucial assumptions, namely the mass of the dominant Iron isotope, and that of Scandium. These two assumptions are essential to anchor the mass scale for particles which stop in E1. There is only one stable isotope of Scandium, Sc-45, but there are 4 stable isotopes of Iron (54,56,57,58), and a priori, it is not certain which mass value should be assigned to the central mass group. We do know that Fe-56 is the most abundant of the terrestrial Iron isotopes (92%), and that it is very difficult to conceive of an

astrophysical situation which would produce dominant Fe-54 or Fe-57 (Hainebach and Schramm, 1975). However, we do not rely on these facts to set our mass scale.

The strongest evidence bearing on the Iron mass assignment is in the Iron isotopic mass distribution which comes from Figure 4.16. The distribution of Iron mass values shows a central dominant isotope flanked by two less abundant groups about 2 AMU on either side. Assuming the dominant nuclide to be stable, the possible alternative hypotheses to Fe-56 dominance are:

1. Fe-58 dominance, Fe-60 is present in appreciable quantities, Fe-56=0.25 x Fe-58; Fe-54=0.

2. Fe-54 dominance, Fe-56=.25 x Fe-54, Fe-52=.25 x Fe-54. The lifetime of Fe-52 is 8.2 hours.

3. Fe-57 dominance, Fe-59(45days)=.25 x Fe-57, Fe55(2.6years)=.25 x Fe-57.

Hypotheses 2 and 3 may be examined as follows: The only source of short-lived isotopes is atmospheric and instrumental interactions. The instrument + atmosphere total thickness to the top of E1 is 9 gm-cm. With cross sections from Silverberg and Tsao (1976), Perron (1975), and Lindstrom (1976), we estimated the probabilities of stable primaries fragmenting above E1 in sufficient quantities to

PROBABILITIES OF ALTERNATIVES TO Fe-56 DOMINANCE

Hypothesis 2: Fe-54 Dominant

Assumed Z,A	Cross-Section to Fe-52	Mean Number of Fe-52 Predicted	Observed Number
26,56	1 mb	.037	14±3.9
26,55			≤4
26,54	10 mb	.37	53±7.4
26,53			≤4
26,52		Net: .41	8.5±3.6

Hypothesis 3: Fe-57 Dominant

Assumed Z,A	Cross-Section to Fe-55	Mean Number of Fe-55 Produced
26,59		-
26,58		-
26,57	50 mb	1.8
26,56		-
26,55	Net:	1.8

Using Student's t-statistic:

The probability of observing 8.5 Fe-52 when 0.41 are expected is:

$$P\{t > 2.3 | \nu=6\} = 3.2\%.$$

The probability of observing 8.5 Fe-55 when 1.8 are expected is:

$$P\{t > 1.9 | \nu=6\} = 4.2\%.$$

Table 4.2

produce the numbers of unstable secondaries which are demanded by the observations under each of these hypotheses.

Table 4.2 shows these probabilities. Those for hypothesis 2 (Fe-54 dominance) are seen to be small. Under hypothesis 3, even if we do produce sufficient Fe-55, there is no source for the required Fe-59, therefore this hypothesis is untenable. Hypothesis 1 can be ruled out by the observation that appreciable abundances of Ni-60 should result from the beta-decay of Fe-60. Also, nucleosynthesis theory has not suggested any circumstances under which Fe-60 could be expected to be present at the source, and there are no fragmentation progenitors in sufficient abundances in the cosmic rays.

Further evidence supporting the Fe-56 choice comes from the alignment of even Z species between Scandium and Iron on even A mass values. This alignment cannot be preserved under any other choice, with the restriction that the response function trend-lines vary smoothly.

Therefore we find ourselves with only one viable option on the Iron composition; an option which yields an excellent categorization of nearby isotopes and which is in agreement with the predictions of current theories of nucleogenesis. It is impossible to quantify the systematic error in mass assignment introduced through the choice of dominant Iron isotope, therefore we forego further efforts in that direction. Noting that the efforts to fit the

response function to the data ceased when all the alignment errors fell below about 0.15 AMU, we take this figure for the possible systematic error in mass assignment.

Systematic errors in the mass assignment for Neon through Sulphur, arising from slight imperfections in the response function of (E1+E2) are also estimated to be 0.15 AMU.

CHAPTER V

RESULTS

1.0 MASS HISTOGRAMS AT THE INSTRUMENT

The Z-A plots, Figures 4.16, 4.17, and 4.18, have shown all the available data covering the charge ranges Z=10-16 (particles analyzed in the E2 counter) and Z=20-26 (particles analyzed in the E1 counter). The purposes of this chapter are to extract from these plots the information that is statistically and physically significant, and to perform the corrections necessary to derive fluxes of each species outside the atmosphere.

We will use the following criteria to characterize the significant results:

1. The possibility of contamination from adjacent charges should not be large. This criterion eliminates from consideration Manganese and Phosphorus.

2. The number of observed counts of any single isotope must be two or more if we are to quote an abundance value for that isotope. Vanadium, by this criterion, is not observed at a significant level in this experiment.

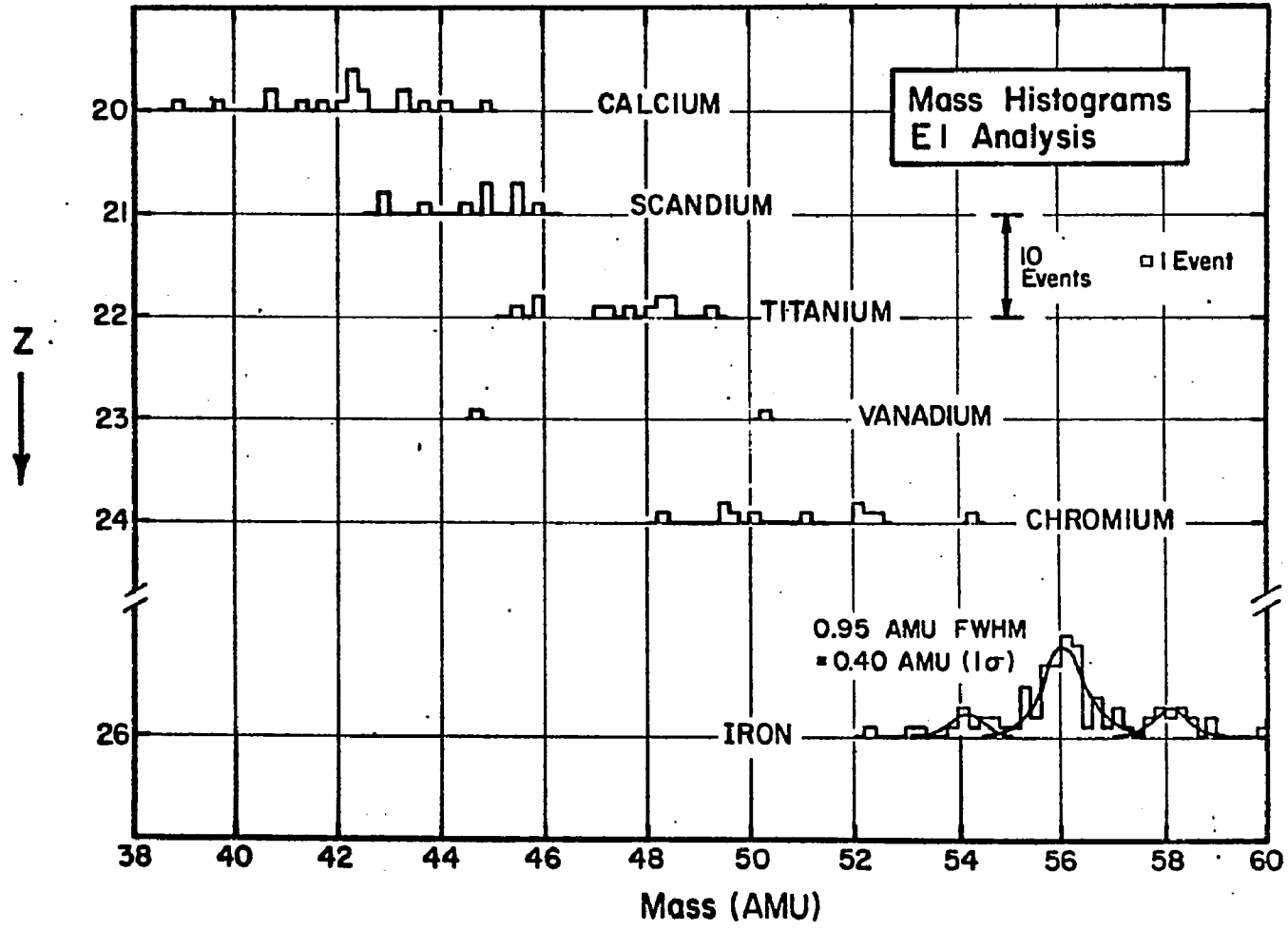

Figure 5.1. Mass Histograms: Z = 20-26

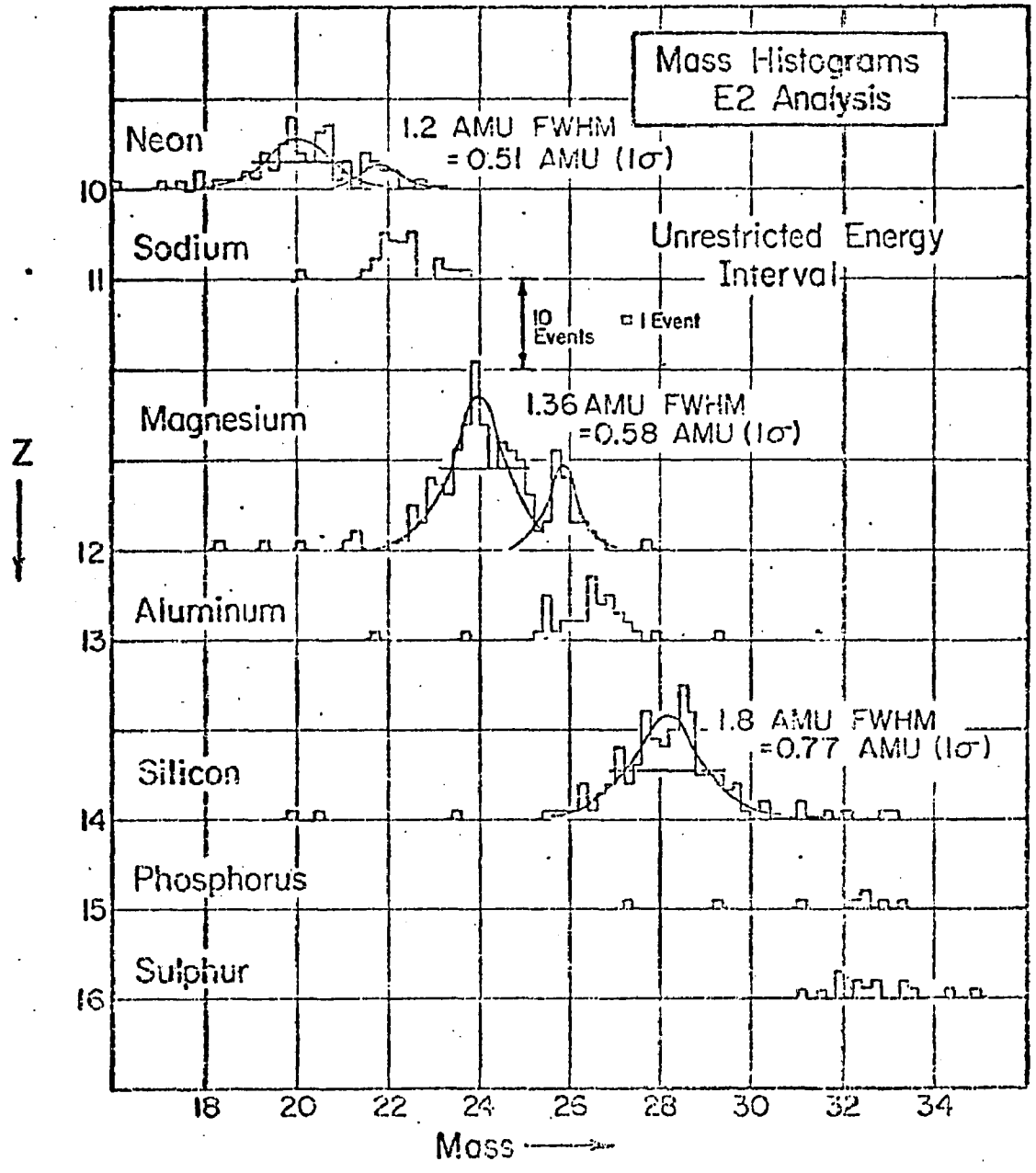

Figure 5.2 Mass Histograms: Z=10-16 (Unrestricted)

Note added in Proof:

Subsequent to the defense of this thesis, the treatment of the isotopes of Ne-Si was revised, by adjusting the E2 response function (Figure 4.7) to give a mean mass of Sodium closer to that of its only stable isotope, Na^{23}. The histograms which resulted from this revision are shown on this figure. All the subsequent tables and discussions have been modified to reflect this improvement.

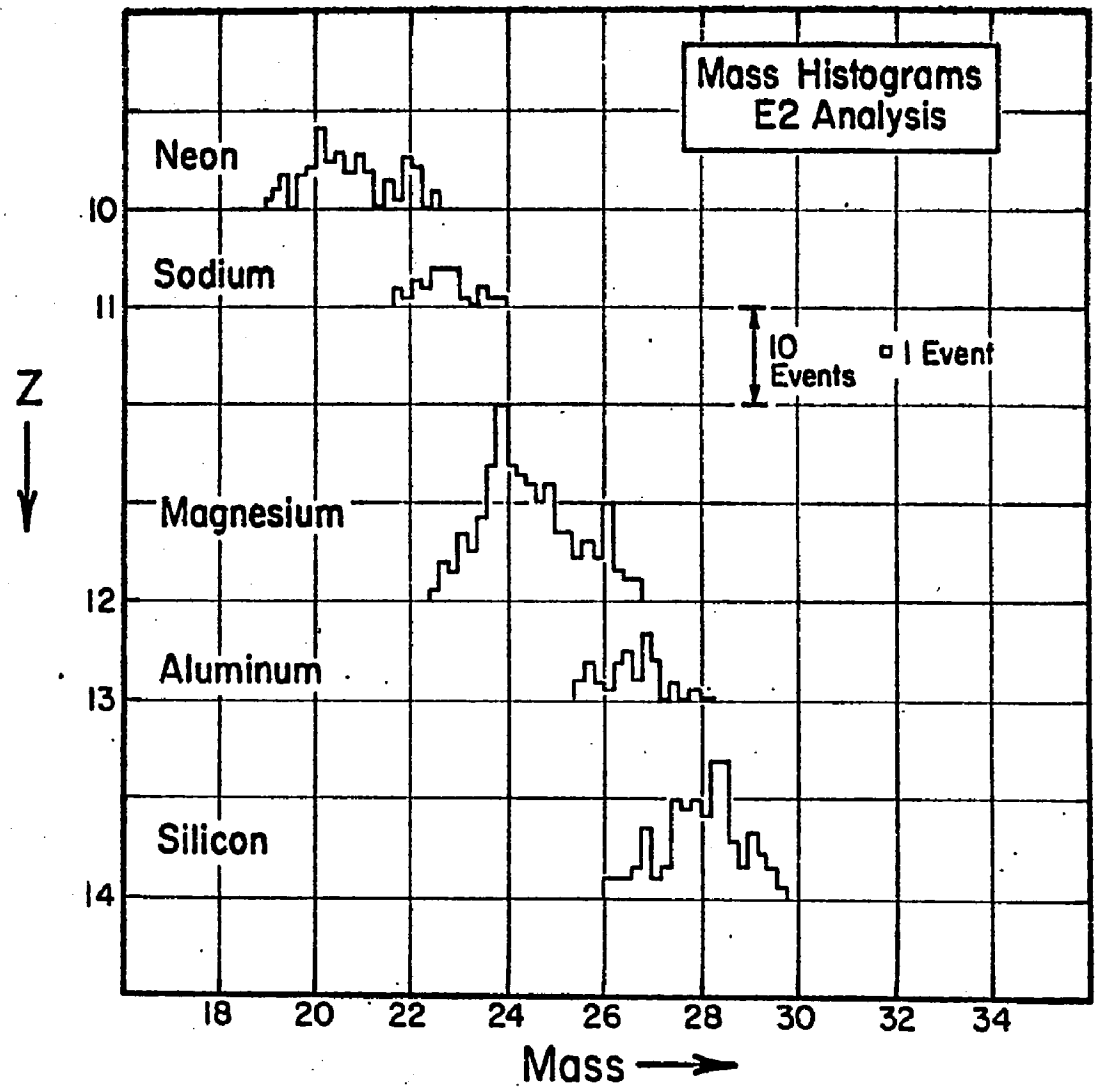
Mass Histograms
E2 Analysis
Neon
Sodium
Magnesium
Aluminum
Silicon
10
Events
1 Event
Z
10
11
12
13
14
18
20
22
24
26
28
30
32
34
Mass

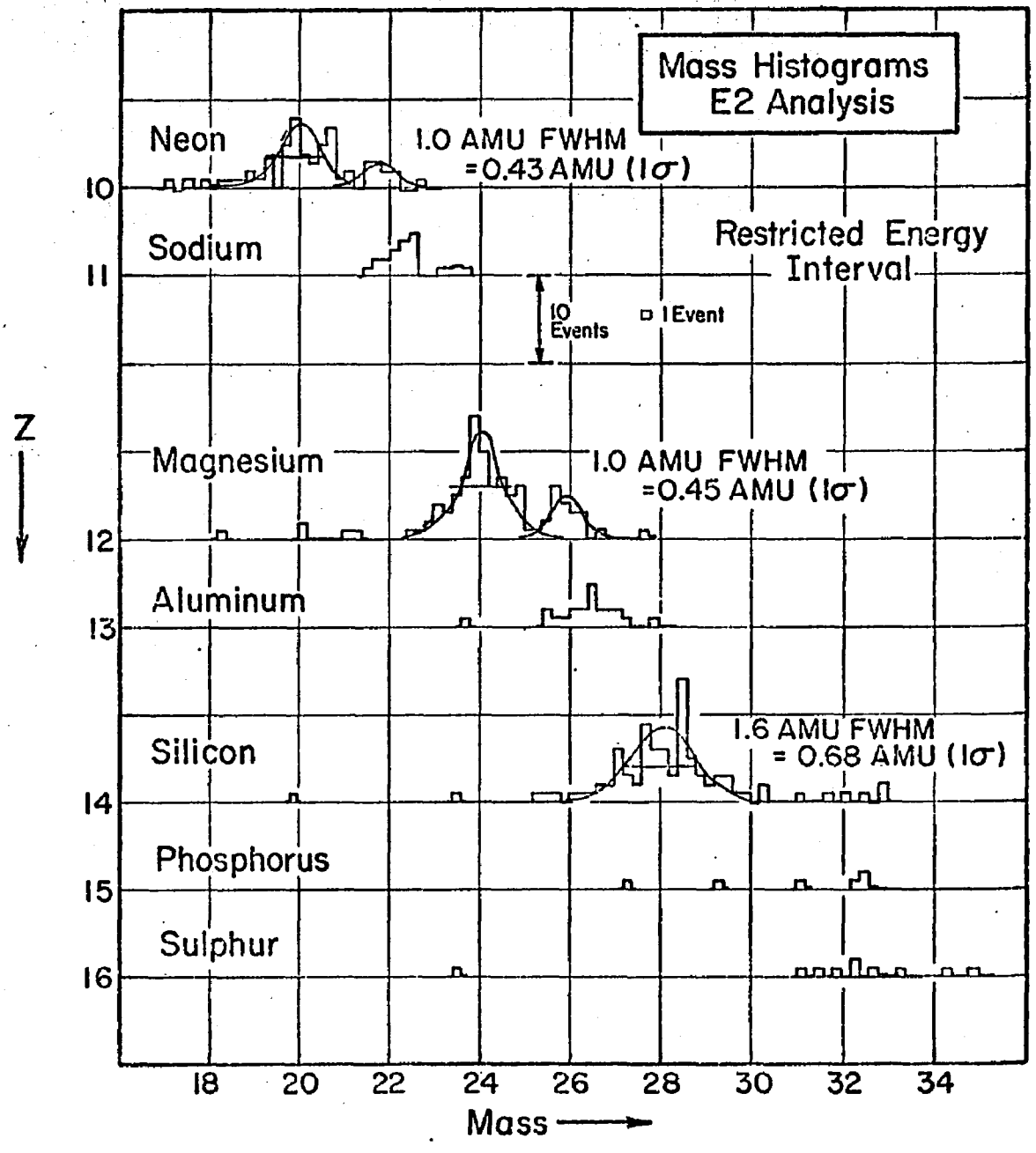

Figure 5.3 Mass Histograms: Z=10-16 (Restricted)

1974 NEW HAMPSHIRE COSMIC-RAY ISOTOPE MEASUREMENTS

Nuclide	Energy (Mev)	Energy Interval	Observed # Events	Neutron Stripping Correction	After Stripping Correction	Error[1]	Corrected For Instrumental Fragmentation	Corrected For Atmospheric Fragmentation	Events/ MeV	Spectral Correction To 600MeV/n	% Of Element	Abundance Relative Fe-56=100
$_{26}Fe^{58}$	582	127	14	-	14	±3.9	54.4	68.7	.541	.519±.14	20.4±5.0	27.8±8.1
$_{26}Fe^{56}$	597	133	53	-	53	±7.4	198	247	1.864	1.864±.260	73.6±5.8	100±14
$_{26}Fe^{54}$	613	139	8	3.6	4.9	±3.3	17.6	20.6	.148	.151±.107	6.0±4.0	8.1±5.5
$_{24}Cr^{52}$	573	112	4	-	4	±2	13.8	12.8	.114	.109±.055	51±18	5.9±2.9
$_{24}Cr^{50}$	589	116	4	.3	3.7	±2	11.1	12.5	.107	.105±.057	49±18	5.6±3.1
$_{22}Ti^{48}$	539	93	6	-	6	±2.4	19.5	22.7	.244	.228±.091	74±12	12.2±4.9
$_{22}Ti^{47}$	547	95	2	.7	1.3	±1.4	3.8	4.4	.047	.044±.047	14±14	2.4±2.5
$_{22}Ti^{46}$	555	97	2	.8	1.2	±1.4	3.3	3.7	.039	.037±.043	12±13	2.0±2.3
$_{21}Sc^{45}$	531	89	7	-	7	±3.2	18.4	20.1	.225	.208±.095	100	11.2±5.1
$_{21}Sc^{43}$	548	93	2[2]	.4	1.6	±1.4	-	-				
$_{20}Ca^{44}$	511	86	2	-	2	±1.4	5.5	6.1	.072	.065±.046	14±9.1	3.5±2.4
$_{20}Ca^{43}$	520	89	2	-	2	±1.4	5.6	6.4	.072	.066±.046	14±9.1	3.5±2.4
$_{20}Ca^{42}$	530	92	8	-	8	±2.8	22.0	25.9	.282	.262±.092	56±13.2	14.1±5.0
$_{20}Ca^{41}$	539	95	3	.6	2.4	±1.7	6.4	7.5	.079	.074±.052	16±10	4.0±2.8
$_{20}Ca^{40}$	548	98	≤4[3]	.2	≤3.8		≤8.5	≤10	≤.10	≤.09	≤17	≤5

NOTES:

(1) Error includes statistical error and systematic error due to isotope distribution overlap.
(2) The two "SC^{43}" events are probably due to spill-over from Ca, as may be seen from the Z-A plot.
(3) Assuming a maximum of 2±2 Ca^{40} events.

Table 5.1. Results (1/2)

1974 NEW HAMPSHIRE COSMIC-RAY ISOTOPE MEASUREMENTS

Nuclide	Energy (MeV)	Energy Interval	Observed # Events*	Neutron Stripping Correction	After Stripping Correction	Error	Corrected For Instrumental Fragmentation	Corrected For Atmospheric Fragmentation	Events/ MeV	Spectral Correction To 600MeV/n	% Of Element	Relative Abundance Fe-56=100
$_{16}S^{34}$	584	112	1	-	1	±1				<.07	<12	<4
$_{16}S^{33}$	597	114	4	-	4	±2.2	15	17.8	.156	.156±.086	30±13	8.4±4.6
$_{16}S^{32}$	610	115	10	-	10	±3.3	36	42.3	.368	.368±.121	70±13	19.7±6.6
$_{14}Si^{30}$	528	112	0	-	0	±5					<5	
$_{14}Si^{29}$	541	114	19	-	19	±10	64.5	75.8	.66	.60 ±.32	21±9.6	32±18
$_{14}Si^{28}$	554	115	70	-	70	±14	228	267	2.32	2.21 ±.44	79±9.6	119±37
$_{14}Si^{27}$	567	117	15	8	7	±9.0					<15	<27
$_{13}Al^{27}$	514	108	27	-	27	±7.7	88.3	100	1.08	1.00 ±.29	93±14	54±17
$_{13}Al^{26}$	527	110	7	4	3	±6.0					<20	<18
$_{12}Mg^{26}$	476	95	26	-	26	±6	90.05	105.6	1.11	.95±.22	19±4	51±13
$_{12}Mg^{25}$	489	97	36	5	31	±8	99.3	115.4	1.19	1.05±.27	21±5	56±17
$_{12}Mg^{24}$	502	99	97	7	90	±10	273	317	3.21	2.97±.33	60±5	1.59±.33
$_{12}Mg^{23}$	515	101	9	11	0	±6					< 4	<10
$_{11}Na^{23}$	476	65	15	-	15	±5	50	57	.89	.76±.25	74±18	41±15
$_{11}Na^{22}$	490	65	6	-	6	±5	17	19	.30	.27±.23	26±18	14±12
$_{10}Ne^{22}$	442	43	9	-	9	±8.2	33.5	38.6	.90	.75±.68	20±14	40±39
$_{10}Ne^{21}$	455	41.5	10	1.7	8.3	±6.4	26.9	30.9	.74	.63±.49	16±11	34±28
$_{10}Ne^{20}$	484	40	33	-	33	±7.7	98.6	113.0	2.83	2.43±.57	64±14	130±50

* In estimating the # events from the Ne-Si histograms, the mass scale was shifted within ± .15 AMU of that defined by the response functions, to find the minimum χ^2 fit. The "unrestricted" dataset is used.

Table 5.1. Results (2/2)

Mass histograms, obtained directly from the Z-A plots, are shown in Figures 5.1, 5.2, and 5.3. Figure 5.1 shows the Z=20-26 range. Z=10-16 is presented in Figures 5.2 and 5.3, first with the unrestricted energy interval discussed in Chapter IV, and then with the restricted energy interval. From these histograms, we estimate the number of counts in each mass interval, showing the estimates in Table 5.1, column 4. These estimates are based on fitted Gaussian distributions, where statistics warrant, or in the case of few events of any charge, simple counting of the events in each isotope cell of the Z-A plot. In the next two sections, we will be concerned with the correction of these estimates for the effects of instrumental and atmospheric interactions. The corrected values are presented in section 4. The chapter concludes with an evaluation of the instrument's performance.

2.0 NUCLEAR INTERACTION CORRECTIONS

To make nuclear interaction corrections, we require the partial cross-sections for any nucleus k(Z,A) of kinetic energy E Mev/n to fragment to j(Z',A') when it collides with an atom of the medium (Zm,Am). We also require the total cross-sections, which give the probability that a nucleus suffers any change in passing through matter.

In the majority of the cases of interest, accurately measured cross-section data are not available, and we are forced to make interaction corrections based on empirical formulae.

The available data does however, support the position that the variation in the correction among the isotopes of any element is not large.

We have also been guided in the interaction corrections by a self-consistency principle: We can measure the chemical abundances of the cosmic rays in the CxS mode, which corresponds to a depth of only 4.62 gms.cm-2 in the instrument; the corrected elemental fluxes above the instrument arrived at from the CxS mode of analysis must agree with the elemental fluxes which we obtain from the CxE analysis, which corresponds to the same particles stoppping deeper in the instrument.

To obtain fragmentation cross-sections for materials encountered in the instrument and the atmosphere, we use the target factor γ_m presented by Lindstrom et al. (1975) to multiply the semi-empirical proton-nucleus (or hydrogen) cross-sections Wjk(E) which are presented in Chapter 6. These authors have shown that the nucleus-nucleus partial cross-sections of Carbon and Oxygen on Be, C, Al, Ca, and Pb can be precisely related to the proton-nucleus cross-sections through the factor

$$\gamma_m = 0.26\ t_m^{\cdot 5}(r_m + 3.0)$$

where:

r_m is the measured half-density electron charge radius, and

t_m is the charge skin thickness of the target (Hofstadter and Collard, 1967).

We estimate the total interaction cross sections for charge-altering nucleus-nucleus collisions using the empirical

INTERACTION MEAN FREE PATHS

(gm•cm-2)

Nucleus	Inelastic Cross-Section in Hydrogen (mb)	Hydrogen	Carbon*	Nitrogen	Aluminum*
26 Fe^{56}	715	2.33	9.98	13.7	17.4
14 Si^{28}	435	3.83	16.0	18.9	26.4
10 Ne^{20}	341	4.89	18.7	21.92	30.5

*Adjusted to include neutron-stripping interactions.

Table 5.2

formula of Meyer and Casse (1975):

$$W_t = 60.5(A^{1/3} + A_m^{1/3} - .93)^2 \text{ mb.}$$

In the case of collisions with hydrogen, we use the formula

$$W_t = 10\pi(1.31\ A^{1/3})^2\ (1-.47\ A^{-.4})\ \text{mb}$$

(Silverberg and Tsao, 1976). Table 5.2 shows typical interaction mean free paths λ which we have used in calculating the interaction corrections. λ is related to the total cross-section by:

$$\lambda = (6\cdot E\text{-}4\ W_t/Am)^{-1}\ \text{gms/cm}^2,$$

and includes a small correction for the effect of neutron-stripping interactions in the instrument.

2.1 INSTRUMENTAL CORRECTIONS

It is necessary to make two levels of interaction corrections before arriving at mass histograms above the instrument. The first step is to subtract the events that can be attributed to neutron-stripping from the estimated isotope totals. Then we may consider the total effect of fragmentation in the instrument on the flux of each species.

Neutron stripping reactions will only be rejected by our consistency criteria in the case of a knock-on proton causing a signal in the counter following the detector in which the main portion of the incident nucleus stops. The

probability of this occurring is very low; therefore, in order to give isotope counts which are free from contamination due to neutron-stripping reactions, we must subtract the estimated number of events of this type from the observed number of events. Since we see an appreciable fraction of Iron-54, for example, the correction for this effect could be quite important.

To estimate the number of neutron-stripping events, we consider interactions occurring from the top of the instrument to the mean depth of the analyzed particles of each charge in E1 or E2. For Iron, this depth is 10.66 gms.cm-2, or 1.39 mfp; while for Neon, the depth is 19.6 gms.cm-2, but the mean free path is 15.5 gms.cm-2, giving a depth of 1.26 mfp in the instrument. The expected number of neutron stripping counts for each species is given in Table 5.1, column 5. We have calculated this number using the following formula:

$$N_s = \underline{N_k \exp(aW_t X)}\,(1-\exp[-aW_t X])\,W_{jk}/W_t$$

$$= N_k\,(\exp[aW_t X]-1)\,W_{jk}/W_t$$

where:

Nk = the observed number of particles which may strip to the specified j (without charge loss),

W_t = the total inelastic cross-section of the k-th isotope of the charge considered, greater in mass than j,

W_{jk} = the cross-section for neutron stripping from the isotope k to the isotope j, and

X = the material thickness from the top of the instrument to the mean depth of each charge in the E counters.

The underlined term in line 1 of this formula is the estimated number of particles of species k which were incident on the instrument. Of these,

$$1-\exp(-aW_t X)$$

fragment, and of the fragmenting particles, W_{jk}/W_t strip to species j.

This correction is largest when a very abundant isotope is above an isotope we wish to measure. In the case of Fe-54, for example, stripping from Fe-56 and Fe-58 accounts for about half of the observed number of events.

Displayed in column 6 of the table are the observed number of counts less the contribution from neutron stripping. The error of each value is given in column 7. The errors quoted include the estimated uncertainty due to mass distribution overlap.

The instrumental corrections are concluded by estimating the flux of particles which, incident on the top of the experiment, produced the values shown in column 6. We do this by multiplying each abundance value by

$$\exp(X/\lambda)$$

which is the inverse of the fractional attenuation which each isotopic component of the cosmic ray suffers in coming

to rest in the instrument. We demand consistency between the chemical fluxes obtained with the CxS and CxE analyses at this point. In the case of Iron, the chemical fluxes were in agreement to within 7%, which provides an important verification of the procedures we have followed. The Ne, Mg, and Si fluxes in the CxE analysis were about 18% higher than those in the CxS analysis. We have interpreted this difference as indicating incomplete interaction rejection in the E2 analysis region (see Section 4.0). Therefore, we have decreased the total interaction correction for the particles which stop in E2 by a constant factor of 1/1.18 to compensate for these undetected nuclear interactions in E2. The number of particles of each species above the instrument is shown in column 8.

2.2 ATMOSPHERIC CORRECTIONS

Atmospheric interactions result in the build-up of secondary nuclei and the break-up of primaries. Since secondaries may also break into tertiary species, we have a network of nuclear fragmentation reactions, which we follow using the propagation code described in the next chapter. We do not consider the process of ionization energy loss here, because our energy intervals have already been referenced to the top of the atmosphere. Because the variation of cross-section with kinetic energy is small over the interval considered, the two corrections are

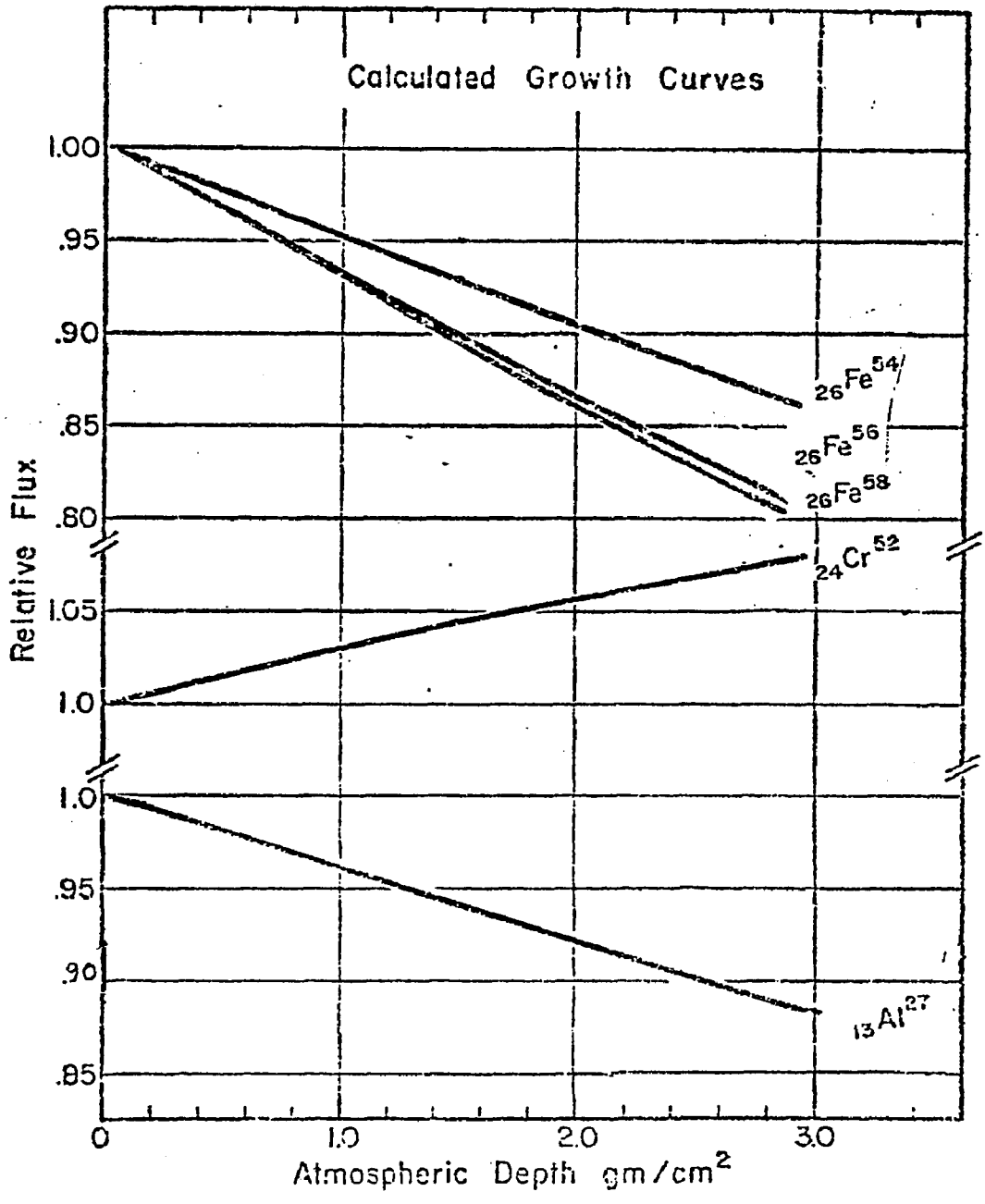

Figure 5.4

Variation of Isotopic Intensity
with Atmospheric Depth

essentially independent. Our calculation is one-dimensional, neglecting the small angular variations of the secondary from the path of the primary particle.

We perform the atmospheric corrections by:

1. estimating the extra-atmospheric flux of particles,

2. calculating the fluxes which these would produce at the instrument, and

3. multiplying the value of the number of counts of each species incident on the instrument (column 8) by the ratio of the estimated flux above the atmosphere to that calculated at the instrument.

Column 9 shows the results of the atmospheric correction. A mean atmospheric depth of 3.0 gms.cm-2, corresponding to the instrument's average zenith angle of 18 degrees, has been used in making this correction. The magnitude of the correction ranges from +25%, for Fe-56, to -7%, for Cr-52, which is built up in the atmosphere by fragmentation from Iron. Figure 5.4 shows the change of intensity of several nuclides with depth in the atmosphere (growth curves), as predicted by our propagation calculation.

The numbers in column 9 refer to particles in different energy intervals; therefore, they are not directly comparable. The extreme case is Neon, measured in a 40 MeV/n interval at an average energy of 460 MeV/n, versus Iron, measured in a 133 MeV/n interval at 600 MeV/n. We normalize the interval

widths by giving the number of counts/MeV/n in column 10.* Then we use the measured energy spectrum of Iron, presented in Meyer et al., 1974, to normalize our results to the same energy (600 MeV/n) for all charges and isotopes. These results, corrected in this way for energy differences, are shown in column 11. Because the energies involved are near the peak of the cosmic ray differential energy spectrum, the spectral correction is less than 16% between all charges, while the spectral corrections for isotopes of the same charge differ by less than 6%.

3.0 ABUNDANCES ABOVE THE ATMOSPHERE

Isotopic fractions of each element are given in column 12, while in column 13 the abundance of each isotope is referenced to Fe-56. Of special note in the isotopic ratios are the following observations:

1. IRON has a substantial abundance (20.4+/-5.0)% of Fe-58. This component cannot be produced by propagation effects, and is the first clear signal that the source material of the cosmic rays is different from material typical of our solar system. The abundance of Fe-54 at the top of the atmosphere is (6.0+/-4.0)%, only marginally above

---

* Counts/MeV may be converted to Peters by dividing by the product of the geometrical factor (.0824 sq.m-ster), the instrument time at altitude (28.4 hours), the dead-time correction (0.89), and a correction factor for the rejection of good events by the selection criteria. This last factor depends on the particular selection criteria in each mode of analysis, and varies from 0.75 to 0.90.

the criterion for significance. The mean mass of Iron is 56.29+/-0.1 AMU.

2. CHROMIUM was observed in the instrument with equal abundances of isotopes 50 and 52 (4 counts each), and one event each of isotopes 48, 51 and 54. After corrections, we still have roughly equal abundances of Cr-50 and Cr-52, giving a mean mass of 51.0+/-0.4 AMU.

3. TITANIUM has the dominant isotope 48 (74+/-12)%, and mean mass 47.6+/-0.2. No Ti-44 is seen. (Titanium 44 is an electron capture isotope of half-life 48 years.)

4. SCANDIUM was used as a response-function calibration point, assuming it to be 100% Sc-45. The mean mass of events with masses between 44.0 and 46.0 in the raw data is 45.17. We attribute all the counts at the top of the atmosphere to Sc-45.

5. CALCIUM is largely Ca-42. Other species constitute half or less of Calcium. Ca-40, which in previous work has been assumed to be the dominant Calcium isotope, is <17% of the total. Calcium's mean mass is 42.30+/-0.12 AMU.

6. SULPHUR is predominantly S-32, with possibly some S-33 present. The mean mass is 32.30+/0.13 AMU.

7. SILICON appears to be mainly Si-28: Si-29<30%, and Si-30<5%. The mean mass is 28.21+/-0.10 AMU.

CHEMICAL ABUNDANCES OF THE COSMIC RAYS

(Relative to Iron = 1.00)

Element	This Experiment		Webber et al., 1972 (FC)	Garcia-Munoz et al., 1977 (FC)	Ormes 1976 (AI)	Julliot et al., 1975 (FC)	Benegas et al., 1975 (FC)	UNH 1974 C×S (AI)
	Above Instrument (AI)	Fully Corrected (FC)						
$_{26}$Fe	1.00	1.00	1.00	1.00	1.00	1.00	1.00	1.00
$_{24}$Cr	.11±.04	.08±.03	.20 ±.03*	.16 ±.02	.214±.011*	.126±.016*	.13±.02	
$_{22}$Ti	.14±.05	.12±.04	.19 ±.03	.167±.013	.217±.011	.160±.016	.17±.02	
$_{21}$Sc	.10±.05	.08±.04	.056±.015	.044±.006	.091±.007	.039±.017	.05±.01	
$_{20}$Ca	.23±.07	.19±.05	.29 ±.03	.233±.015	.304±.011	.229±.023	.27±.02	.16
$_{16}$S	.22±.07	.21±.06	.28 ±.03	.278±.018	.464±.014*	.302±.029	.34±.03	
$_{14}$Si	1.25±.29	1.11±.25	1.34±.07	1.75±.07*	2.05±.03*	1.357±.070	1.53±.08	1.41
$_{13}$Al	.44±.15	.43±.14	.34 ±.04	-	.536±.014	.202±.039*	.45±.06	
$_{12}$Mg	2.32±.36	1.96±.31	2.00±.09	-	2.85±.043	1.721±.078	2.04±.16	2.20
$_{11}$Na	.50±.18	.41±.14	.38 ±.04	-	.616±.018	.085±.031*	-	
$_{10}$Ne	1.90±.36	1.50±.28	1.91±.09	-	2.30±.03	1.349±.070	-	1.76

* >2σ disagreement with this experiment.

Table 5.2

8. ALUMINUM appears to be predominantly Al-27. The mean mass of Aluminum is 26.93+/-0.20 AMU.

9. The primary isotope of MAGNESIUM, Mg-24, is complemented with definite Mg-25 and Mg-26 components, which make up (40±6)% of the total. With these components, the mean mass of Magnesium is 24.59+/-.07 AMU.

10. SODIUM appears to be predominantly Na-23, as would be expected, since this is the only stable isotope. The mean mass of Na is 22.74+/-0.11 AMU.

11. Like Magnesium, NEON also appears to have heavier isotopes standing apart from the dominant isotope (Ne-20): Ne(21+22) are (36±18)% of the total, giving Neon a mean mass of 20.56+/-0.12 AMU.

The chemical ratios are also of interest, although no new information is given in these values. Table 5.3 shows the measured abundances of each element relative to Iron, above the instrument, and above the atmosphere. For comparison, several other recent measurements of the chemical composition are given which show good agreement with the values from this experiment.

4.0 INSTRUMENTAL PERFORMANCE

It is of interest to compare the observed mass resolutions (which we can measure for the most abundant isotopes) to those predicted in the design study (Chapter III) and

RESOLUTIONS: OBSERVED AND PREDICTED

	Neon	Magnesium	Silicon	Iron
Observed*	0.43±.07	.45±.05	.68±.07	.40±.06
Predicted	0.4	.45	0.5	0.6

*Resolutions quoted are for the "restricted" case.

Table 5.4

interpret any differences between the two. Table 5.4 gives the data for this comparison. Recall that the predicted Cerenkov resolutions are based on the extrapolation of v=1 resolution data for each charge. We notice that the Iron resolution is somewhat better than that expected, while the Neon-Silicon resolutions are somewhat worse. Therefore, it is of interest to carefully examine the premises which went into the original predictions. In considering the Iron result, it appears that the limiting factor in Cerenkov resolution, the pathlength correction, must have been slightly better than was deduced from the analysis of high-energy particles. The explanation for this may lie in part in the larger contribution to the Cerenkov resolution of knock-on electrons at high energies (see Section 2.2). On the basis of the Iron isotope result, we place the FWHM limiting resolution of the Cerenkov counter at about 4%, instead of 6% as indicated in Figure 2.5. The low-Z results, showing the opposite tendency, point to a resolution weakness in E2, the counter in which these particles stopped. This is consistent with the observation made during the instrument's construction that E2 was the most difficult detector to compensate, due to the low level of signal observed from the electron reference source. E2 was viewed directly by a single 5-inch photomultiplier. This contrasts with the superior deisgn of E1, which was viewed by reflected light with four 5-inch photomultipliers. We therefore believe that the limiting resolution in the E2 counter was probably due to compensation non-uniformities.

It is also of interest to explain why the interaction rejection mechanisms were apparently more effective for particles stopping in E1 than for particles stopping in E2. Two factors which tended to diminish the power of the mechanisms in E2 were: (1) the flat geometry of E1, which contributes about 10% resolution broadening to the E1-S consistency criterion; and (2) the PEN counter resolution, which being much larger than that of E2 may have allowed some events with a fragment signal to pass.

CHAPTER VI

COSMIC RAY PROPAGATION

The corrected abundance values presented in chapter V refer to particles which, since their acceleration, have been conditioned by exposure to the modulating effect of the solar magnetic field and by exposure to the interstellar medium for some 1.E7 years. By carefully removing these effects, we can hope to arrive at the source abundances of the cosmic rays, and thus draw inferences about their origin. The principles to follow are well established by previous work. Section 1 gives the solar modulation corrections, and section 2 is a discussion of interstellar propagation theory. Section 3 discusses the numerical application and predictions of the standard propagation theory, comparing previously derived source abundances to those which can be derived on the basis of this work.

1.0 SOLAR MODULATION

At the energies we are studying, the force-field approximation (Gleeson and Axford, 1968) is considered to give a good account of the modulation of galactic cosmic rays. In this approximation the flux Je of the cosmic rays at the earth is related to the flux Jo outside the influence of solar modulation by

$$J_e(E) = \frac{E^2 - m_0c^2}{(E+\Phi)^2 - m_0c^2} J_o(E+\Phi)$$

where:

E = total particle energy (kinetic + rest), Mev.

Φ = force-field energy loss, Mev,

m_0c^2 = particle rest energy

J = flux of particles/Mev

For August, 1974, Webber (1977) estimates the value 96+/-20 Mev for the force-field energy loss for (A/Z)=2 particles. This figure describes the effective energy loss of cosmic rays entering the expanding sphere of the solar wind. When we correct the mean energies of each element for this effect, we find that before solar modulation the mean energy of each isotopic species in our observations is 695+/-6 Mev.

2.0 INTERSTELLAR PROPAGATION THEORY

Three important processes affect the cosmic rays in the interstellar medium: fragmentation, ionization energy loss, and scattering by the galactic magnetic field. No exact treatment of the detailed scattering process exists, but the diffusion approach is believed to be valid at these energies. The diffusion model which has been most successful in explaining the composition observations made during the last decade has been the "leaky-box" model

(Cowsik et al,1967). We devote the next several paragraphs to a review of this propagation model, and its background in the observation and theory of the galactic structure.

Observations of the galactic magnetic field (Hiltner, 1956, Manchester, 1971) tell us that the mean field strength is about 3E-6 Gauss, and that it is ordered along the spiral arms of the galaxy. Fluctuations in the field the order of the field itself are observed with scale sizes 1.E11 cm. Comparing the gyroradius of a 1 Gev cosmic ray nucleus in this field (2.E12 cm) to the characteristic thickness of the galactic disk (1.E21 cm) suggests strongly that the particles are effectively tied to the local magnetic field. Studies of the effects of scattering and gradient and curvature drifts (Jokipii and Lerche, 1969; Jokipii, Lerche and Schommer, 1969) concur in this view. Parker (1973), and Jokipii (1973) argue that the topology of the magnetic field is most probably closed. Parker (1965, 1975) also argues that since the cosmic rays constitute a relativistic gas of pressure comparable to that of the confining magnetic fields, and since they are tied to the magnetic field, escape from the galaxy is possible only if and when the pressure of the cosmic rays builds a bubble in the galactic field which bursts open at the disk surface. Further, a closed magnetic topology gives a natural explanation for the observed smooth energy spectrum up to 1.E7 GeV, whereas an open topology seems likely to allow escape of high-energy

particles along the magnetic lines of force, causing the cosmic ray energy spectrum to steepen at 100 or 1000 GeV.

Following arguments such as these, and seeking a model which can produce the observed fluxes of the rare elements Li, Be, B in the cosmic rays, propagation theorists have devised models in which the galaxy is represented as a closed box within which cosmic rays propagate with an exponential distribution of lifetimes. The mean lifetime is determined by the sum effect of lifetimes against escape, fragmentation, and energy loss by ionization of the medium.

Jones (1975) and Owens(1975) describe the mathematical justification for the model we use in the propagation calculations. We follow Owens' discussion here.

It is assumed that cosmic rays propagate by diffusion in the disk of the galaxy. The diffusion equation for particle density N(x,t) is:

$$\frac{\partial N}{\partial t} = \frac{\partial}{\partial X_i}\left(K_{ij} \frac{\partial N}{\partial X_j} \right) + S$$

where:

Kij($\underline{x}$,t) is the diffusion coefficient tensor, and

S($\underline{x}$,t) is the rate of particle production (particles/cc-sec).

The boundary condition assumed is N=0 at the surfaces of the disk. The disk is assumed to be of thickness 2D and radius

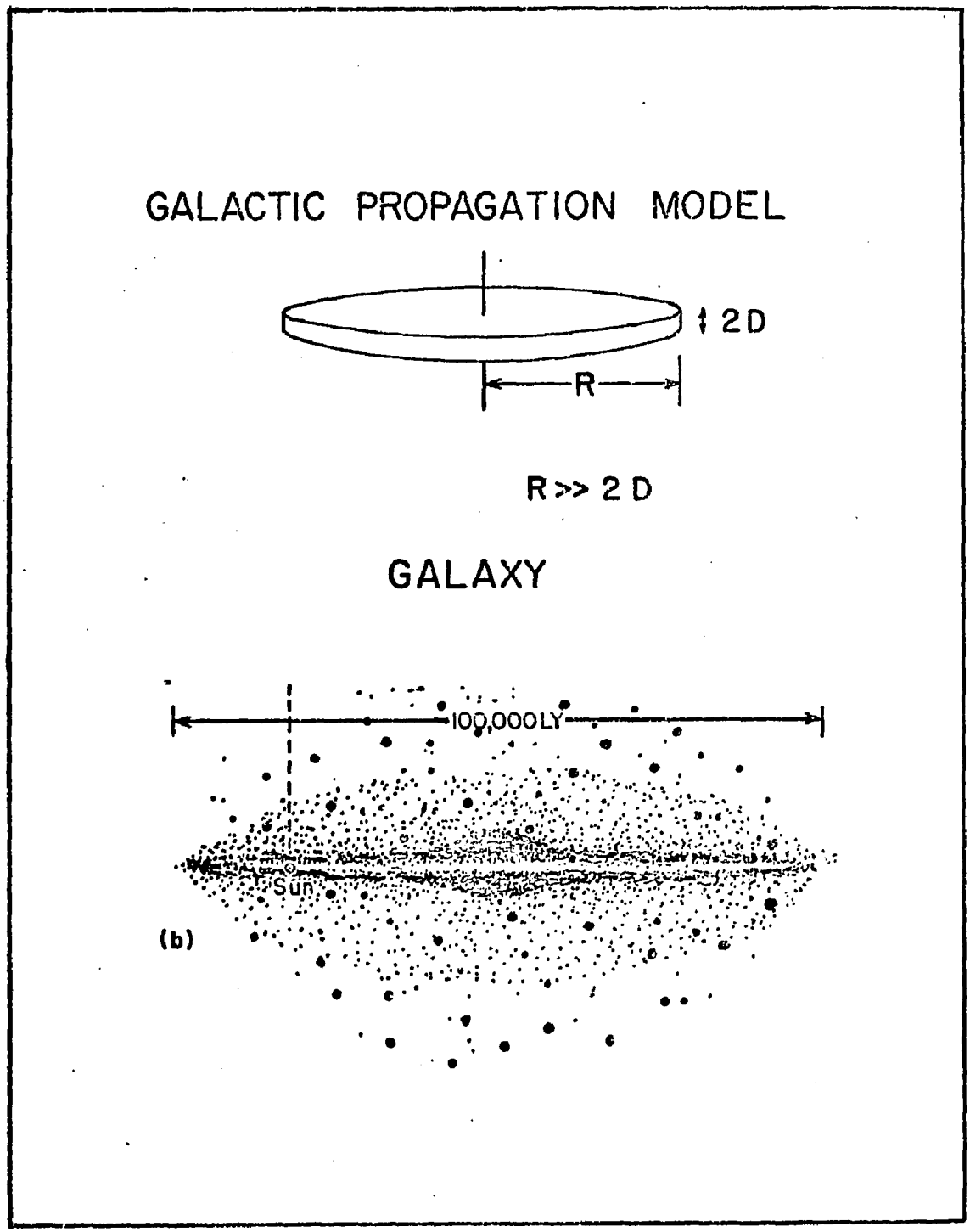

Figure 6.1 Galactic Propagation Model

R, where D is assumed to be small enough so that only diffusion perpendicular to the surfaces is important

$$\text{i e:} R/K_{\parallel} >> D/K_{\perp}$$

where $K_{\parallel}$ and $K_{\perp}$ are components of the diffusion tensor parallel to the galactic plane and perpendicular to it, respectively (see Figure 6.1). The diffusion coefficient is taken as constant within the galaxy. The one-dimensional equation

$$\frac{\partial N}{\partial t} = K \frac{\partial^2 N}{\partial z^2} + S \quad \text{with } N(z=\pm D)=0 \quad \text{and } K=K_{\perp}$$

results. The Green's function solution for arbitrary source function is:

$$N(Z,t) = \int_{-D}^{D} dZ' \int_{-\infty}^{\infty} dt' S(Z',t') g(Z,Z',t,t')$$

where the Green's function is

$$g(Z,Z',t,t') = \frac{1}{D} \sum_{n=1}^{\infty} \left\{ \exp\left[-Kn^2\pi^2(t-t')/4D\right] \sin\left[n\pi(Z+D)/8D\right] \sin\left[n\pi(Z'+D')/8D\right] \right\}$$

For a uniform distribution of cosmic ray sources throughout the galaxy, the distribution of cosmic ray ages is

$$f(\tau) = \frac{4N}{\pi} \sum_{\substack{n=1 \\ \text{odd}}}^{\infty} \frac{1}{n} \exp\left[-Kn^2\pi^2\tau/4D^2\right] \sin\left[n\pi(Z+D)/2D\right]$$

while when the sources are concentrated in the central plane of the disk, one has

$$f(\tau) = R \sum_{\substack{n=1 \\ \text{odd}}}^{\infty} \exp\left[-Kn^2\pi^2\tau/4D\right] (-1)^{n-1} \sin\left[n\pi(Z+D)/2D\right]$$

In these cases, the mean lifetime is

$$\tau = 4D/\pi^2 K$$

and for lifetimes greater than the mean, the first term in the series dominates, and the shape of the distribution is exponential. Owens also shows that the same observation holds in the case of a spherically symmetric model, with either a uniform or localized source, if we replace D by R, the radius of the confinement region.

In the propagation model which we introduce next, we will make use of the equivalence of an exponential distribution of cosmic ray lifetimes to an exponential distribution of pathlengths. This equivalence holds because pathlength is (approximately) a constant times the lifetime:

$$x = \rho v \tau \qquad \text{gms} \cdot \text{cm}^{-2}$$

where:

ρ = density of the medium, gms.cm-3

v = particle velocity.

3.0 PROPAGATION MODEL

Three factors are considered in our numerical model of cosmic ray transport: energy loss by ionization in the interstellar medium, composition change by fragmentation, and the exponential distribution of lifetimes. The

calculation is started by setting up an initial source abundance distribution with a total energy spectrum of the form:

$$\frac{dJ}{dE} = \text{const}/(A+E)^{\gamma}$$

where:

$\gamma = 2.65$,

$A = M_o c^2 = 938$ Mev,

J = particle flux/Mev.

A discrete set of energies is used, which span the range from 100 Mev to 100 Gev. We trace the changes in the composition and energy of the distribution as it is transported through successive small steps of the interstellar medium. At each step, the fragmentation and energy-loss of the particles are calculated, and the abundance distributions and energies are modified to reflect these processes. Then we interpolate from the new abundance values and energies to find the fluxes at the fixed energy points chosen initially. These flux values constitute the inputs to the next step. This procedure integrates the transport equation

$$\frac{dN_j(E,x)}{dx} = \sum_{k=1}^{M} N_k W_{jk}(D) - \frac{\partial}{\partial E}\left(N_j \frac{dE}{dX}\right)$$

where:

M = total number of species transported, and

CROSS-SECTION TABULATION FOR Z= 26., A= 56.

SECONDARY	ENERGY (MEV): 100.	147.	215.	316.	464.	681.	.100E+01	.147E+01	.215E+01	.316E+01
26. 56.	-715.	-715.	-715.	-715.	-715.	-715.	-715.	-715.	-715.	-715.
26. 55.	101.	73.2	60.0	56.4	53.7	51.3	49.7	48.9	48.6	48.6
25. 55.	18.5	16.1	18.0	22.9	27.1	30.2	31.3	25.9	23.8	23.8
26. 54.	83.7	43.9	40.0	34.7	28.4	22.7	19.3	18.3	18.2	18.2
25. 54.	128.	67.2	61.3	53.1	43.5	34.7	29.5	28.0	27.8	27.8
24. 54.	1.91	2.80	3.82	3.82	3.82	3.82	3.82	3.82	3.82	3.82
26. 53.	70.0	36.8	33.7	29.3	24.2	19.6	15.8	16.0	15.9	15.9
25. 53.	140.	73.4	67.1	58.5	48.3	39.1	33.6	32.0	31.8	31.8
24. 53.	67.8	49.4	30.2	23.8	21.4	18.4	14.9	11.7	9.39	9.21
26. 52.	2.33	1.83	1.14	.952	.911	.821	.688	.555	.452	.404
25. 52.	79.2	62.1	39.0	32.4	31.0	28.0	23.4	18.9	15.4	15.1
24. 52.	160.	126.	78.8	65.6	62.7	56.6	47.4	38.2	31.1	30.6
25. 51.	16.8	14.2	9.11	8.01	8.14	7.68	6.65	5.50	4.57	4.49
24. 51.	89.9	75.9	48.8	42.9	43.6	41.2	35.7	29.5	24.5	24.1
23. 51.	12.7	10.7	6.91	6.07	6.17	5.82	5.04	4.17	3.46	3.40
24. 50.	36.1	32.8	21.7	20.1	21.7	21.4	19.2	16.3	13.8	13.6
23. 50.	28.9	26.3	17.4	16.1	17.4	17.2	15.4	13.0	11.0	10.9
22. 50.	3.65	3.31	2.19	2.03	2.20	2.17	1.94	1.65	1.39	1.37
24. 49.	4.91	4.80	3.26	3.20	3.67	3.79	3.51	3.05	2.63	2.59
23. 49.	40.6	39.6	26.9	26.4	30.3	31.3	29.0	25.2	21.7	21.4
22. 49.	7.55	7.39	5.01	4.92	5.64	5.83	5.40	4.69	4.04	3.99
24. 48.	.925	.973	.678	.708	.857	.926	.897	.791	.694	.686
23. 48.	19.1	20.1	14.0	14.6	17.7	19.2	18.4	16.4	14.4	14.2
22. 48.	22.4	23.5	16.4	17.0	20.7	22.4	21.4	19.1	16.8	16.6
20. 48.	.970E-02	.102E-01	.712E-02	.739E-02	.899E-02	.972E-02	.931E-02	.830E-02	.728E-02	.720E-02
23. 47.	4.49	5.08	3.64	3.99	5.16	5.83	5.78	5.20	4.73	4.68
22. 47.	21.4	24.2	17.3	19.0	24.6	27.8	27.6	25.2	22.5	22.3
21. 46.	5.46	6.65	4.89	5.67	7.78	9.21	9.44	8.34	8.36	7.99
22. 46.	11.4	13.9	10.2	11.8	16.2	19.2	19.7	18.5	16.8	16.7
20. 46.	.218	.265	.195	.226	.310	.367	.376	.353	.321	.319
21. 45.	13.4	17.6	13.2	16.2	23.7	29.3	31.1	29.9	27.7	27.5
21. 44.	4.22	5.95	4.61	5.98	9.25	12.0	13.1	12.9	12.2	12.2
20. 44.	1.97	2.79	2.16	2.80	4.33	5.61	6.15	6.06	5.73	5.70
22. 44.	.347	.490	.380	.492	.761	.986	1.08	1.07	1.01	1.00
21. 43.	1.12	1.70	1.35	1.86	3.05	4.13	4.69	4.74	4.56	4.55
20. 43.	2.52	3.82	3.04	4.17	6.85	9.28	10.5	10.6	10.2	10.2
19. 42.	.660	1.08	.880	1.28	2.23	3.16	3.70	3.83	3.76	3.76
20. 42.	2.31	3.77	3.08	4.46	7.78	11.0	12.9	13.4	13.2	13.1
20. 41.	.408	.711	.596	.913	1.69	2.51	3.04	3.23	3.23	3.23
19. 41.	1.09	1.91	1.60	2.46	4.55	6.75	8.19	8.70	8.70	8.70
19. 40.	.811	1.53	1.32	2.14	4.21	6.53	8.19	8.93	9.10	9.11
20. 40.	.864E-01	.164	.141	.228	.448	.696	.873	.951	.969	.971
18. 40.	.327	.619	.533	.862	1.70	2.63	3.31	3.60	3.67	3.67
19. 39.	.257	.524	.463	.792	1.66	2.69	3.49	3.90	4.04	4.06
19. 38.	.529E-01	.116	.105	.190	.422	.718	.963	1.10	1.17	1.17
18. 38.	.853	1.87	1.70	3.07	6.80	11.6	15.5	17.8	18.8	18.9
18. 37.	.188	.443	.413	.789	1.86	3.31	4.59	5.39	5.81	5.84
17. 37.	.203	.479	.447	.854	2.01	3.58	4.97	5.83	6.29	6.33
17. 36.	.244	.619	.592	1.20	2.99	5.57	7.99	9.62	10.6	10.7
18. 36.	.478E-01	.121	.116	.235	.587	1.09	1.57	1.89	2.07	2.09
16. 36.	.407E-01	.103	.988E-01	.200	.500	.930	1.33	1.61	1.76	1.78
16. 35.	.769E-01	.210	.206	.440	1.17	2.28	3.38	4.17	4.67	4.72
17. 35.	.104	.284	.279	.595	1.58	3.08	4.57	5.58	6.31	6.38
16. 34.	.170	.500	.505	1.14	3.22	6.55	10.1	12.7	14.5	14.7
15. 33.	.322E-01	.102	.105	.251	.754	1.61	2.55	3.31	3.85	3.90
16. 33.	.560E-01	.177	.184	.438	1.31	2.80	4.44	5.77	6.69	6.78
15. 32.	.481E-01	.164	.174	.439	1.40	3.12	5.12	6.81	8.06	8.18
16. 32.	.168E-01	.571E-01	.607E-01	.153	.487	1.09	1.78	2.37	2.81	2.85
16. 31.	.178E-02	.650E-02	.710E-02	.189E-01	.640E-01	.149	.254	.346	.417	.428
14. 31.	.109E-01	.400E-01	.437E-01	.116	.393	.918	1.56	2.13	2.56	2.61
15. 31.	.328E-01	.120	.131	.349	1.18	2.75	4.58	6.33	7.69	7.82
14. 30.	.289E-01	.114	.128	.360	1.29	3.16	5.54	7.76	9.53	9.70
14. 29.	.151E-01	.642E-01	.739E-01	.220	.839	2.14	3.89	5.59	6.99	7.13
14. 28.	.539E-02	.245E-01	.293E-01	.913E-01	.370	.987	1.86	2.73	3.48	3.55
13. 27.	.844E-02	.414E-01	.503E-01	.167	.719	2.01	3.91	5.90	7.56	7.83
13. 26.	.201E-02	.106E-01	.132E-01	.465E-01	.212	.620	1.25	1.93	2.55	2.62
12. 26.	.473E-02	.250E-01	.311E-01	.109	.500	1.46	2.94	4.55	5.92	6.16
12. 25.	.371E-02	.211E-01	.270E-01	.100	.487	1.49	3.10	4.91	5.62	6.80
12. 24.	.159E-02	.971E-02	.128E-01	.502E-01	.258	.827	1.78	2.89	3.97	4.08
11. 23.	.196E-02	.129E-01	.174E-01	.722E-01	.395	1.32	2.94	4.91	6.87	7.07
11. 22.	.102E-02	.589E-02	.714E-02	.295E-01	.171	.600	1.38	2.36	3.37	3.47
10. 22.	.114E-02	.659E-02	.799E-02	.330E-01	.192	.672	1.55	2.64	3.77	3.89
10. 21.	.138E-02	.802E-02	.972E-02	.384E-01	.210	.718	1.71	2.99	4.34	4.49
10. 20.	.142E-02	.821E-02	.996E-02	.393E-01	.215	.735	1.68	2.89	4.21	4.36
9. 19.	.183E-02	.106E-01	.129E-01	.508E-01	.278	.951	2.17	3.74	5.39	5.57
TOTALS	.629E+05	.467E+05	.350E+05	.327E+05	.340E+05	.345E+05	.337E+05	.320E+05	.306E+05	.305E+05
PRIMARY	-.400E+05	-.400E+05	-.400E+05	-.400E+05	-.400E+05	-.400E+05	-.400E+05	-.400E+05	-.400E+05	-.400E+05

Table 6.1 Hydrogen Cross Sections

Wjk = the cross-section for fragmentation from nuclide k to nuclide j.

We determine spectral abundances Nj(E,x) for each species j at .25 gm.cm-2 intervals of interstellar pathlength x spanning 0-10 gms.cm-2 (slab model abundances). Weighting these with an exponential pathlength factor exp(-x/L) we obtain the abundance distributions which correspond to an exponential distribution of lifetimes. We use the value L=6 gms.cm-2 for the mean pathlength, in accordance with current estimates based on the ratio of secondary to primary species at energies comparable to those we are discussing (Silverberg et al, 1976).

3.1 FRAGMENTATION CROSS-SECTIONS

Fragmentation cross-sections Wjk for protons on nuclei (hydrogen cross-sections) are given by Silverberg and Tsao (1973, 1976), and Perron, (1975). Silverberg and Tsao give a semi-empirical formula which is of great utility for calculating the many cross-sections which are unmeasured. The formula fits most of the measured cross-sections. Perron (1975) gives recent measurements of proton-iron cross-sections for fragment nuclei with Z>20 which we use instead of the semi-empirical formula, in the cases when they disagree. As an example, the cross sections for Iron on hydrogen are shown as a function of energy and secondary species in Table 6.1.

COSMIC RAY PROPAGATION RESULTS

	Observed Isotope Fractions	Abundance Relative to Fe-56	Shapiro	% Predicted Fractions	Predicted Relative Fe-56	Perron (1975) Predicted Fractions	New Source Rel. Fe-56	Predicted Isotope Fractions (%)	Predicted Rel. Fe-56
Fe^{58}	20.4±5.0	27.8±8.1	-	-(1)	0	-	29	20.5(2)	28
Fe^{56}	73.6±5.8	100	100	93	100	-	100	73.3	100
Fe^{55}	0	0	-	4.6	4.9	-	0	4.1	5.6
Fe^{54}	6.0±4.0	8.1±5.5	-	2.1	2.3	-	0	2.0	2.7
Cr^{52}	51±18	5.9±2.0	-	45	9.1	42	-	45	11
Cr^{51}	-	-	-	28	5.8	24	-	26	6.4
Cr^{50}	49±19	5.6±3.1	-	14	2.9	20	-	13	3.2
Ti^{50}	74±12	12.2±4.9	-	33	6.3	36	-	34	8.1
Ti^{47}	14±14	2.4±2.5	-	30	5.6	30	-	30	6.7
Ti^{46}	12±13	2.0±2.3	-	29	5.4	27	-	28	6.6
Sc^{45}	100	11.2±5.1	-	100	4.5	-	-	100	4.5
Ca^{44}	14±9	3.5±2.4	-	19	4.0	-	-	17	5.3
Ca^{43}	14±9	3.5±2.4	-	16(1)	3.4	-	-	15	4.5
Ca^{42}	56±13	14.0±5.0	-	18(1)	3.8	-	-	46(2)	14.0(3)
Ca^{41}	16±10	4.0±2.8	-	3.7	0.8	-	-	4	1.3
Ca^{40}	≤20	≤5	6.6	39(1)	8.4		4	17(2)	5.2
S^{33}	30±13	8.4±4.6	-	8.6	2.3	-	-	8.3	2.9
S^{32}	70±13	19.7±6.6	14	78	21	-	20	82	29
Si^{29}	21±10	32.0±18	90	1.2	1.66	-	22	97	34
Si^{28}	79±10	119.0±37	-	97	134	-	80		117
Al^{27}	93±14	54.0±17	11	100	24	-	15.6	100	33
Mg^{26}	19±4	51.0±13	-	5.0(1)	8.5	-	18.5	15.4(2)	40
Mg^{25}	21±5	56.0±17	-	4.0	6.7	-	28	22	57
Mg^{24}	60±5	159.0±33	93	91	154	-	97.8	63	163
Ne^{22}	20±14	40.0±39	-	10.4	14	-	-	10.6	20
Ne^{21}	16±11	34.0±28	-	6.0	8.1	-	-	6.4	12
Ne^{20}	64±14	130.0±50	57	83	112	-	83	83	156

(1) Discrepancy with observations.
(2) Improved agreement with observations.
(3) Assuming cross-section 26-56 to 20-42 = 27 mb.

Table 6.2. Cosmic Ray Propagation Results

4.0 PROPAGATION RESULTS

Now let us compare the predictions of this model to our observations. Our observations are summarized in columns 2 and 3 of Table 6.2. We begin our comparison by taking a set of previously determined source abundances (Shapiro et al. 1976) and calculating the corresponding abundances outside the heliosphere (in the energy intervals appropriate to this experiment). The Shapiro et al. source abundances are tabulated in column 4 of Table 6.2, and the predicted isotope fractions and absolute abundances relative to Fe-56 which we find by taking these abundances and using our propagation program are shown in columns 5 and 6. The isotopic fractions of Ti and Cr nuclei at the earth calculated by Perron (1975) (column 7), agree very well with our calculations, thus helping to give us confidence our our propagation model.

It is the isotopic ratios which are of most significance in the source abundances, and also of highest reliability in our data. We therefore confine our attention from this point on to these ratios. The significant disagreements between the predicted isotopic ratios and those observed are indicated by "1" in column 5.

To reconcile these differences in the isotopic ratios, we assume a new set of source abundances (column 8) and calculate a new set of isotopic abundances at the boundary of the heliosphere (columns 9 and 10 of Table 6.2) which are

in closer agreement with the measured isotopic fractions. The new source abundances require the presence of both Fe-58 and Fe-56 in significant quantities. With the possible exception of Ca,* our data is consistent with the absence of all elements between S and Fe in the cosmic ray source. In other words, the masking effect of the substantial fluxes of particles produced by fragmentation from iron obscures the ability to measure a source contribution for these elements. In the next chapter we will try to interpret the physical significance of the isotopic source ratios we have measured.

* In the case of Ca the total charge abundance predicted using the semi-empirical cross-section formula is only about 0.3 of that actually measured. In our experiment only 18 Ca nuclei are analyzed for their isotopic abundance, so that it is possible that one is observing an extreme statistical variation. However, our overall charge abundance ratio Ca/Fe = 0.21±.06 is very similar to that obtained by other workers based on much greater statistics. In the past the difference between the predicted and observed amounts of Ca relative to Fe was usually attributed to a source abundance of ^{40}Ca $\simeq$ 15% that of Fe (e.g., Shapiro and Silverberg, 1975); however, that possibility is not allowed by our data since we see only a small amount of ^{40}Ca. We observe that, using the semi-empirical formula of Silverberg and Tsao (1973), the total cross section for Fe fragmenting to Ca is $\sim$ 48 mb. There are no direct measurements to confirm this value and it is possible that it is low. We have carried out a separate calculation using a total cross section of 70 mb (^{40}Ca = 27 mb), and these results are shown in Column 10 of Table 6.2. These predictions are in much closer agreement with our observations. It should be noted, however, that because of the limited statistical accuracy of the data, the uncertainties on the cross sections we would deduce from the data are large--e.g., the total cross section for Ca is 70±15 mb. The data is suggestive, however, that the cosmic-ray Ca isotopic abundance may be unusual. An explanation for this has been suggested by Silverberg et al., 1973, in which, during Si burning, the nuclei could pass through the "bottleneck" at A$\sim$44 directly to the Fe group leaving S, Ar and Ca underabundant. The above authors suggest that perhaps S and Ar are indeed underabundant, and our data, which suggest little ^{40}Ca, point to the possibility that Ca is underabundant in the cosmic-ray source.

CHAPTER VII

SIGNIFICANCE OF THE RESULTS

1.0 INTRODUCTION

In the introductory chapter, the interpretation of our isotopic composition results in the framework of the theory of nucleogenesis was established as a goal. This chapter attempts to fulfill that objective, drawing upon the considerable theoretical groundwork which has been laid in anticipation of isotropic results.

The basic data which theories of the evolution of matter attempt to explain is the abundances of the nuclides. At this point in time (and for the immediate future) we have only two categories of materials which we may sample to obtain information on these abundances. Terrestrial, lunar and meteoritic samples ("solar system" matter) comprise the first category, and the cosmic rays give us the second category. The cosmic rays are our sole sample of material from outside the solar system.

The highest quality of information in both these categories is contained in the isotopic ratios of each element, rather than in the ratios of elements. This is because it is difficult to exclude the possibility of effects which alter chemical ratios having biased our sample. For example, in the case of the local matter abundances, evaporative rates are strongly dependent on atomic number, but very weakly dependent on the mass number of each chemical species. Similarly, in the cosmic rays, a charge dependent acceleration or propagation may obscure or disguise the information which was implicit in the chemical ratios at the birth of the cosmic rays, but the isotopic ratios are much less likely to have been significantly altered by such effects. The isotopic ratios may, on the other hand, be strongly affected by the nuclear processes at the site of their birth.

In this chapter we will first examine and compare the data on local and cosmic ray source isotopic ratios. Then we will review the current work on nucleosynthesis, supernova models and cosmic ray acceleration as they bear on our measurements.

Finally, we will attempt to assess the impact of our data on the current state of knowledge of cosmic ray origin.

SOURCE ABUNDANCES

	No. Initial Counts	Isotopic Source Abundance %		Error %	Solar System %
Fe^{58}	14± 4	22.5	±	5.4	0.33
Fe^{56}	53± 7	77.5	±	6.1	91.7
Fe^{54}	8± 3	< 13			5.8
Si^{29}	19±10	< 34			
Si^{28}	70±14	80	±	10	92
Mg^{26}	26± 6	12.8	±	2.7	11
Mg^{25}	36± 8	19.4	±	4.6	10
Mg^{24}	97±10	67.8	±	5.7	79
Ne^{22}	9± 8	< 32			11
Ne^{21}	10± 6	< 26			.26
Ne^{20}	33± 8	97		$^{+3}_{-49}$	89

Table 7.1 Cosmic Ray Source Abundances

2.0 SOURCE ABUNDANCES

The isotopic cosmic ray source abundances (Chapter VI) contain several new facts which are of overbearing importance, which we attempt to explain here. These facts are shown in Table 7.1. Discussing each of them in turn, we note:

(1) The presence of Iron-58 (22.5+/-5.4)% of the source Iron;

(2) Heavy isotopes of Silicon are less than 34% of Silicon (1σ);

(3) Mg-25 and Mg-26 are each present, at levels of (12.8+/-2.7)% and (19.4+/-4.6)%, respectively;

(4) Ne-21 and Ne-22 constitute the order of 40% of Neon.

Now let us contrast these figures with the isotopic ratios of local matter (Cameron, 1974):

(1) The Iron composition of solar system material is 91.66% Fe-56, 5.82% Fe-54, 2.19% Fe-57, and only .33% Fe-58.

(2) Silicon is 92.2% Si-28, 4.7% Si-29, and 3.09% Si-30. Our cosmic ray data does not disagree with these figures.

(3) Magnesium is 78.7% Mg-24, and about 10% each of Mg-26. Again, our cosmic ray data is not in disagreement.

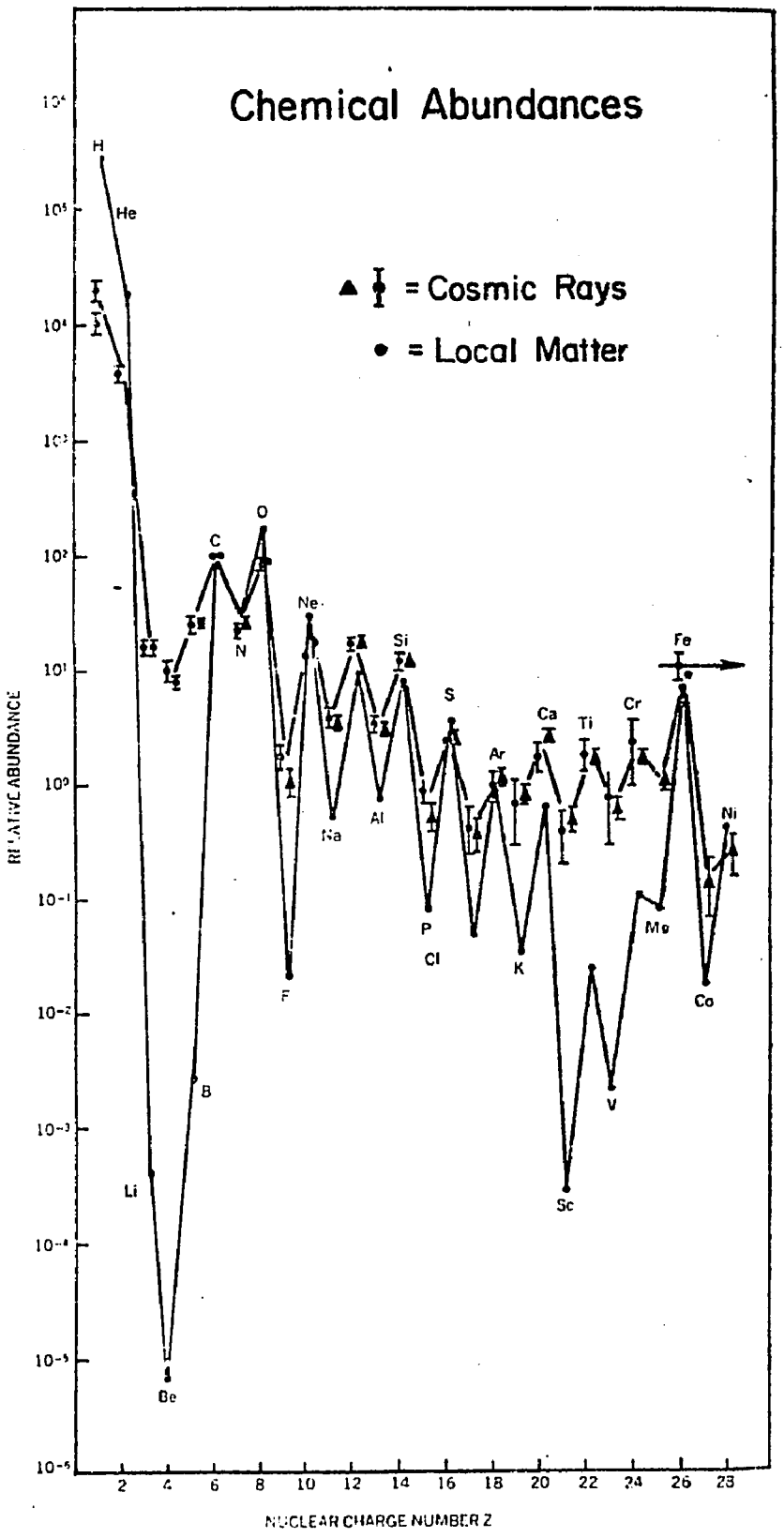

Figure 7.1 Chemical Abundances

(5) Solar System Neon is 89% Ne-20 and 11% Ne-22. Our measurements of Neon are consistent with the above isotopic distribution within the statistical errors.

The principle deviation of our isotopic measurements of cosmic rays at the source from the solar system abundances is for Iron, and it is this difference which we shall focus on in our discussion.

The information from our experiment must, of course, be added to the previously obtained data on chemical and isotopic ratios in the cosmic rays as compared to the local abundances. Figure 7.1, from (Meyer et al., 1974) shows the state of information on chemical ratios. The important factors which can be seen in Fig 7.1 are the overabundance, by six orders of magnitude, of Li, Be, and B in the cosmic rays, and the large enhancements of elements 19 (K) through 25 (Mn). These features find a natural explanation in the fragmentation of the cosmic rays during their transport through the interstellar medium. They yield information on the pathlength-matter density product of the primary cosmic rays, but tell us little about the cosmic ray sources. This is also true of the isotopic information which has been obtained for charges below Neon. The most significant fact which has been obtained from isotopic composition measurements in this range is the cosmic ray lifetime (ca. 1.E7-1.E8 years) which is deduced from the isotopic

composition of Berrylium (Webber et al, 1973b, 1977, and Garcia-Munoz et al, 1976).

3.0 COSMIC RAYS AND NUCLEOSYNTHESIS MODELS

Now we turn our attention to stellar evolution models which have been successful in explaining the solar system abundances, to discover what is necessary to explain the cosmic ray source observations. We draw freely from the literature in the material which follows, notably from Hainebach et al (1976) and Woosley (1975)*. However, before proceeding it is important to be aware of the strong assumptions which go into the comparison of a nucleosynthesis-type abundance fit to the cosmic ray observations. Three of the more obvious assumptions are:

1. that the composition of the interstellar matter near the cosmic ray sources is similar to the composition we observe around us on the earth.

2. that the abundances predicted by nucleosynthesis processes feed equally into the cosmic ray accelerator (no selective acceleration);

3. that the abundances we observe are correlated with a single class of fairly similar events (eg. supernova explosions, not, eg., supernova explosions and interstellar Fermi mechanism).

*The reader is assumed to be familiar with the fundamentals of stellar evolution as presented, for example, in Reeves, 1968.

To explain the solar system abundances of the nuclides with Z> 10, explosive processes are necessary. For this reason, and also in light of the SAS II gamma-ray observations noted by Stecker (1975) which indicate concentrations of cosmic rays around supernova remnants, we narrow the remaining discussion to supernova-associated cosmic ray origin models.

Current supernova models (Arnett (1975) and Arnett and Schramm (1973) are based on the evolution of Helium cores of various masses. These He core masses have been related to main-sequence masses using previous Hydrogen-burning evolutionary calculations (Iben, 1963; Paczynski, 1969). The Helium cores eventually evolve to a 1.4 solar mass Fe-Ni core surrounded by a "mantle" consisting of Si, O, Ne, C, and He as well as mixtures of Mg, S, Ar, etc. Beyond the mantle is an "envelope" consisting of normal interstellar material.

In all the current models of stellar burning which produce Iron, an explosion occurs in which temperatures in excess of several billion degrees are reached. The Iron comes from zones deep in the interior of the star, in which substantial Silicon burning is completed previous to the explosion. Iron is created in a state of nuclear statistical equilibrium with neighboring Iron-peak species. The relative abundances of the Iron isotopes are functions of the temperature, the density, the time scale for the expansion and cooling of the matter as it is ejected into

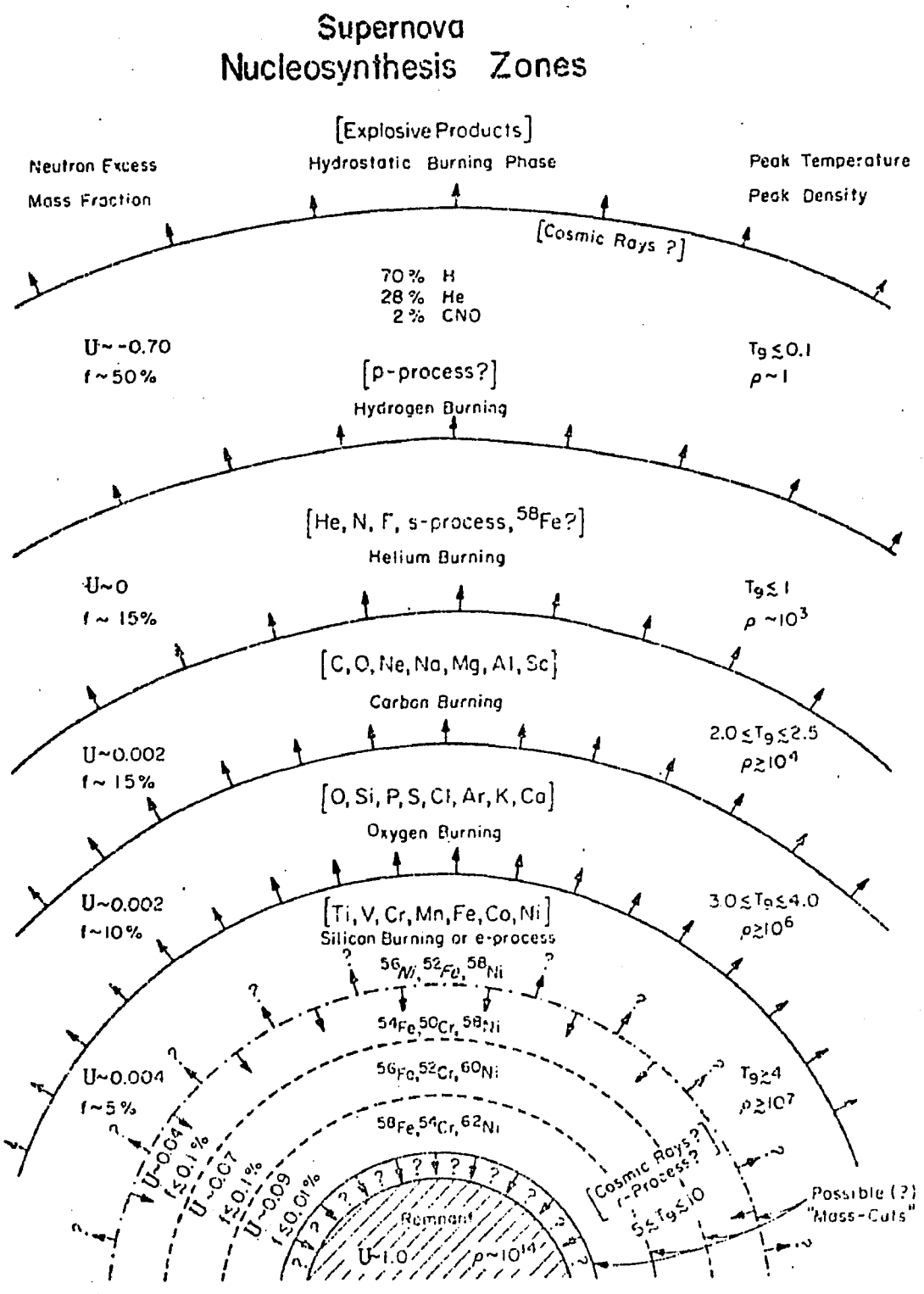

Figure 7.2 Supernova Nucleosynthesis Zones (Woosley, 1975)

the interstellar medium (freeze-out), and the neutron enrichment U of the material. The dependence of the isotopic composition on these parameters is weak with respect to the temperature, density, and freeze-out details, but very strong with respect to the neutron enrichment. The neutron enrichment is defined by:

$$U = \sum_i x_i \left(\frac{N_i - Z_i}{A_i}\right)$$

where:

Xi is the mass fraction of the isotope (Zi, Ai),

Ni is the number of neutrons in the nucleus, and

the sum is over all the species present. It is very important that U is believed to increase monotonically towards the center of the star.

Figure 7.2, from Woosley (1975) shows a likely configuration of a typical supernova just prior to the explosion. It is not important for this discussion to review the ideas regarding the exact mechanism of the collapse and explosion. It is important to see that current theory predicts that the Iron-58 is synthesized only in the last zone in which nuclei are stable. The next zone is the (possible) neutron star remnant. Our observations of Fe-58 in the cosmic rays, in the context of this picture, demand that this very innermost zone of matter be accelerated to

cosmic ray energies.

The detail of information which we can obtain from the Iron observation is very much enhanced by a Figure (also from Woosley, 1975) relating the neutron excess at the site of nucleosynthesis to the ratios of Iron isotopes. Woosley's diagram is reproduced in Figure 7.3, with our observations superimposed. We find a possible explanation of the Fe-58 abundance at a neutron excess of .081+/-.01. Note that because of the strong dependence of the Fe-58 abundance on U, this value is quite accurately known. The source abundance of Fe-54 is small or zero, the small fraction which we observed at the instrument having been lost in the corrections for fragmentation from Fe-56 and Fe-58 in the instrument, the atmosphere and the interstellar medium. The value of U determined above predicts no Fe-54. If Fe-54 is present at all, it must have a <u>different source</u> than the Fe-58.

This last statement is particuarly interesting in light of the paper by Hainebach et al (1974) on the origin of the solar system isotopes in the Iron peak. They find that two different processes are required, one to account for the observed Fe-54, 56, 57, Cr-52, 53, Ni-58, and Mn-55 (U = .0037) and another to account for Fe-58 and Ti-50, Cr-54, V-51, Ni-62 at U = .077.

It is possible to speculate that a substantial portion of the solar Fe-58 may be in fact old cosmic rays, which lost their energy before the solar system was formed, thus enriching the pre-solar interstellar medium in Fe-58. We will not pursue this suggestion further at this point, because it takes us from the topic of cosmic ray composition into the field of nucleocosmochronology.

4.0 CONCLUSIONS

We have discussed a measurement of cosmic ray isotopic composition which has strong implications for theories of cosmic ray origin. Commencing with details of the instrument, and following each step of the data analysis, we have reached the conclusion, which until this point was a popular but unproven hypothesis, that at least part of the cosmic ray nuclei are born in explosive events associated with nucleosynthesis. Further, we have identified the zone from which the Iron component of the cosmic rays comes; it is the innermost zone of the exploding star, with the highest values of neutron enrichment. Much theoretical work must follow on these observations. The implications for cosmic ray acceleration are certain to be large, for now theories must accelerate the material closest to the core of the star. The Sturrock (1971) model of the pulsar mechanism has suggested that material from the surface of the pulsar itself might be accelerated. Models such as that of Scott

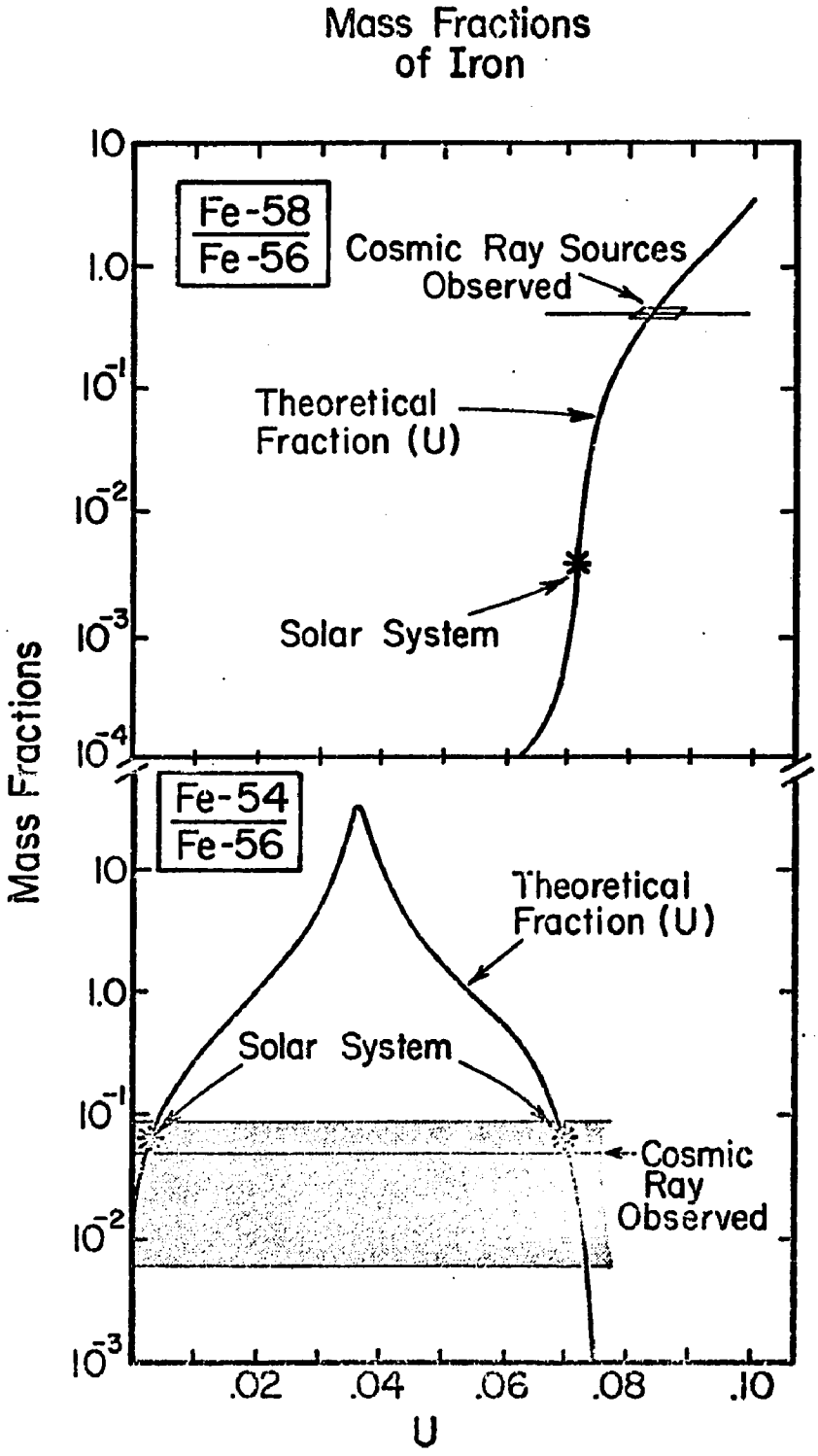

Figure 7.3 Isotopic Fractions of Iron as a Function of Neutron Excess

and Chevalier (1975), which most effectively accelerate material further from the core must show how material from deep within the star can be mixed with that in the outer zones, if they are to remain credible. Our observations indicate that supernovae acceleration mechanisms must be effective in spite of the objections which are currently raised regarding the severe adiabatic deceleration which particles may experience before they escape from the expanding sphere of the supernova remnant (Kulsrud and Zweibel, 1975).

BIBLIOGRAPHY

Arnett, W.D., 1966 Can. J. Phys. 44, 2553.

Arnett, W.D., 1973 in EXPLOSIVE NUCLEOSYNTHESIS, Proc. Conf. Explosive Nucleosynthesis, Austin.

Baade, W., and Zwicky, F., 1934, Phys. Rev. 45, 138.

Bartholma, K.P., Siegman, G., and Enge, W., 1975, Proc. 14th Int. Cosmic Ray Conf. 1, 384

Benegas, J.C., Israel, M.H., Klarmann, J., and Maehl, R.C., 1975, Proc. 14th Int. Cosmic Ray Conf. 1, 251.

Benegas, J.C., Israel, M.H., Klarmann, J., and Maehl, R.C., 1975, Proc. 14th Int. Cosmic Ray Conf. 1, 379.

Burbridge, E. Margaret, Burbridge, G.R., Fowler, William A., and F. Hoyle, 1957, Rev. Mod. Phys. 29, 547.

Burbridge, G.R., 1974, Phil. Trans. R. Soc., Lond.,A 277, 481.

Casse, M., and Goret, P., 1973, Proc. 13th Int. Cosmic Ray Conf.1, 584.

Casse, M., Goret, P., and Cesarsky, C.J., 1975, Proc. 14th Int. Cosmic Ray Conf.2, 646.

Colgate, S.A., and White, R.H., 1965, Ap.J., 143, 626.

Colgate, S.A., 1973, "Supernova Shock Waves", preprint.

Cowsik, R., Pal, Yash, Tandon, S.N., and Verma, R.P., 1965, Phys. Rev., 158, 1238.

Cowsik, R., and Wilson, Lance W., 1975, Proc. 14th Int. Cosmic Ray Conf. 2, 475.

Dwyer, Robert, and Meyer, Peter, 1976, APS Conference, Washington, D.C.

Fan, C.Y., Gloeckler, G., and Simpson, J.A., 1966, Phys. Rev. Lett. 17, 329.

Fermi, E. 1949, Phys. Rev. 75, 1169.

Fermi, E. 1954, Ap.J., 119, 1.

Fichtel, C.E., Hartman, R.C., Kniffen, D.A., Thompson, D.J., Bignami, G.F., Ogelman, H., Ozel, M.E., and Tumer, T., 1975, Ap.J., 198, 163.

Fisher, A.J., Hagen, F.A., Maehl, F., and Ormes, J.F., 1975, Proc. 14th Int. Cosmic Ray Conf., 1, 373.

Fowler, W.A., 1975, Proc. 14th Int. Cosmic Ray Conf. 11, 3550.

Garcia-Munoz, M., Mason, G.M., and Simpson, J.A., 1975, Proc. 14th Int. Cosmic Ray Conf. 1, 331.

Garcia-Munoz, M., Mason, G.M., and Simpson, J.A., 1977, Proc. 15th Int. Cosmic Ray Conf. 1, 224.

Ginzburg, V.L., and Syrovatskii, S.I., 1964, The Origin of Cosmic Rays, Pergamon Press, New York.

Gleesen, L.J., and Axford, W.I., 1968, Ap.J., 154, 1011.

Hainebach, K.L., Schramm, D.N., and Arnett, W.D., 1975, Proc. 14th Int. Cosmic Ray Conf. 2, 488.

Hagen, F.A., Fisher, A.J., Ormes, J.F., and Arens, J.F., 1975, Proc. 14th Int. Cosmic Ray Conf. 1, 361.

Hartman, R.C., Fichtel, C.E., Kniffen, D.A., Lamb, R.C., Thompson, D.J., Bignami, G.F., Ogelman, H., Ozel, M., and Tumer, T., 1976, in THE STRUCTURE AND CONTENT OF THE GALAXY AND GALACTIC GAMMA RAYS, Goddard Space Flight Center.

Henke, R.P., and Eaton, E.V., 1975, Proc. 14th Int. Cosmic Ray Conf. 1, 395.

Heristchi, D.J., 1967, Nuc. Inst. Meth. 47, 39.

Hiltner, W.A., 1956, Ap.J., Suppl., 2, 389.

Iben, I., 1968, ApJ., 193, 157.

Jokipii, J.R., and Lerche, I., 1969a, Ap.J., 157, 1137.

Jokipii, J.R., Lerche, I., and Schammer, R.,A., 1969b, Ap.J., Lett, 157, L119.

Jokipii, J.R., 1973, Comments Astrophys. Space Sci., 5, 125.

Jones, Frank C., 1970, Phys. Rev. D., 2, Number 12, 2787.

Julliot, C., Koch, L., and Petrou, N., 1975, Proc. 14th Int. Cosmic Ray Conf. 12, 4118.

Juliusson, Einer, 1975, Proc. 14th Int. Cosmic Ray Conf. 1, 355.

Kulsrud, Russel, and Zwiebel, Ellen, 1975, Proc. 14th Int. Cosmic RayConf. 2, 465.

Lamb, R.C., and Pethik, C.J., 1976, Ap.J. Lett., 209, 77.

Lezniak, J.A., 1975, Nuc. Inst. Meth., 126, 129.

Lezniak, J.A., 1976, Nuc. Inst. Meth. 136, 299.

Lindstrom, P.J., Greiner, D.E., Heckman, H.H., Cork, B., and Beiser, F.S., 1975, preprint, CBL-3650.

Maehl, R., Hagen, F.A., Fisher, A.J., Ormes, J.F., and Simon, M., 1975, Proc. 14th Int. Cosmic Ray Conf. 1, 367.

Manchester, R.N., 1972, Ap.J., 172, 43.

Meyer, Peter, Ramaty, Reuven, and Webber, William R., 1974, Physics Today, 27, Number 10.

Ormes, J.F., Fisher, A., Hagen, F., Maehl, R., and Arens, J.F., 1975, Proc. 14th Int. Cosmic Ray Conf. 1, 245.

Ostriker, J.P., and Gunn, J.E., 1969, Ap.J., 157, 1395.

Ostriker, J.P., and Gunn, J.E., 1970, Ap.J., 160, 979.

Ostriker, J.P., and Gunn, J.E., 1971a, Ap.J., 164, L95.

Ostriker, J.P., and Gunn, J.E., 1971b, Ap.J., 165, 523.

Owens, A.J., 1975, Proc. 14th Int. Cosmic Ray Conf. 2, 678.

Parker, E.N., 1965, Ap.J., 142, 584.

Parker, E.N., 1973b, Astrophys. Space Sci., 24, 279.

Parker, E.N., 1975, Ap.J., 202, 523.

Pasczynski, B., 1971, Acta. Astr., 21, 1.

Perron, Claude, 1975, Thesis, Centre d'Orsay, Universite Paris-Sud.

Preszler, A.M., Kish, J.C., Lezniak, J.A., Simpson, G., and Webber, W.R., 1975, Proc. 14th Int. Cosmic Ray Conf. 1, 243.

Reeves, Hubert, 1968, Stellar Evolution, Gordon and Breach, New York.

Richtmeyer, R.D., and Teller, E., 1949, Phys. Rev. 75, 1729.

Scott, John S., and Chevalier, Roger, A., 1975, Ap.J., 197, L5.

Shapiro, M.M., and Silverberg, R., 1975, Proc. 14th Int. Cosmic Ray Conf. 2, 538.

Silverberg, R., and Tsao, C.H., 1973, Ap. J. Suppl., 25, 315.

Silverberg, R., Tsao, C.H., and Shapiro, M.M., 1976, in SPALLATION NUCLEAR REACTIONS AND THEIR APPLICATIONS, Ed. Shen/Merker.

Soutoul, A., Casse, M., and Julliusson, E., 1975, Proc. 14th Int. Cosmic Ray Conf. 2, 455.

Stecker, F.W., 1975, Phys. Rev. Lett. 35, Number 3, 188.

Sturrock, P.A., 1971, Ap. J. 164, 529.

Webber, W.R., Damle, S.V., and Kish, J., 1972, Astrophys. Space Sci. 15, 245.

Webber, W.R., Lezniak, J.A., and Kish, J., 1973a, Ap. J. 183, L81.

Webber, W.R., Lezniak, J.A., Kish, J., and Damle, S.V., 1973, Ap. Space Sci. 24.

Webber, W.R., Lezniak, J.A., Kish, J.C., and Simpson, G.A., 1977, Astrophys. Lett., in press.

Webber, W.R., Lezniak, J.A., 1974, Durham Symposium on Cosmic Ray Isotopic Composition.

Wheeler, J. Craig, 1973, in Explosive Nucleosynthesis, Conf. Expl. Nucl., Austin.

Woosley, S.E., 1975, "Importance of Isotopic Composition of Iron in Cosmic Rays," Orange Aid Preprint Series, Caltech.

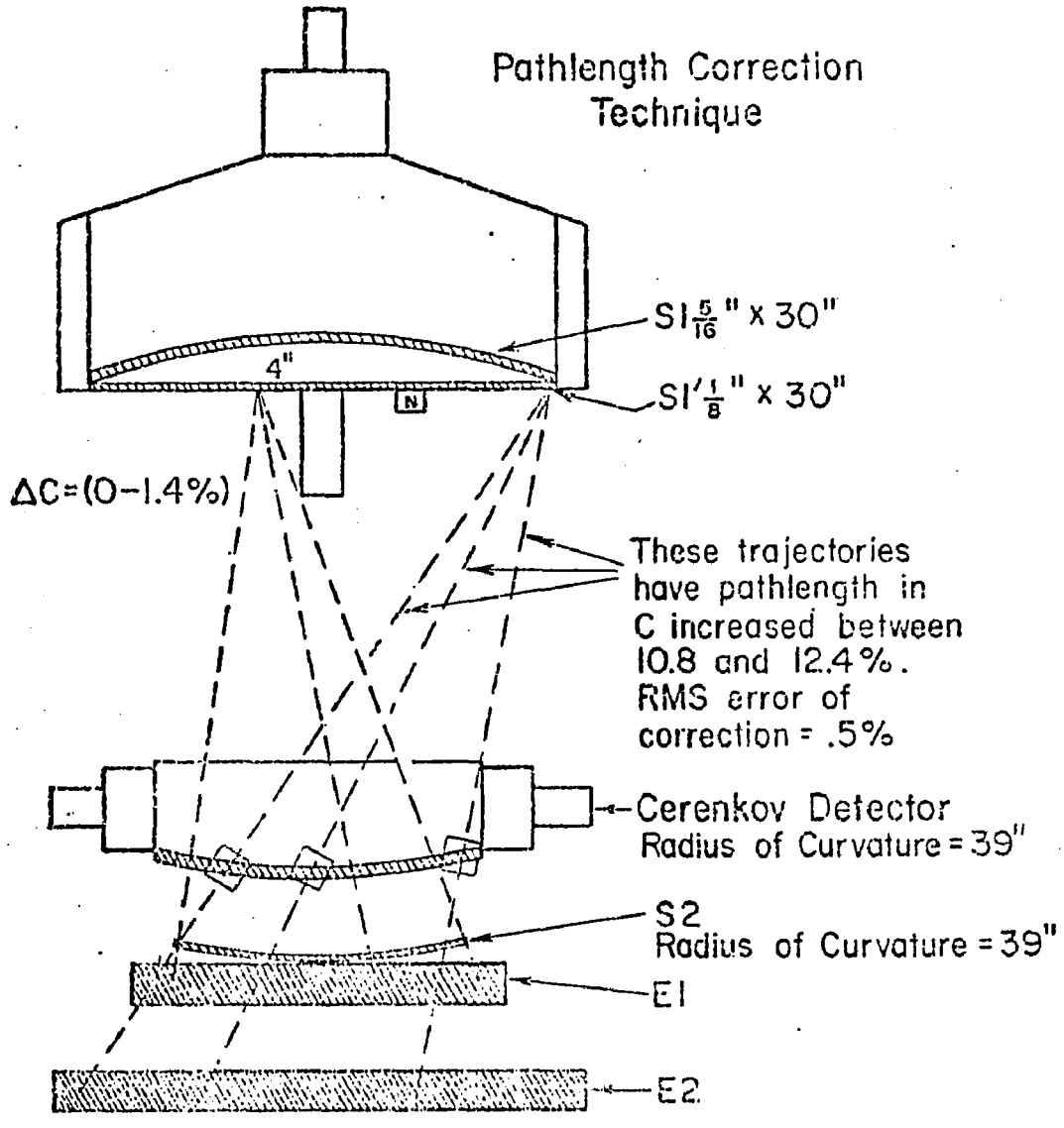

Figure A1.1 Pathlength Correction Technique

APPENDIX 1

PATHLENGTH CORRECTION TECHNIQUE

1.0 INTRODUCTION

The central problem of counter design for cosmic ray composition studies is that of combining large geometrical collecting power with high resolution detectors. One important source of resolution broadening is "pathlength errors" which are the variations in the energy deposited in any penetrated detector caused by the secant (e) increase of pathlength, where (e) represents the angle between the particle trajectory and the perpendicular to the detector surface. This increase has the two-fold effect of increasing the output of the detector traversed, and decreasing the energy with which the particle enters the following detectors. The combination of suitably curved detectors with a radius measurement at the opposite end of the telescope is a simple and powerful technique for removing pathlength errors.

The principle of the method is seen in Figure A1.1. It may be seen from this Figure that particles which pass through the S1 and S1' detectors at any radius from the instrument axis may take a variety of trajectories through

the C detector, and that these trajectories may be inclined with respect to the normal to the C-detector surface, thus giving an increase of pathlength, and therefore signal, from the detector. The crux of the pathlength correction technique is that if the radius of the particle from the axis at S1' is known, and if the curvature of the C detector is chosen appropriately, then all trajectories through any fixed S1' radius have very similar angles with respect to the C-detector surface. As we note on Figure A1.1, particles passing near the maximum radius of S1 and S1' have pathlength errors of from 10.8 to 12.4 %. Therefore knowledge of the particle radius in S1' may be used to remove the majority of the pathlength errors in C. As a further step, the decrease of energy loss in the detector in which the particle stops, due to the increase of pathlength through the detectors above it, may be computed and corrected for.

The principle of the radial information system is also quite simple: The thin scintillator S1' has a 2" photomultiplier optically coupled to its center, and is situated as close as possible to S1. It is painted on the edge and wrapped with foil in such a way that it has a fall-off of pulse height with radius of about 15%/inch. The pulse height in S1' is therefore a function of scintillator output and radius. The adjoining counter S1 has had all the spatial non-uniformities removed, by compensation. Therefore the ratio S1/S1' may be used as the argument of a

function to give the radius, and thus the pathlength correction.

In the following sections of this Appendix, we discuss the geometry of the pathlength correction for detectors which are penetrated, the corrections to detectors in which the particle stops, and the technique used for establishing the radial scale. We conclude the last section with a discussion of the net pathlength error which results from the combined effects of errors in the radial measurement and intrinsic errors in the pathlength correction technique.

2.0 CORRECTION TO PENETRATED DETECTORS

Assuming that the radius of a particle is known precisely in one curved detector, we may study the pathlength effects in penetrated detectors at the opposite end of the telescope using elementary geometry. Refer to Figure A1.2.

To calculate the pathlength error in the bottom detector in this Figure, the angle(e) may be determined as follows.

Let:

e= the angle from the particle trajectory to the perpendicular to the detector surface

$\underline{X}, \underline{Y}, \underline{Z}$= unit vectors in the radial, transverse, and axial directions

$\underline{R}$= unit vector along Cr

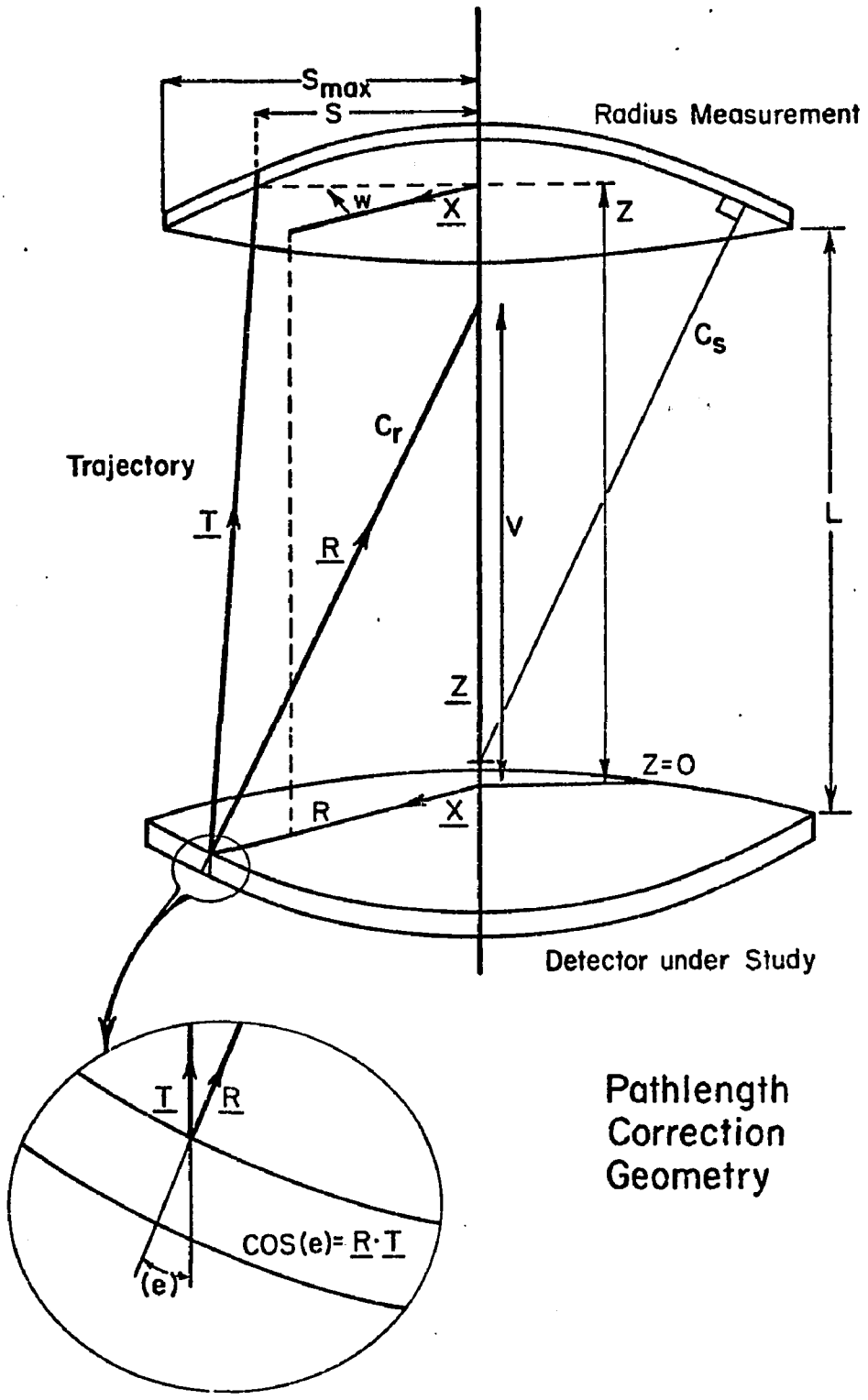

Figure A1.2 Pathlength Correction Geometry

$\underline{T}$= unit vector along trajectory

S= trajectory radius in radius detector

Cs= radius of curvature of radius detector

Smax= max radius of radius detector

L= minimum detector separation

R= trajectory radius in detector studied

Cr= radius of curvature of detector studied

Rmax= maximum radius of detector studied

w= azimuth of trajectory intersection with detector studied relative to intersection with radius detector

Z= $\underline{z}$-separation of intersections of trajectory with detectors.

Then:

$$\cos(e)=\underline{R}\cdot\underline{T}$$

And the fractional pathlength increase 'P' is given by

$$P \leq \left(1-\frac{1}{\underline{R}\cdot\underline{T}}\right)^{-1}$$

Equality represents the approximation that the detector is flat in the region of the trajectory. This is strictly valid only for zero thickness detectors, but the departure from validity is of the order of the fractional correction squared.

The coordinates of the trajectory intersection with the detector studied are defined as (R,0,0) , while the intersection with the radius detector is

$$(S\cos(w), S\sin(w), Z).$$

CERENKOV DETECTOR PATHLENGTH CORRECTIONS

S1' RADIUS	P%	% RMS ERROR	MAX(P)-MIN(P)
0.000	0.091	0.052	0.162
2.000	0.294	0.203	0.737
4.000	0.887	0.386	1.446
6.000	1.881	0.511	1.910
8.000	3.329	0.611	2.296
10.000	5.103	0.702	2.608
12.000	7.382	0.683	2.493
14.000	10.131	0.581	2.064

Table A1.1 Cerenkov Detector Pathlength Corrections

S2 DETECTOR PATHLENGTH CORRECTIONS

S1' RADIUS	P%	% RMS ERROR	MAX(P)-MIN(P)
0.000	0.019	0.011	0.034
3.000	0.369	0.106	0.399
6.000	1.424	0.171	0.632
9.000	3.177	0.158	0.573
12.000	5.617	0.110	0.348
15.000	8.726	0.313	1.245

Table A1.2 S2 Detector Pathlength Corrections

Then:

$$\underline{R} = (R\underline{x} + V\underline{z})/(R^2 + V^2)^{\frac{1}{2}}$$

$$\underline{T} = \frac{(R - S\cos w)\underline{x} - S\sin w\,\underline{y} + Z\underline{z}}{(R^2 + S^2 - 2RS\cos w + Z^2)^{\frac{1}{2}}}$$

$$R \cdot T = \frac{(R^2 - RS\cos w + VZ)}{\{(R^2 + S^2 - 2RS\cos w + Z^2)(R^2 + V^2)\}^{\frac{1}{2}}}$$

where

$$Z = L + (C_s^2 - S^2)^{\frac{1}{2}} + (Cr^2 - R^2)^{\frac{1}{2}} - (C_s^2 - S_{max}^2)^{\frac{1}{2}} - (Cr^2 - R_{max}^2)^{\frac{1}{2}}$$

$$V = (C_r^2 - R^2)^{\frac{1}{2}}$$

The mean pathlength errors are determined as a function of radius in the radial measurement detector by numerically averaging over the area of the detector studied, weighting each differential element of the numerical integral with the geometrical factor appropriate to it (Heristchi, 1967). An analysis of the Cerenkov detector C is shown in Table A1.1 below. The first column gives radius in S1', the second gives the fractional pathlength error 'P', the third gives the root-mean square deviation of 'P', and the fourth gives the difference between the extreme values of 'P'. It can be seen that perfect knowledge of the radius in the radial measurement detector would allow reduction of the pathlength errors in C from a mean of 5.5% to less than 0.7%, which is well below the estimated error from other sources.

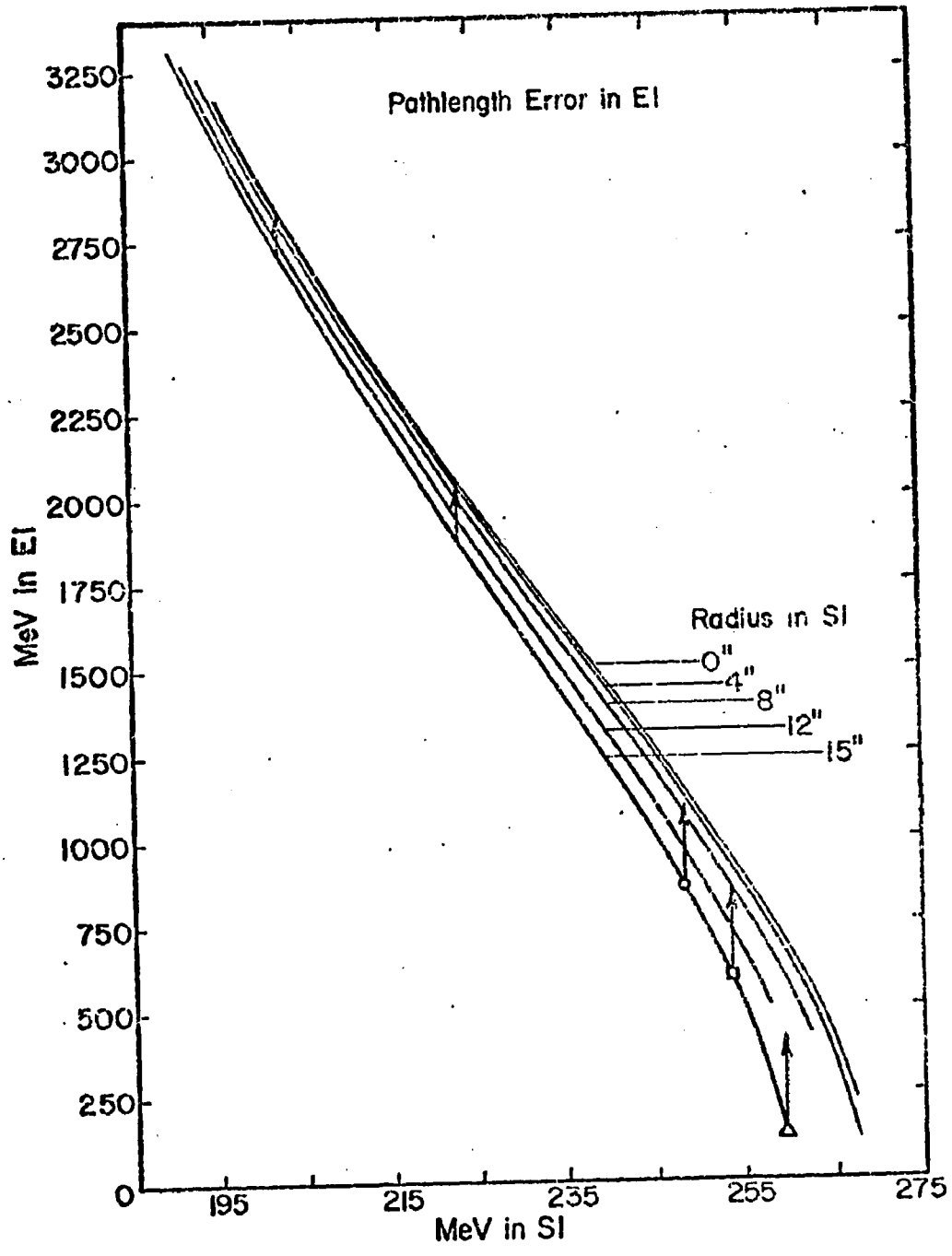

Figure A1.3 Pathlength Error in E1

Similarly, pathlength errors in the S2 counter can in principle be corrected to 0.5%, as we may see from Table A1.2.

3.0 CORRECTIONS TO STOPPING DETECTORS

The effect of an increase in pathlength in the detectors above the one in which the particle stops is to decrease the energy loss in the stopping detector. This effect can be corrected for in a simple manner, by increasing the pulse from the stopping detector proportionately to the pathlength correction applied to the detectors which are penetrated.

To study the relationship between the correction to the stopping counters and that to the penetrated counters, we first construct Figure A1.3 from energy loss calculations. We have assumed a series of radii in S1', as indicated in the Figure. For each radius in S1' the thickness of the subsequent elements of the telescope is increased by the average pathlength error calculated for each S1' radius. This Figure shows the average energy deposited in E1 and S1 by Oxygen-16 nuclei which stop in E1. The S1 detector curvature is chosen to minimize the overall pathlength errors in it, and for a given particle energy, the S1 energy deposit is independent of radius. Therefore this figure in effect gives a measure of the pathlength error in E1 as a function of S1 radius and E1 energy deposit. We may

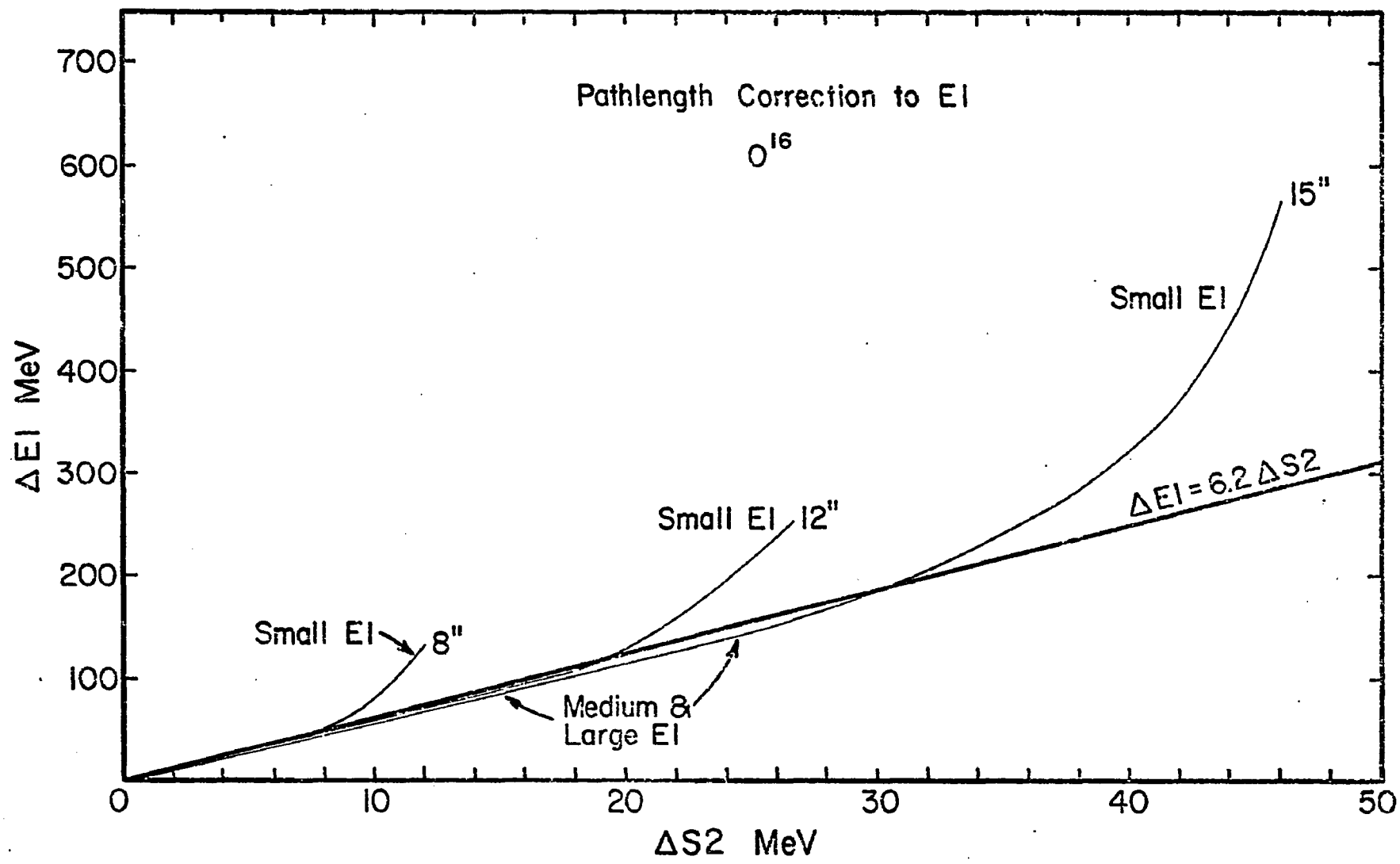

Figure A1.4 Pathlength Correction to E1

determine this error for any S1 radius from the figure; it is the difference between the curve at 0" and that at the radius considered, at constant S1.

The next step in this analysis is to find a convenient method of expressing this error, which is valid for all nuclei. A logical choice of parameter to correlate with the E1 pathlength error is the pathlength error in S2, since these two quantities are physically related, as we have discussed. The correlation of the E1 pathlength error with that in S2 is shown in Figure A1.4. The curves on this graph show that at all S1 radii, the increase of energy deposit in S2 due to pathlength errors is well-correlated with the decrease of energy deposit in E1, except for the smallest energy deposits in E1. Therefore if we make the linear correlation shown in A1.4, E1 will be corrected as shown by the arrows on Figure A1.3. A survey of other nuclei has proved that the correlation function shown in Figure A1.4 is adequate for all cases.

The case of particles stopping in the E2 counter is handled in a similar fashion, but the correction is not as well determined, because E1 is flat, and therefore the pathlength errors in E1 are much larger. Note that although the pathlength correction to E2 due to variations of (e) in E1 is not well defined, that in the sum E1+E2 is known to high accuracy, being only due to the well defined pathlength variations in (e) through S2 and C. This is the reason for

the use of this sum in the data analysis for particles stopping in E2.

4.0 RADIAL MEASUREMENT DETECTOR

4.1 RADIAL SCALE

Three pieces of information are used to establish the relationship between the ratio S1/S1' and the radius. these are:

1. The response of S1' to a localized beam of electrons of fixed energy. This response, as a function of S1' radius, was measured before and after the flight, giving the empirical relationship:

$$\ln S1' = A - kR$$

where K and A are constants, and R is the radius.

2. Particles which trigger the S1' normalization detector 'N' give a calibration point at 3.5 inches.

3. The peak of the S1' pulse-height distribution of all v=1 particles of each charge. We have assumed that this point corresponds to a radius of 12.5 inches, for all charges. This assumption is verified by first calculating the expected pulse height distributions in S1' for a variety of detector resolutions. These distributions represent convolutions of the distribution of differential geometry (as a function of S1' radius)

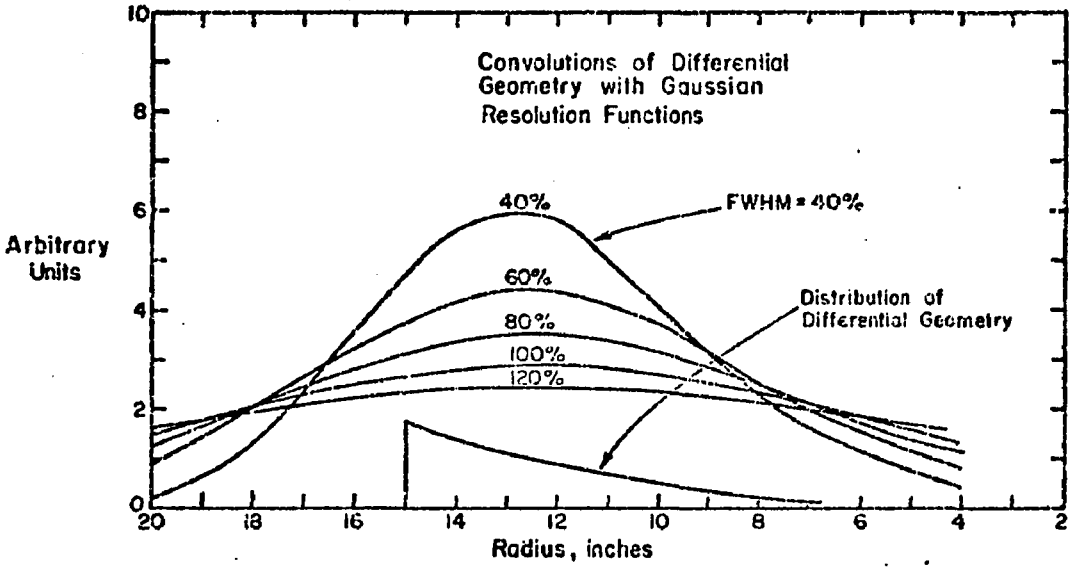

Figure A1.5

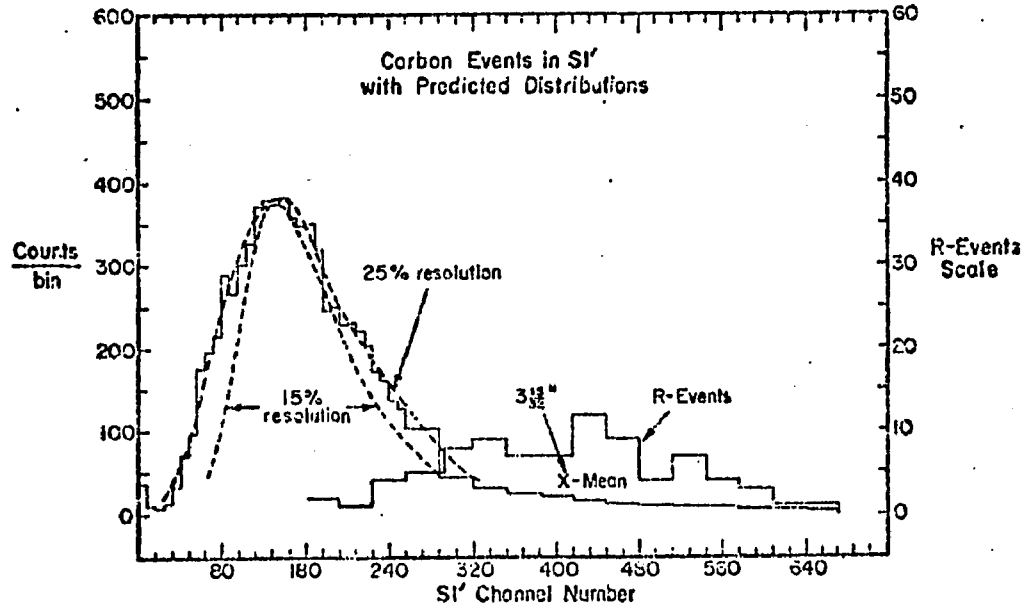

Figure A1.6

with the resolution of the radial detector. These distributions are shown in Figure A1.5. It is seen from this Figure that, independent of S1' resolution, the peak of the distribution corresponds to 12.5". Thus we have two points with which to establish the radial measurement scale, along with an experimentally measured radial fall-off function. To verify that the convolutions provide a reasonable representation of the data, we show in Figure A1.6 the measured distribution of Carbon events, and the calculated distributions (converted to pulse-height scale).

4.2 SATURATION OF S1'

Figure A1.7 is a logarithmic plot of S1' channel versus S1 channel, showing the N-events (3.5") and the S1' distribution peaks(12.5") separately, for each available charge. The slope of these two curves should be one for proportionality to hold between S1 and S1'. What is seen instead is that as S1' increases, the ratio S1/S1' becomes slightly larger. This unexpected behavior may be explained if saturation of the output of S1' relative to S1 is invoked. Modelling this saturation effect by

$$S1'_{saturated} = \left(\frac{S1'}{1+S1'/a}\right)$$

with a=4817, the observed nonlinear behavior is removed. (This nonlinearity fit implies that the observed Iron

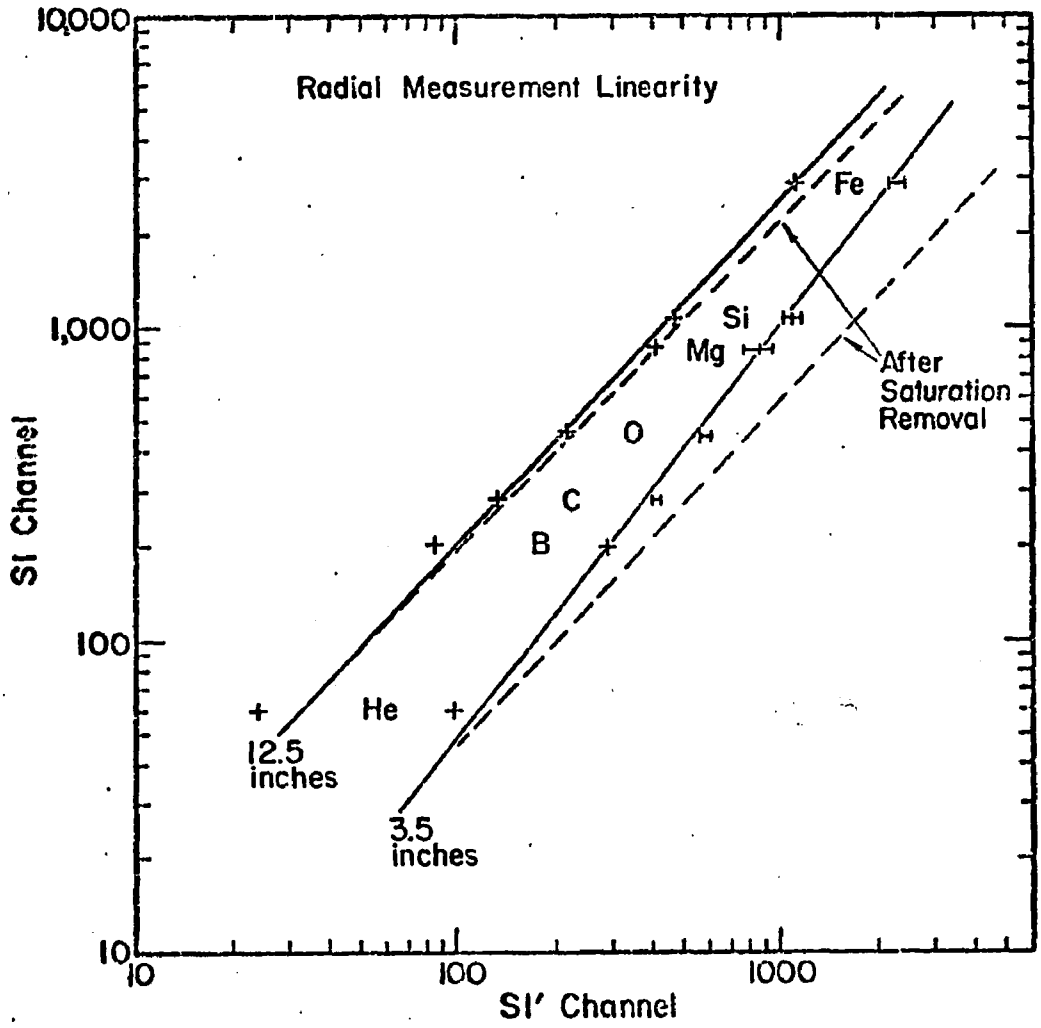

Figure A1.7 Radial Measurement Linearity

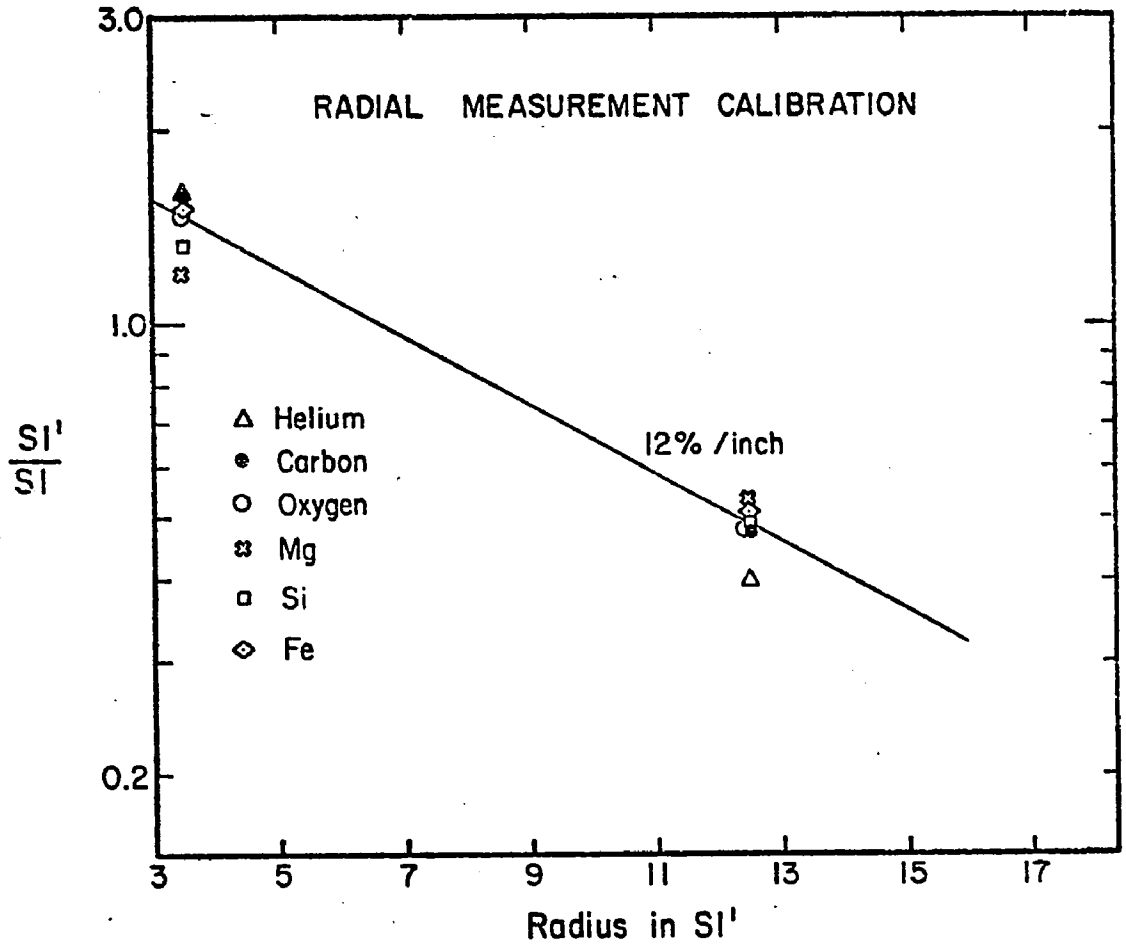

Figure A1.8 Radial Measurement Calibration

N-events at channel 2300 should have been in channel 4400.) The source of the non-linearity was almost certainly electronic, probably in the S1' photomultiplier, which was run at very high gain in order to achieve sensitivity to the small pulse heights related to events at large radii.

4.3 RADIAL SCALE AND TOTAL PATHLENGTH ERRORS

Using information on the pulse height of all the charges mentioned above, the preflight calibration, and including the effects of S1' saturation, we have constructed the radial measurement calibration curve shown in Figure A1.8. This calibration curve is used to find the S1' radius of each event, and thus to determine the pathlength correction to apply. The complete pathlength correction algorithm is shown in Figure A1.9.

Using this radial calibration, we may estimate the intrinsic resolution of the radial counter. This estimate is made by making a convolution of differential geometry in S1' with sample Gaussian resolution functions to derive predicted pulse height distributions in S1'. We can estimate the S1' resolution as a function of charge, by comparing the predicted distributions with observed pulse-height distributions. A sample was shown in Figure A1.6 for Carbon. We find that the limiting resolution of the S1' counter for Carbon and all heavier nuclei is 23%.

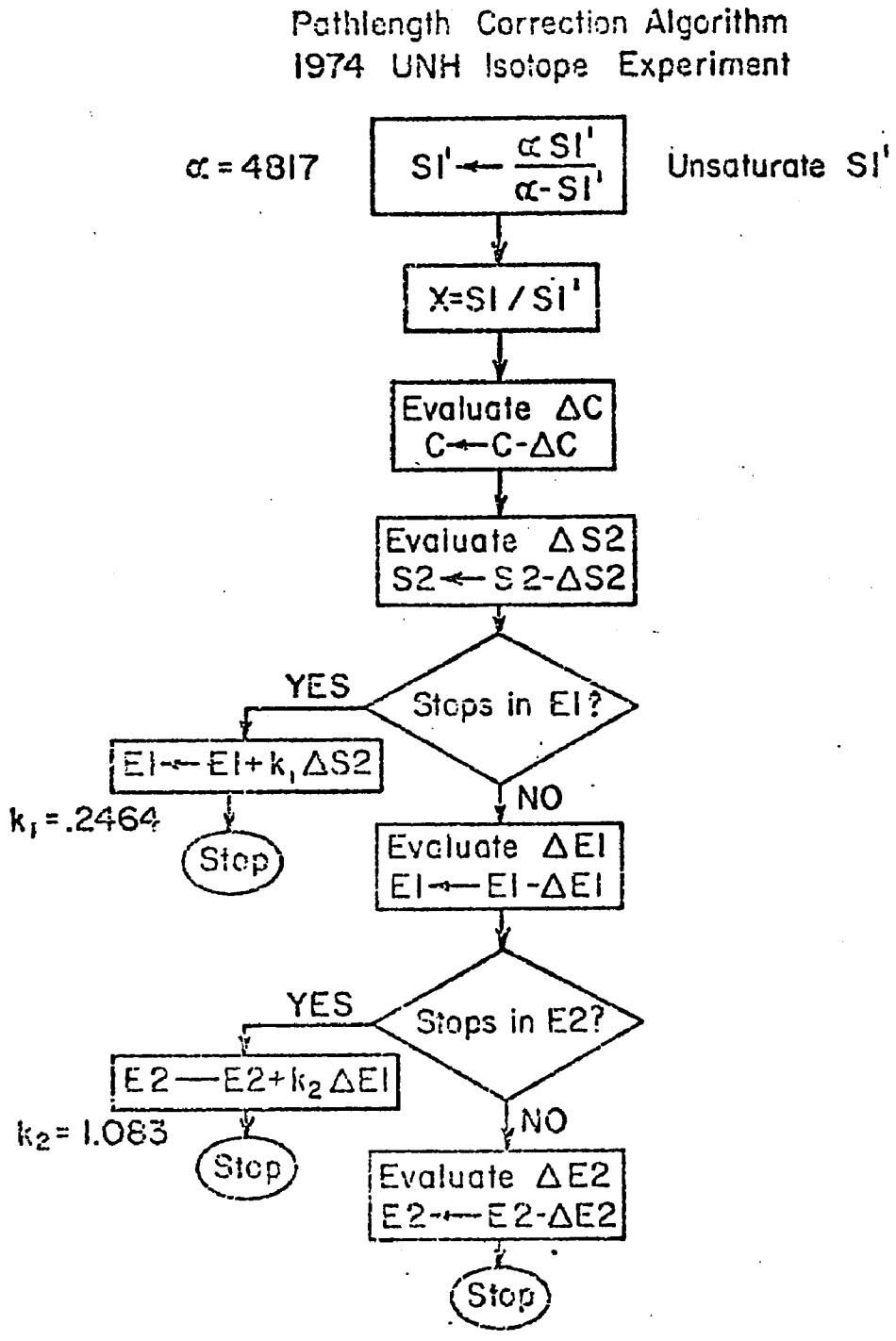

Figure A1.9 Pathlength Correction Algorithm

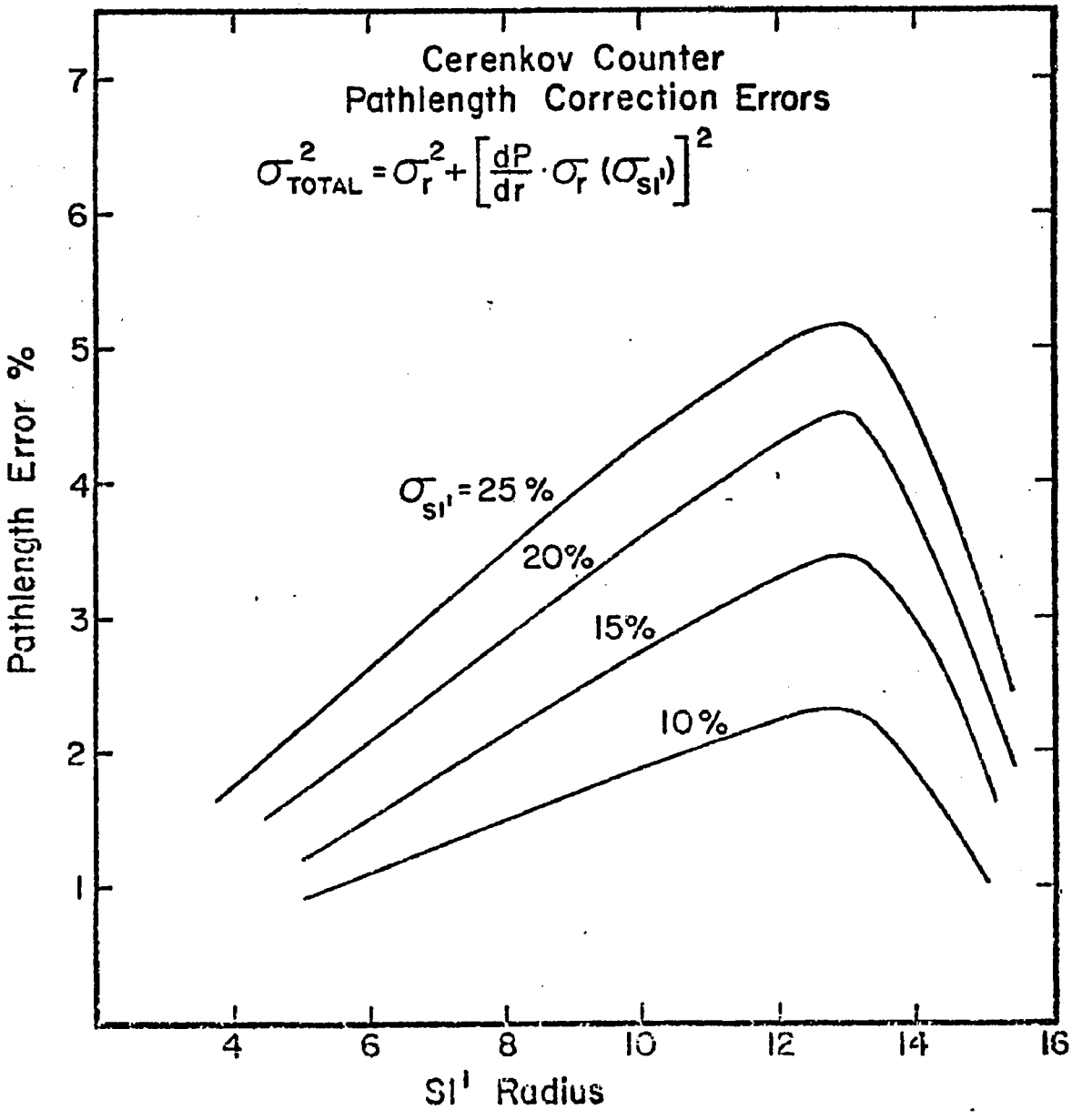

Figure A1.10 Cerenkov Counter Pathlength Correction Errors

The total pathlength contribution to the resolution of pathlength corrected detectors has two components. One, which we call the residual error (Qres), is the pathlength error which remains even if the radial measurement is perfect. This error is shown, for example, in Table A1.1, column 3. The second component, which is due to the error in the radial measurement, may be expressed as the product of the radial measurement error (which is a function of the S1' resolution) and the rate of change of pathlength correction (P) with respect to radius (dP/dr). The quadratic sum of these components is seen plotted versus S1' radius in Figure A1.10, with detector resolution as a parameter. The pathlength error is seen to increase with radius to a peak at a radius of about 13". For a 23% S1' resolution this peak error is about 5%, and the mean error is estimated to be 4%.

APPENDIX 2

DATA ANALYSIS DETAILS

This Appendix is written to document some details of the data collection and analysis procedures.

1.0 DATA COLLECTION DURING THE BALLOON FLIGHTS

The instrument was flown three times in the summer of 1974. On July 21 and August 3 it was flown from Churchill, Manitoba, and on September 22, it flew from Sioux Falls, South Dakota. For each of these flights, the instrument was carefully adjusted before the launch. Minimum ionizing Z=2 particles were simulated in the pre-flight tests by using muons with X4 amplifiers, to set thresholds on the telescope coincidence elements S1 and S2 which rejected all penetrating protons, while allowing helium nuclei to trigger the instrument. The thresholds were set at channel 15, while the gains of S1 and S2 were adjusted so that minimum ionizing helium would be in channel 30. 12-bit (4096 channel) ADC'S were used for each counter analyzed (S1, S1', Gas1, Gas2, C, S2, E1, E2, PEN). For the Churchill flights, the gas detector was not flown.

Figure A2.1 shows the geographic trajectories of the flights, and altitude profiles are seen in Figure A2.2. For the Churchill flights, both P and L-band transmitters were

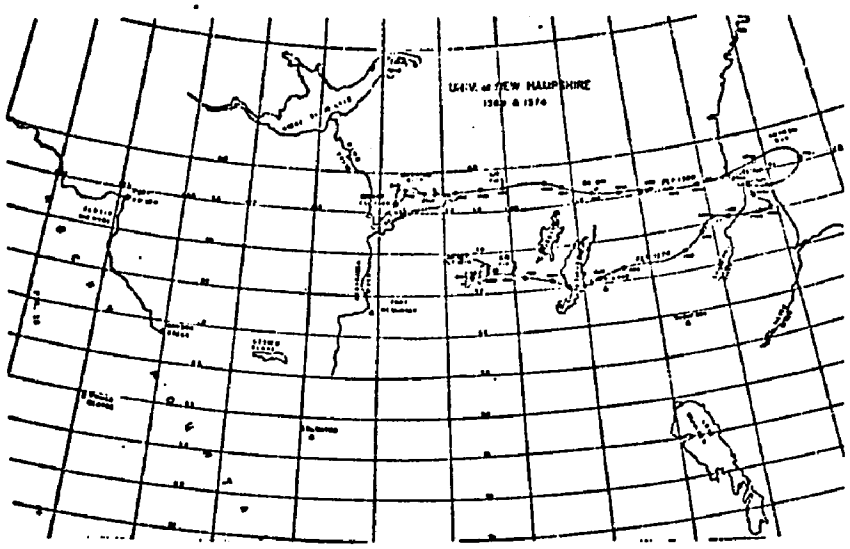

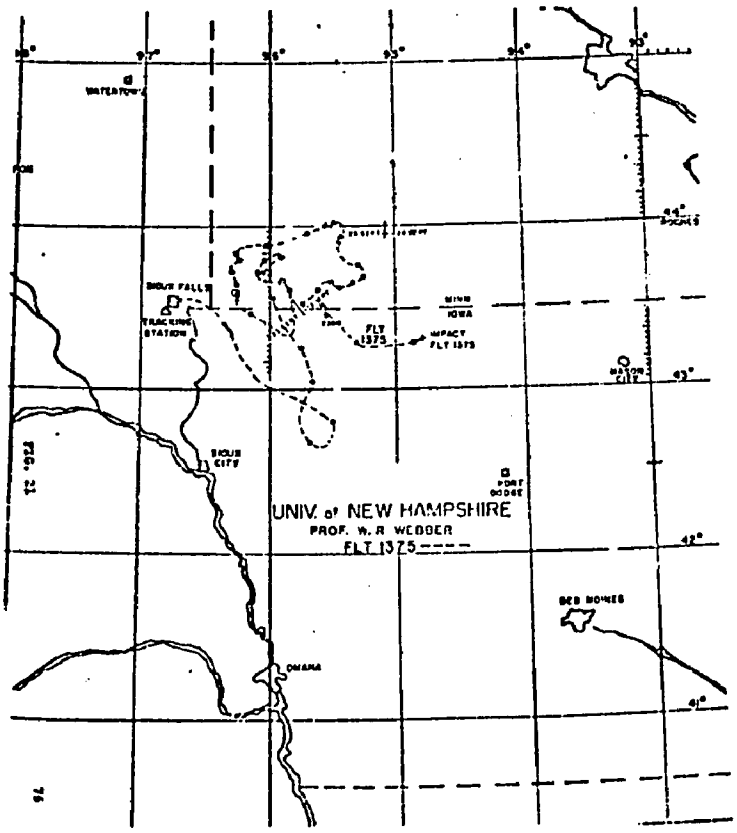

Figure A2.1 Geographic Trajectories

Churchill 'A' Flight

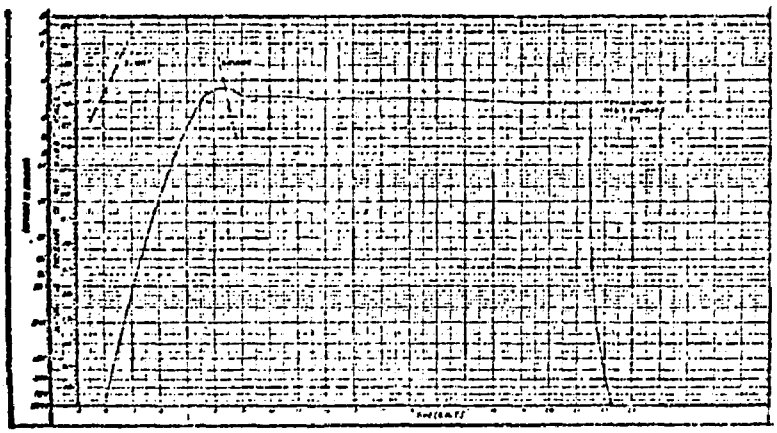

Churchill 'B' Flight

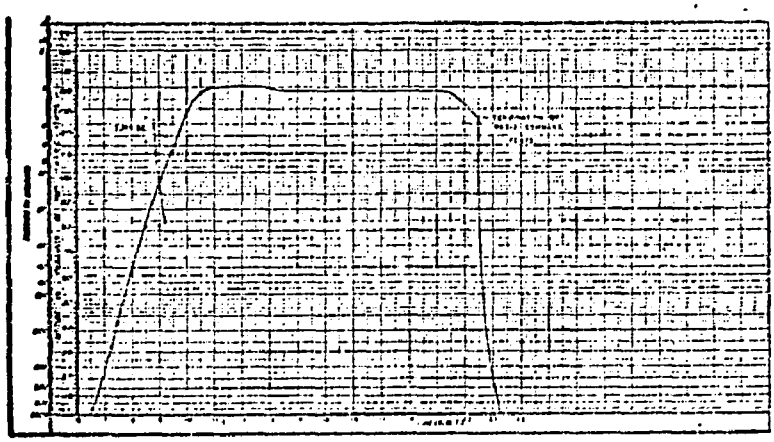

Sioux Falls Flight

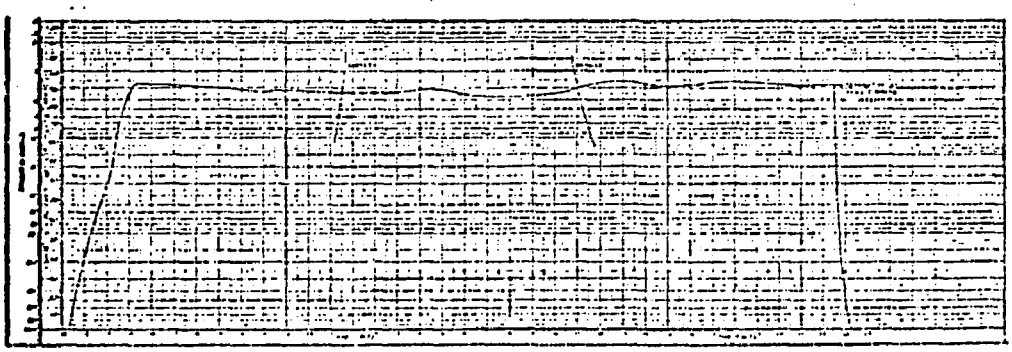

Figure A2.2 - Altitude Profiles

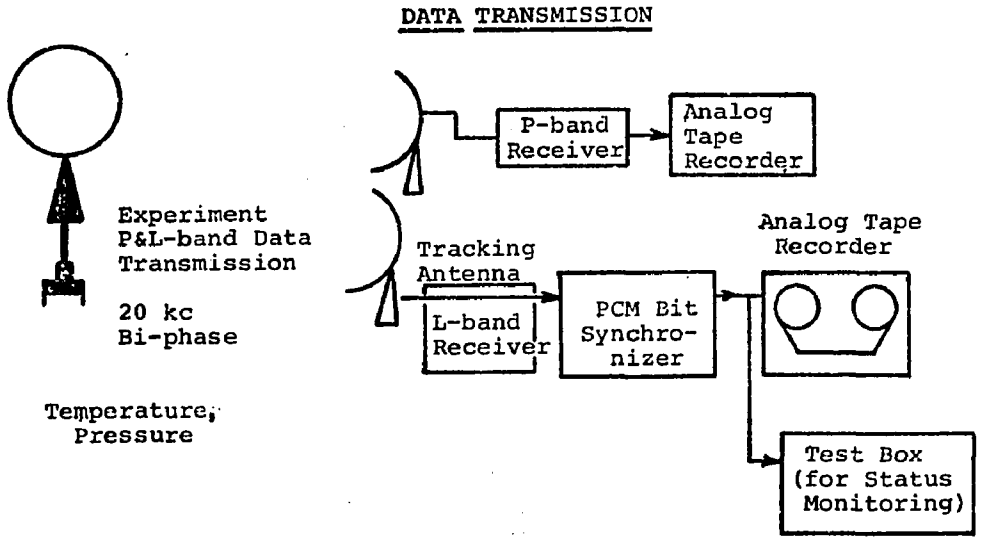

Figure A2.3 Data Transmission

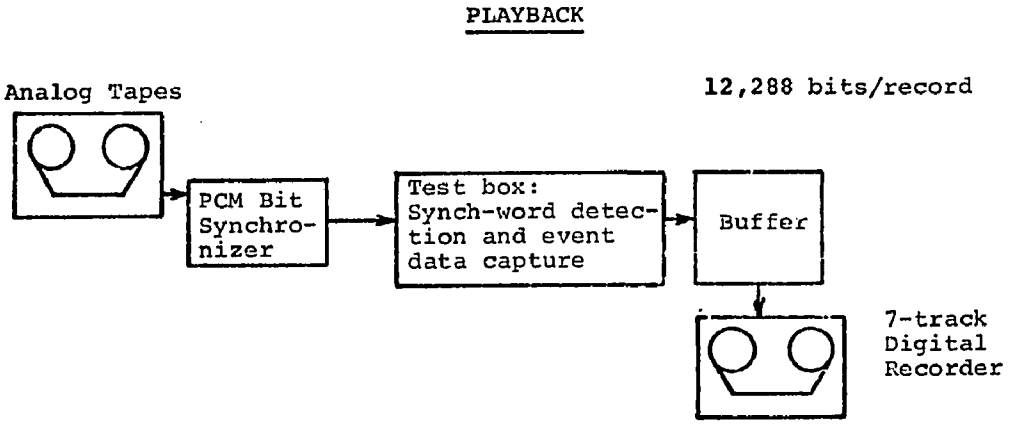

Figure A2.4 Playback Configuration

used, and the data was recorded at 20Kcs on wide-band video equipment, as seen in Figure A2.3. The telemetry mode was bi-phase, with a repeated one-zero bit pattern maintained between events, which enhanced the experiment's noise rejection capability. The use of a PCM bit synchronizer greatly aided the extraction of the signal from the background noise during time periods when the signal was weak. For the Sioux Falls flight, due to FCC regulations, P-band coverage was not available, but otherwise the situation was the same. For the first flight, downrange tracking was used, but this was not necessary for the later flights. Good data were obtained for a total of 28.4 hours at float from the three flights, for a net collection factor of 8450 square m-ster-sec.

2.0 PLAYBACK OF FLIGHT DATA

The playback configuration is diagrammed in Figure A2.4. The flight data was in the form of video tape (analog) records of the signal received by the ground stations. During playback, the signal is scanned for the 6-bit synch pattern which signals transmission of an event. This pattern initiates the placing of the event data into a record of information for output to a computer tape. The extraction of data from the video tapes was facilitated by the use of the bit synchronizer again, which by maintaining a high degree of phase synchronization with the incoming

signal, is able to reject spurious frequency components, thus greatly enhancing the signal-to-noise ratio. An alternate mode of playback operation, which was used for the Churchill 'B' and the Sioux Falls flights, ignored the synch information and put all the data, including the one-zero pattern onto the computer tape. This allowed computer scanning of the bits between events to eliminate noisy sections of data.

3.0 TEMPERATURE CORRECTIONS

During the ascent, balloon experiments encounter ambient temperatures from -70 degrees to +70 degrees F . The experiment was wrapped in 4 inches polyurethane foam insulation, and (after the first flight) carried two heavy duty batteries driving resistive heaters, to moderate the temperature extremes. Even so, it was important to carefully remove temperature effects in each detector caused by the variation of temperature inside the package from 30 degrees F to 80 degrees F. This was done by determing, for successive one hour intervals, the pulse amplitudes of minimum ionizing (or v=1) B, C, O, Mg, and Fe nuclei which penetrate the instrument without slowing down appreciably: Matrices of C x (det) (where (det) is each of S1, S2, E1, and E2) were generated for each hour of flight data, using a simple four-detector consistency

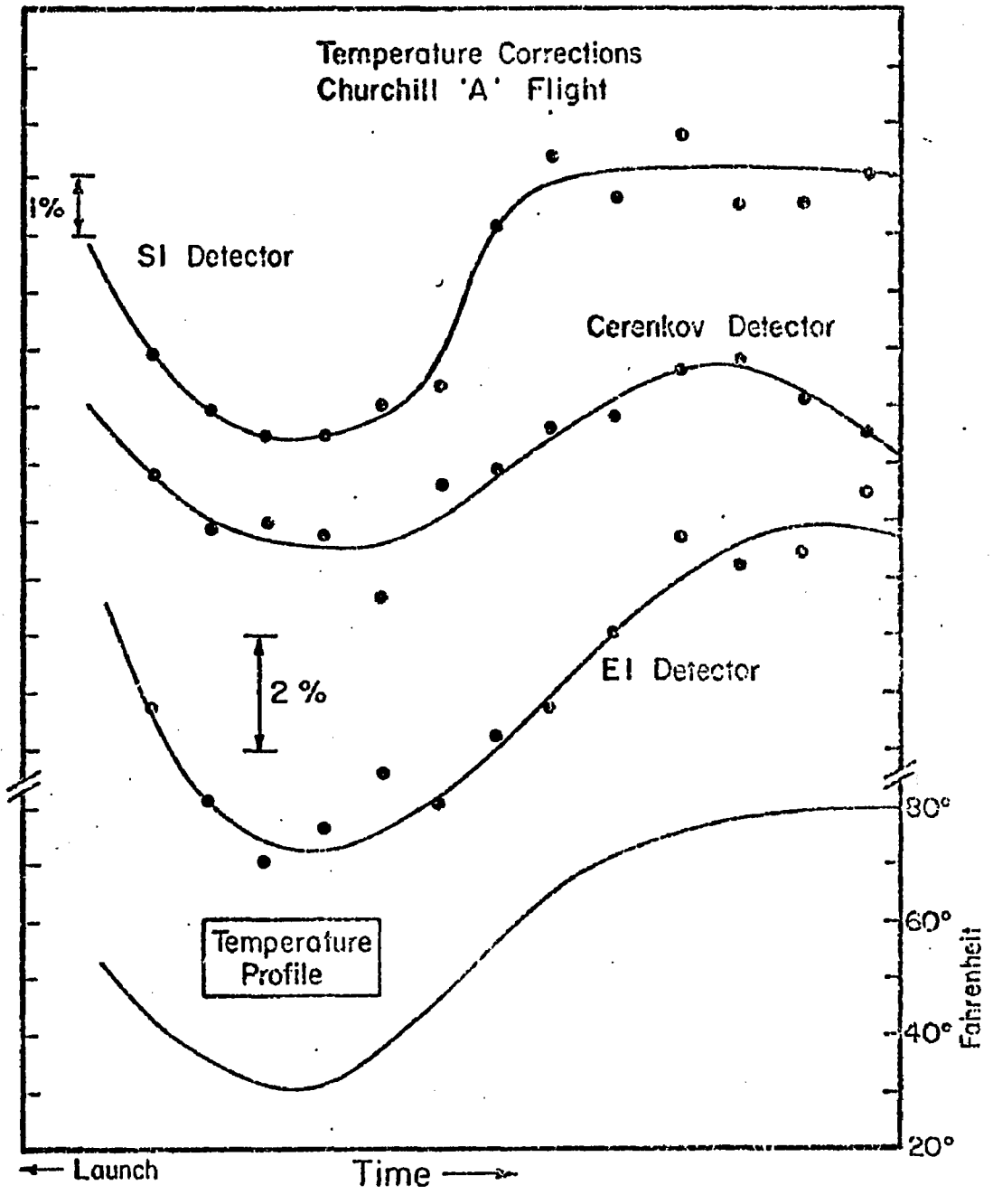

Figure A2.5 Temperature Corrections 'A' Flight

1974 INTERFLIGHT NORMALIZATIONS

	S1	C	S2	E1	E2
Churchill 'A'	1.0585	1.021	1.076	1.00	1.039
Churchill 'B'	1.00	1.00	1.00	1.00	0.993
Sioux Falls	0.9575	0.947	1.0162	1.020	1.015

Table A2.1 Inter-Flight Normalizations

criterion*, and pulse height histograms were obtained for each charge, detector, and time interval. The gain shift of each charge relative to the initial interval was determined. An average gain shift for each hour was then determined. Figure A2.5 shows the time-temperature profiles of the "A" flight and the variations of gain in three of the detectors.

The correction was performed on a record-by-record basis, with linear interpolation in time being used to determine the correction factor for each record of data. Events due to helium nuclei were removed from the data at this point, to reduce the computational load.

4.0 INTER-FLIGHT NORMALIZATION

To improve the statistical accuracy of information for the instrument calibration and to eliminate repetition of analysis, the data from all three flights were combined. To accomplish this, normalization coefficients were determined for each detector and flight in the same manner as the hourly temperature coefficients were found. The normalization coefficients for the three flights are shown in Table A2.1.

*The selection criterion imposed was: $[S1-S2]<.3S$, where $S=(S1+S2)/2$, and $[E1'-S]<.7S$, $[E2'-S]<.7s$, $E1'$ and $E2'$ being normalized to the gain of S. [..] denotes absolute value.

Convolution Results on Cerenkov Detector
(from Lezniak, 1975)

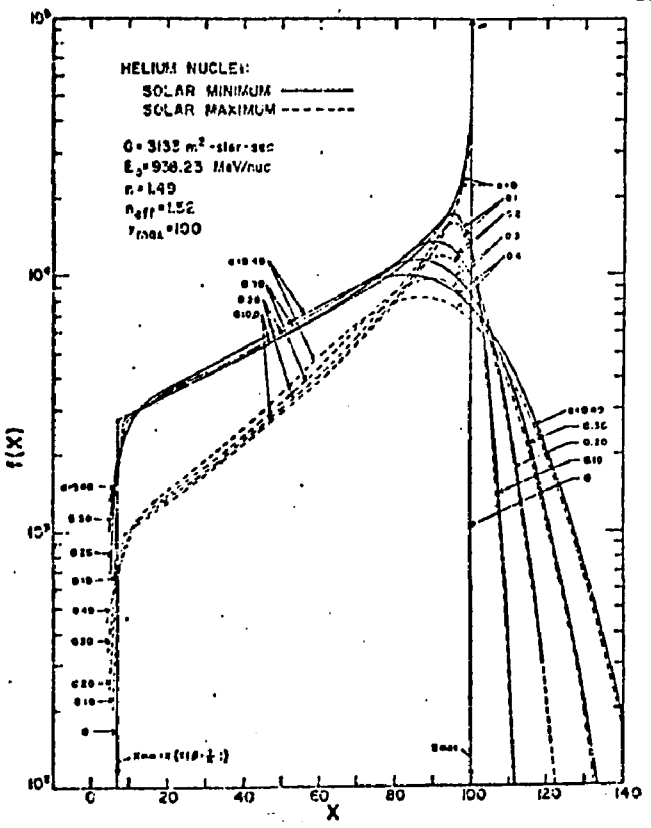

(a)

X_{max} = (v=1) response of detector with perfect resolution

α = inherent FWHM resolution at (v=1)

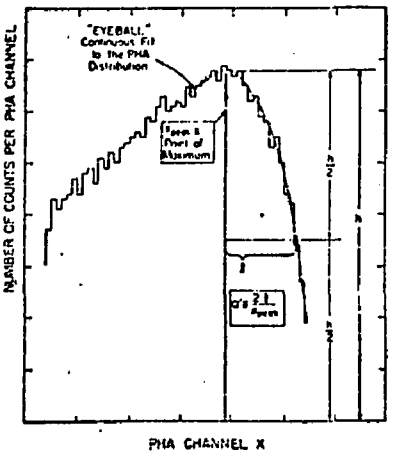

(b)

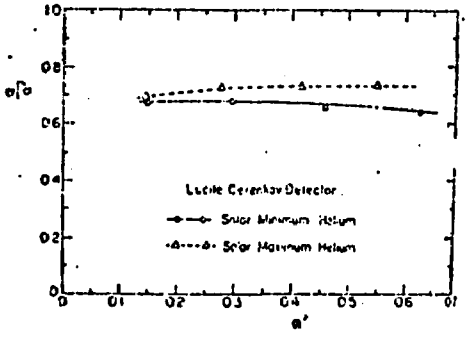

(c)

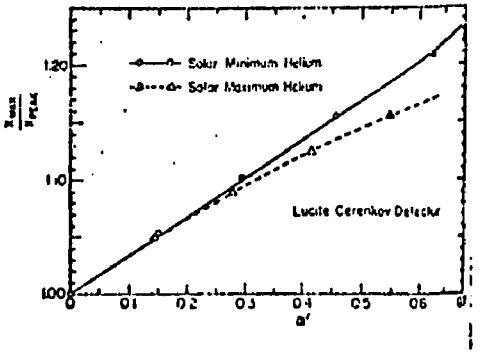

(d)

Figure A2.6 Convolution Results in the Cerenkov Detector

5.0 CERENKOV RESPONSE AT V=1

Lezniak (1975) has made a careful study of the effect of resolution broadening in Cerenkov detectors, with the purpose of extracting energy spectra from Cerenkov pulse height distributions. As a first step, he investigated the commonly used calibration point for Cerenkov detectors, the "v=1" peak. He determined the location of the v=1 point, given a typical Cerenkov pulse height distribution, by convolving the theoretical Cerenkov response as a function of v with Gaussian resolution functions, also a function of v, for typical energy spectra. The widths of the resolution functions were assumed to scale according to photoelectron statistics. The convolution results were used to define the relationship between the observed distribution peak location and the half-width of the distribution, and the inherent v=1 peak location and inherent detector resolution. Figure A2.6 shows the main features of the technique. Part a of this Figure shows the results of convolving the theoretical Cerenkov response with Gaussian resolution functions of various resolutions. Two examples of energy spectra are shown, one for solar minimum helium, and the other for solar maximum helium. Part b shows the definition of the parameters which are measured from an observed pulse height distribution, part c shows the relationship between the intrinsic detector resolution and the observed width shown on part b, and part d shows the effect of various detector resolutions on the position of the measured distribution

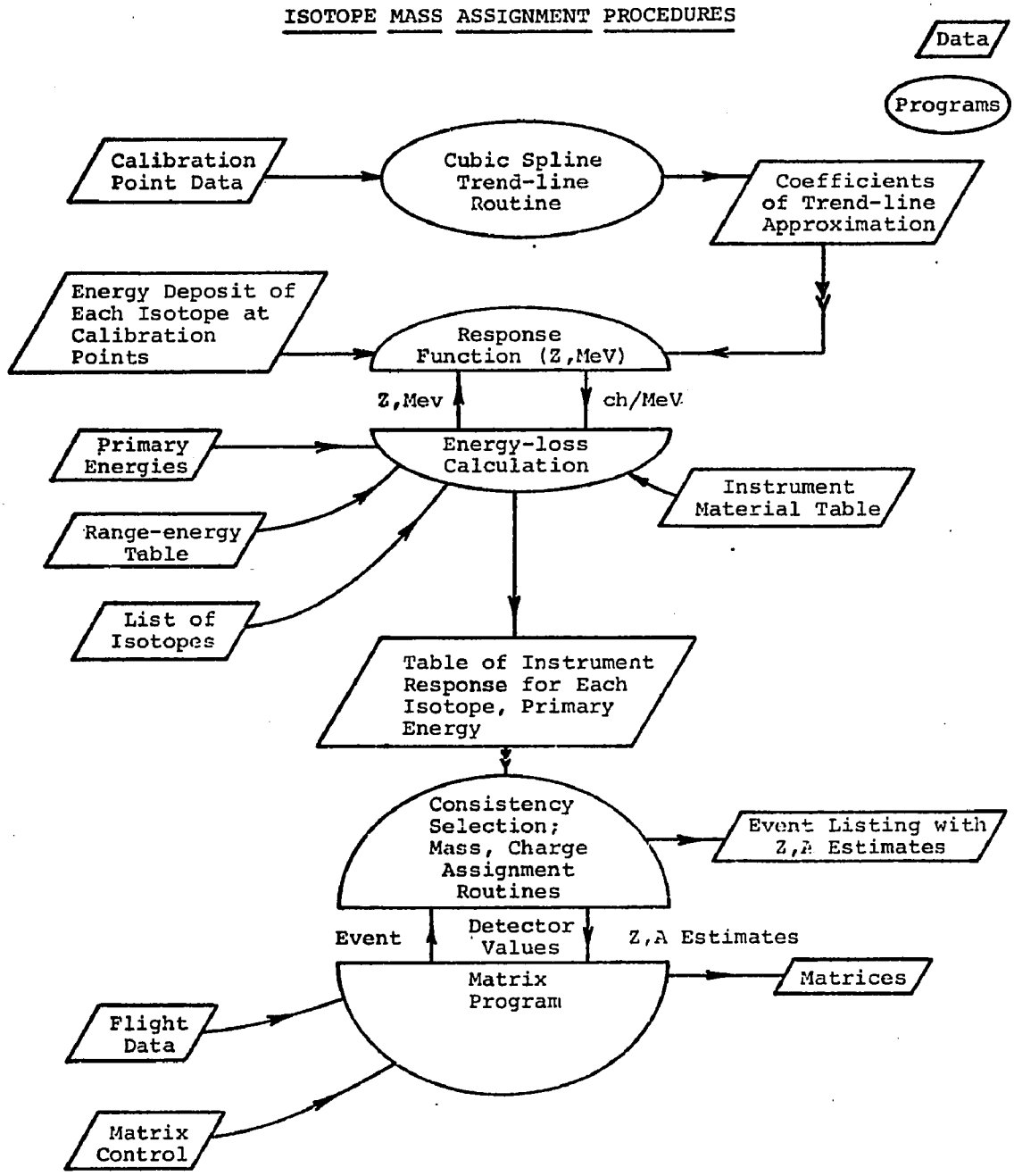

Figure A2.7 Isotope Mass Assignment Procedures

peak.

6.0 MAP OF THE CALIBRATION STEPS

This section presents a map of the procedures used in extracting the charge and mass information from the data with the help of the detector calibration points. Using the map, we will trace the steps taken in passing from estimates of calibration point data to charge and mass values for each event. There are three steps shown on the map, Figure A2.7:

1. The calibration data are fitted along trend-lines, as described in Chapter IV. To mathematically represent these trend lines, we have used a cubic spline fit of three breakpoints, which keeps the lines quite smooth. The set of spline coefficients for each trend line of each detector studied is the output of this step.

2. The next step gives predicted pulse heights in each detector for every desired isotope and energy. This program uses the spline coefficients and a look-up table of energy losses (Mev) at the calibration points for all isotopes of interest, to calculate the ch/Mev on the trend-lines at the calibration energies of each nuclide. Interpolation in log(Mev) by log(ch/Mev) between the points found on the trend-lines gives the response function for all energy deposits of the particular nuclide. An energy-loss routine gives the energy

deposit (Mev), which is multiplied by the response function ch/Mev(Z,A,Mev) to give the predicted detector response in channels. A table is generated listing the channel number of all the detectors studied for a suitable range of particle kinetic energies and nuclei.

3. The table produced in step 2 is used to interpolate charge and mass values for each event, which may then be plotted as desired.